POLITECNICO DI MILANO

School of Industrial and Information Engineering

Master of Science in Materials Engineering and Nanotechnology

Chemical Vapour Deposition of Zirconium Disulphide Thin Films

Supervisor: Prof. Carlo S. Casari
Politecnico di Milano

External Supervisor: Dr. Cecilia Mattevi
Imperial College London

Co-supervisor: Mauro Och
Imperial College London

Author:
Giulia Zoe Zemignani
876060

Academic Year 2018-2019

To those who have always

encouraged me to do my best.

Contents

List of figures ... viii

List of tables ... xiv

Acknowledgements ... xv

Abstract ... xvii

Estratto ... xix

Introduction ... 1

1 2D Materials based on TMDs ... 5

1.1 2D Materials ... 5

1.2 Transition metal dichalcogenides (TMDs): properties ... 6

1.2.1 Group VI TMDs ... 11

1.2.2 Group IV TMDs ... 13

1.3 Fabrication techniques for TMDs ... 15

1.4 Characterisation techniques for TMDs ... 18

1.5 Applications ... 25

1.6 Aims and objectives ... 27

2 Growth mechanisms in CVD technique ... 29

2.1 Principles of nucleation and growth for 2D materials ... 29

2.2 Physics of CVD ... 32

2.3 Mechanism of growth for TMDs ... 36

3 Experimental details ... 41
3.1 CVD experimental set-up and procedure ... 41
3.2 Raman spectroscopy and photoluminescence (PL) ... 44
3.3 X-ray photoelectron spectroscopy (XPS) ... 46
3.4 X-Ray diffraction (XRD) ... 48
3.5 Scanning electron microscopy (SEM) ... 49
3.6 Transition electron microscopy (TEM) ... 50
3.7 Energy dispersive x-ray spectroscopy (EDS) ... 51
3.8 Selected area electron diffraction (SAED) ... 51
3.9 Absorption spectroscopy ... 52
4 Synthesis and characterisation of TMDs ... 55
4.1 Introduction ... 55
4.2 Growth of 2D tungsten disulphide WS_2 ... 56
4.2.1 Characterisation of WS_2 ... 59
4.3 Growth of 2D tungsten diselenide WSe_2 ... 62
4.3.1 Characterisation of WSe_2 ... 63
4.4 Zirconium disulphide ... 67
4.4.1 Experimental trials for the sublimation of $ZrCl_4$ ... 67
4.4.2 Effects of specific parameters ... 72
4.4.3 Different substrate orientations ... 75
4.4.4 Deposition on Au foil ... 77
4.4.5 Deposition on sapphire ... 79
4.4.6 Choice of different precursors ... 80
4.4.7 Physical and morphological characterisation of ZrS_2 on SiO_2/Si... 81
4.5 ZrS_xSe_{1-x} alloys ... 100

4.5.1 Synthesis and characterisation 100
4.6 Final remarks 102
Conclusions and perspectives 103
Appendix 105
References 107

List of figures

Figure 1.1: Periodic table highlighting the three chalcogens and the transition metals of Group IV and VI (of our interest). Adapted from [2]. 6
Figure 1.2: Typical 2D crystal structure for TMDs. Left: 2H phase Group VIB TMDs. Right: 1T phase Group VIB TMDs [4]. 7
Figure 1.3: Left: Energy diagram of a typical semiconductor. Right: Brillouin zone of hexagonal lattice labelled according to the standard notation [2]. 8
Figure 1.4: DFT calculated band gap structures of 1L, 2L and 4L of WS_2 (top) and WSe_2 (bottom) [5]. 9
Figure 1.5: Band structure of monolayer ZrS_2 [6]. 10
Figure 1.6: Left: WS_2 on Au [17]. Right: WS_2 on SiO_2/Si [18]. Scale bars: 500 μm and 300 μm, respectively. 11
Figure 1.7: Left: False-colour DF-TEM image showing a continuous monolayer MoS_2 film [21]. Right: Optical images of the WSe_2 monolayers grown with KCl as growth promoter at 825 °C. Inset: high-magnification optical images of polygon-shaped crystals with hexagonal symmetry [15]. Scale bars: 1 μm and 200 μm, respectively. 13
Figure 1.8: AFM of monolayers and few-layers of ZrS_2 (top) [25] and HfS_2 (bottom) [27]. 14
Figure 1.9: Left: Optical reflection and transmission path of a TMD flake upon SiO_2/Si. Right: Contrast of MoS_2 vs. SiO_2/Si substrate [2]. 18
Figure 1.10: Optical band gap of many 2D monolayer materials [33]. 19
Figure 1.11: Schematics showing atomic displacement of four Raman active modes in WS_2 and WSe_2. The dotted lines are the van der Waals forces [35]. ... 21

Figure 1.12: Normal optical modes for ZrS_2; empty dots are S atoms, plain dots are Zr atoms [37]. 21
Figure 1.13: Representation of the crystal structure of ZrS_2. Chalcogen atoms are represented in yellow and zirconium atoms in green. Left: Lateral view of a unit cell. Middle: The c-axis view of four unit cells. Right: Extended view of the crystal structure where the layered structure can be appreciated. The out-of-plane Raman mode A_{1g} and the in-plane E_g one are sketched [36]. 22
Figure 1.14: Raman spectra of WS_2 from 1L to 6L [5]. 22
Figure 1.15: From the left: PL spectra of 1L–6L WSe_2 nanoflakes on 300 nm SiO_2/Si substrates; corresponding IT and DT emission peak positions; peak position differences between IT and DT emission of 2L–6L WSe_2 [5]. 23
Figure 1.16: Thickness dependence of the Raman spectra for ZrS_2 (λ=532 nm) on a silicon substrate with 285 nm of SiO_2. Inset: Zoom of Raman spectra in the characteristic peak for thin layers. The intensity has been normalized to the height of the silicon phonon peak [36]. 24
Figure 1.17: Some applications for semiconducting TMDs [33]. 25
Figure 2.1: Schematic of the processes determining the growth of a film on a solid substrate [33]. 30
Figure 2.2: Schematic of the three growth modes for thin films. Θ is the overlayer coverage in monolayers (ML) [47]. 32
Figure 2.3 Left: Schematic of a CVD process from a nano/micro-scale point of view (dashed oval) and macro-scale equipment required. Right: The three gas flow regimes as a function of the component pressure and dimensions [48]. 34
Figure 2.4: Basic flow model for a flat substrate in a horizontal tube reactor in the viscous regime [48]. 35
Figure 2.5: Hexagonal MoS_2 crystals alternating Mo-zz and S-zz faces [49]. 36
Figure 2.6: Wulff construction and the relationship between Mo:S atom ratio and domain shape [51]. 37
Figure 2.7: The two regimes and the polycrystalline growth analysed for graphene, h-BN and MoS_2, respectively [52]. 38

Figure 2.8: Left: Nucleation at different sites and times. Right: Nucleation at the same site and simultaneously [52]. 39
Figure 3.1: Real and schematic of the CVD set-up used. 41
Figure 3.2: Schematic of PL process [57]. 45
Figure 3.3: Schematic of core electron ejection by means of an x-ray radiation [Notes form a characterisation course]. 46
Figure 3.4: Basics of a typical XRD experiment [57]. 48
Figure 4.1: Optical micrographs of WS_2 nanocrystals grown at different temperatures and from different precursors [14]. 56
Figure 4.2: CVD set-up for the synthesis of WS_2. On the right the main furnace (F1), on the left the secondary furnace (F2) [14]. 58
Figure 4.3: Optical image of WS_2 mono- and few-layers. The monolayers are indicated with white arrows. Scale bar: 50 µm. 59
Figure 4.4: Raman spectrum of a WS_2 monolayer crystal labelled with characteristic vibrational modes. 60
Figure 4.5: Left: Comparison of Raman spectra of a monolayer and a few-layers crystal. Right: Raman spectra of WS_2 for 1L, 2L, 3L and bulk [62]. 61
Figure 4.6: Left: PL spectrum for 1L-WS_2, peak position at 1.99 eV. Right: PL spectra characteristics of WS_2 grown using: WO_3 at 950 °C, WO_3 + NaCl at 850 °C and H_2WO_4 + NaCl at 850 °C compared to the PL of a mechanically exfoliated sample. Individual spectra (dotted line) and deconvolution in exciton and trion components are shown [14]. 62
Figure 4.7: Micrographs of WSe_2 crystals and polycrystalline parts. a. Corner of an SiO_2/Si substrate where nucleation density is high; b. Substrate scratch acts as nucleation centre; c. Polycrystalline film with different nucleation density areas; d. Homogeneous polycrystalline film. Scale bars: a. 20 µm, b. 50 µm; c. 50 µm; d. 50 µm. 64
Figure 4.8: Optical microscopy of WSe_2 monolayers (left) and thicker layers (right). Scale bars: 50 µm. 64

Figure 4.9: Raman spectrum of WSe_2 monolayer (left) and few-layers (right), labelled with characteristic vibrational modes. The 520 cm^{-1} peak refers to the silicon substrate. 65
Figure 4.10: PL spectrum for 1L-WSe_2. The maximum of the peak is positioned at 1.65 eV. 66
Figure 4.11: Vapour pressure of $ZrCl_4$ empirically calculated (left) and from Clausius-Clapeyron equation (right). 68
Figure 4.12: 1st CVD configuration. 69
Figure 4.13: Comparison between the S and $ZrCl_4$ curves of vapour pressure vs. temperature. The interception is an indication of the best choice for deposition. 70
Figure 4.14: 2nd CVD configuration. 71
Figure 4.15: Optical micrographs showing the complete coverage by ZrS_2 both on the edges (left) and on the central part (right) of the silicon wafer. Inhomogeneities are visible. Scale bars: 50 µm. 72
Figure 4.16: Cluster of ZrS_2 73
Figure 4.17: Optical images of S at different scale bars and relative Raman spectrum (confirmed by RRUFF database). 74
Figure 4.18: Upside-down configuration. The silicon and sapphire wafers are placed face-down upon two $ZrCl_4$-containg crucibles. 76
Figure 4.19: Micrographs of SiO_2/Si (left) and Al_2O_3 (right) substrates in the upside-down configuration are shown. Scale bars: 20 µm. 77
Figure 4.20: Photograph showing the Au foil over the SiO_2/Si sample. A piece of gold has been cut to show the deposition of ZrS_2 also on the silicon substrate. 78
Figure 4.21: SEM images of ZrS_2 deposited on gold foils. Scale bars: 10 µm and 100 µm, respectively. 78
Figure 4.22: XPS spectra of ZrS_2 on gold. 79
Figure 4.23: Sulphur structures on sapphire. 80
Figure 4.24: Structures from the deposition of ZrO_2 + NaCl and S as precursors. Scale bars: 20 and 10 µm, respectively. 81

Figure 4.25: Left: Experimental spectrum of ZrS_2 thin film grown by CVD. Right: Raman spectra for different number of layers obtained by mechanical exfoliation [36]. 82
Figure 4.26: Deconvolution and fitting of the experimental main peak for ZrS_2 (blue dotted line). The yellow curve refers to the A_{1g} peak, the red curve to the "*" broadening of A_{1g}, while the violet curve resembles the total fitting. 83
Figure 4.27: Left: Optical micrograph of a ZrS_2 sample grown for 25 min. Scale bar: 100 µm. Right: Raman spectra of the three circled points in the left image. 83
Figure 4.28: Raman map of the intensity of the A_{1g} peak (on the right) referring to the blue squared area from the optical micrograph on the left. 85
Figure 4.29: Raman map and related histogram of the intensity of A_{1g} peak..... 85
Figure 4.30: Raman map and histogram referring to the FWHM of the A_{1g} peak of a sample grown for 15 minutes. The histogram has been normalized to 1. ... 86
Figure 4.31: XPS spectra of polycrystalline ZrS_2 sample grown for 12 minutes. 87
Figure 4.32: EDS spectrum of an exfoliated flake of ZrS_2. 88
Figure 4.33: XRD spectrum of a polycrystalline ZrS_2 thin film. 90
Figure 4.34: TEM images of different flakes taken at different magnitudes. Left: Perfect triangular flake; scale bar 0.2 µm. Middle: Few-layered flake; scale bar 0.5 µm. Right: Thick sample; scale bar 1 µm. 91
Figure 4.35: HR-TEM images of the flakes. Crystalline and amorphous domains are visible. Scale bar: 10 nm. 91
Figure 4.36: Left: Top and side views of monolayer ZrS_2 showing the hexagonal lattice; a, b and c axes are defined [70]. Right: SAED image of the triangular flake in the inset. A perfect hexagonal lattice is visible. 92
Figure 4.37: SEM samples-holder carrying ZrS_2 on both SiO_2/Si and gold substrates. 93
Figure 4.38: SEM images of ZrS_2 samples grown on SiO_2/Si at different times: 10, 15 and 25 minutes. Scale bars: 300 nm; magnitude 53.97 k. 94
Figure 4.39: SEM images of ZrS_2 samples grown for 12, 15 and 25 minutes. Scale bars: 1 µm; magnitude 12 k. 94

Figure 4.40: SEM image from a non-perpendicular direction. Scale bar: 300 nm; magnitude 53.97 k.......... 95
Figure 4.41: Cross-sectional SEM images portraying vertical flakes. Scale bars: 10 µm and 5 µm, respectively. 95
Figure 4.42: a. SEM image of a ZrS_2 cluster with terraced structure; b. ZrS_2 flakes ball with high contrast. Scale bars: 300 nm and 1 µm, respectively. 96
Figure 4.43: Top left: Area selected for the EDS map. Maps of oxygen, silicon, sulphur and zirconium are shown. 96
Figure 4.44: Photograph of ZrS_2 samples grown with increasing growth time as indicated in the picture (in minutes). Bare silicon substrate is reported at the extreme left. 97
Figure 4.45: PL emission spectrum of ZrS_2 thick layer. The experimental data (dotted line) have been fitted with a gaussian curve (line). 98
Figure 4.46: Absorption spectrum of ZrS_2 flakes in ethanol.......... 99
Figure 4.47: Comparison between Raman features of ZrS_2 (red) and ZrS_xSe_{2-x} (blue). 100
Figure 4.48: XPS spectra for ZrS_xSe_{2-x} alloy. 101
Figure A.1: Sulphur structures, crystallites and ribbons. 105
Figure A.2: Left: Exfoliated ZrS_2 flake on TEM grid. Right: Resultant SAED pattern. 106

List of tables

Table 1: Precursors and parameters chosen for the synthesis of WS_2 monolayer crystals. 57
Table 2: Precursors and parameters chosen for the synthesis of WSe_2 monolayer crystals. 63
Table 3: Precursors and parameters chosen to synthesise ZrS_2, as a first trial. .. 69
Table 4: Parameters chosen for the optimized synthesis of ZrS_2. 71

Acknowledgements

I'd like to acknowledge Dr. Mattevi for the opportunity to join her group at Imperial College of London to carry out my Master thesis. Furthermore, a special thanks goes to my supervisor, Prof. Casari, for his constant presence and availability during my research project.

This work would have not be possible without the support of the whole research group. Specifically, I'm extremely grateful to Mauro Och for the excellent tutorship and valuable advice during the whole research period, as well as SEM, XPS and XRD measurements. Also thanks to: Maria Sokolikova for her prompt recommendations and for the TEM, SAED and EDS measurements; Pawel Palczynski for the assistance and tips in Matlab; Apostolos Panagiotopoulos, Gang Cheng and Stefano Tagliaferri for their further results with SEM, EDS mapping, TEM and SAED. A particular mention to Dr. Regoutz and Mr. Sweeney for their precious teachings.

My thanks are extended to my fellows at Politecnico di Milano, particularly Teo, Chiara, Sofia, Mel and everyone who supported me during these years full of joy and cheerfulness. Thanks to my boyfriend, Alessandro, for making me face exams with the right amount of anxiety and for amuse me and amaze me at every possible time. The exceptional aid of you all made me achieve this goal.

Finally, I'd like to profoundly thank my parents, Valeria and Mauro, for all your help and support in making me get through though moments during my whole

academic career. Without you, nothing of this would have been possible and I will never repay you for what you have done. This thesis is dedicated to you both and to my grandparents and their belief in the improvement through personal efforts. A special thought to you, grandma Ninina, I wish you were here to see and celebrate with me.

Abstract

In this project, developed at Imperial College London, for my Master degree in Materials Engineering and Nanotechnology at Politecnico di Milano, I have been working with mono- and few-layered materials of the family of transition metal dichalcogenides (TMDs). The objective was the development of a reproducible synthesis procedure, by chemical vapour deposition (CVD), of an almost unexplored material, zirconium disulphide (ZrS_2). The initial syntheses were performed on tungsten disulphide (WS_2) and tungsten diselenide (WSe_2), two materials of Group VI TMDs, by routine CVD procedures developed by the research group. Their synthesis has been a useful tool to introduce the research on ZrS_2 and to understand the physical and chemical properties of TMDs in general. After an extensive experimental research, aimed to tune the parameters in order to achieve the highest ZrS_2 quality, it has been possible to synthesise films of ZrS_2 over cm^2 areas of silicon substrates. These films present vertically oriented flakes grown on a layer-by-layer structure of the same material, deposited on both silicon substrates and gold and unreported at the present time. Furthermore, the size of the vertical flakes can be tuned according to the growth time. The produced ZrS_2 films have been thoroughly characterized. Raman spectroscopy measurements match with the previous literature, as well as TEM and SAED confirming the layered and hexagonal crystal structure. We have also measured a photoluminescence (PL) signal at $\sim$ 1.4 eV, corresponding to a photon absorption in the NIR. Furthermore, the chemical characterisation by means of EDX highlighted slight vacancies of sulphur in the structure, whereas non obvious contaminations of chlorine and overall crystalline purity have been

revealed by XPS measurements. Finally, cross-sectional SEM has reported some few µm-high vertical flakes, revealing the roughness of the overall surface. The XRD has detected the oriented layered structure of our material, suggesting a layer-by-layer growth, while absorption spectroscopy proved their semiconducting character.

The reported CVD procedure represents an important initial step to the further control of the morphology and dimensions of ZrS_2 thin films.

Estratto

In questo progetto, sviluppato all'Imperial College di Londra, per l'ottenimento della Laurea Magistrale in Ingegneria dei Materiali e delle Nanotecnologie al Politecnico di Milano, ho lavorato con materiali costituiti da singoli o pochi strati appartenenti alla famiglia dei dicalcogenuri di metalli di transizione (TMDs).

Questi ultimi sono materiali a strati, ognuno composto da tre piani, tenuti insieme dalle forze di van der Waals. Un singolo strato è formato da due piani di calcogenuri (S, Se, Te) con al centro uno piano formato da atomi di un metallo di transizione. Tra gli oltre 40 composti con questa struttura appartenenti ai TMDs, si possono trovare differenti proprietà elettriche che vanno dagli isolanti, ai semiconduttori, ai metalli. L'interesse verso questi materiali, e in particolare verso molti di quelli appartenenti al Gruppo VI e IV, risiede nel loro carattere di semiconduttori con molte potenzialità nell'ambito dell'elettronica e della optoelettronica. Per poter beneficiare di questi vantaggi però, la produzione su larga scala di 2D TMDs risulta essere un passo fondamentale da compiere verso lo sviluppo tecnologico.

Per questo motivo, l'obbiettivo della mia tesi è stato lo sviluppo di una procedura di sintesi riproducibile, attraverso la chemical vapour deposition (CVD), di un materiale semiconduttore quasi inesplorato tra i TMDs, il disolfuro di zirconio (ZrS_2).

Le prove iniziali di sintesi sono state condotte su disolfuro di tungsteno (WS_2) e diseleniuro di tungsteno (WSe_2), due materiali del Gruppo VI dei TMDs, attraverso una consolidata procedura CVD sviluppata nel gruppo di ricerca stesso.

Basandosi su tali procedure, vari tentativi sono stati svolti su ZrS_2 variando alcuni parametri, tra cui temperatura di deposizione, flusso di gas inerte, quantità di precursori, tipo di precursori e tempo di crescita.

In seguito a questa estensive ricerca sperimentale, mirata alla ricerca della migliore procedura per la crescita di ZrS_2, è stato possibile sintetizzare film di ZrS_2 delle dimensioni di cm^2 su substrati di silicio. Questi film presentano flakes orientate verticalmente su una struttura strato-su-strato dello stesso materiale, cresciuto sia su silicio che su oro e mai riportata fino ad ora. Inoltre, la dimensione di queste flakes verticali è stata regolata secondo il tempo di crescita.

I film di ZrS_2 prodotti sono stati caratterizzati a fondo. Misure di spettroscopia Raman hanno confermato i risultati riportati in letteratura, così come la TEM e SAED hanno dimostrato la struttura cristallina a strati ed esagonale. Abbiamo anche registrato un segnale di fotoluminescenza (PL) a ~ 1.4 eV, corrispondente all'assorbimento di un fotone nel NIR. Inoltre, la caratterizzazione chimica grazie all'EDX ha sottolineato lievi vacanze di zolfo nella struttura, mentre l'XPS ha rivelato contaminazioni non ovvie di cloro e una complessiva purezza cristallina. In fine, la cross-sectional SEM ha riscontrato alcune flakes verticali alte pochi micron, rivelando una complessiva rugosità superficiale, mentre le dimensioni laterali di queste variano da poche centinaia di nanometri fino a poco più di un micron, in base a tempo di crescita. L'analisi XRD ha rivelato la struttura orientata a strati del nostro materiale, suggerendo una crescita strato-su-strato, mentre la spettroscopia di assorbimento ha dato prova delle proprietà di semiconduttore del materiale.

La procedura CVD riportata rappresenta un importante passo iniziale per il successivo controllo della morfologia e delle dimensioni di film di ZrS_2.

Introduction

In recent years, we have witnessed a renovated interest in the study of transition metal dichalcogenides (TMDs). This important class of materials, a family of over 40 layered compounds, has followed the discovery of graphene, as its inorganic counterpart. The first report regarding the electronic properties of MoS_2, dates back to 2010 [1]. The peculiar properties of this material paved the way for a new branch in nanoscience and nanotechnology. Furthermore, due to the semiconducting character of most Group IV and Group VI TMDs, the research on these materials was quickly set in motion because of their attracting potential in many fields, including electronics, optoelectronics, sensors, and energy storage. But these purposes require large-scale syntheses of semiconducting TMDs nanosheets and thin films, in order to propel the new technologies of the future.

In this context, Group VI TMDs but, in particular, Group IV TMDs, have recently drawn attention due to their extremely high theoretical charge carrier mobilities and band gap in the VIS-NIR region, making these materials promising for electronic and optoelectronic devices. Despite the wide research centred on Group VI TMDs, nevertheless, only few reports have demonstrated the synthesis of few-layered Group IV TMDs and large-scale fabrication has yet to be achieved. Therefore, the objective of my thesis work has been focused on the design of a reproducible, safe and cost effective synthesis procedure to achieve a controllable large-area growth of single-layer zirconium disulphide (ZrS_2). However, the initial synthesis trials were performed on tungsten disulphide (WS_2) and tungsten diselenide (WSe_2), two materials of Group VI TMDs, by an already

consolidated CVD procedure developed by the group itself. Their syntheses have been a useful tool to introduce the research on ZrS_2 and to understand the physical and chemical properties of TMDs in general.

As one of the most controllable and industrially scalable preparation methods, the chemical vapour deposition (CVD) has been chosen to achieve this goal. Our one-step CVD process consists in the co-evaporation of a Zr-precursor and S powders in a horizontal tubular furnace in the presence of an inert carrier gas. In particular, the process do not involve the use of H_2, H_2S and H_2Se because of safety reasons and it also avoids carbon-containing precursors. Much effort has been devoted to the optimization of the CVD parameters for the synthesis of ZrS_2.

The thesis will be divided in four chapters and an appendix:

- **Chapter 1: 2D materials based on TMDs**
  A review of the basic science concerning 2D materials and particularly TMDs will be provided, including structural, electronic and optical properties of these materials. Furthermore, a specific analysis of Group IV and VI TMDs state-of-the-art for the CVD fabrication is presented, as well as the most used production methods. The most suitable characterisation methods for the study of TMDs are highlighted and the most interesting applications presented.
- **Chapter 2: Growth mechanisms in CVD technique**
  We present the principal growth mechanisms for thin films as well as a focus into the main physical mechanisms in a CVD synthesis.
  Furthermore, we provide insights into the growth kinetics of 2D materials, with particular attention to TMDs.
- **Chapter 3: Experimental techniques**
  A number of different state-of-the-art characterisation techniques are required to obtain information on the chemistry, morphology, crystallinity, optical and electrical properties of TMDs atomic layers. In this chapter, we explain the basics of the experimental techniques which

have been used to characterize the CVD-grown ZrS_2 material, which include microscopies (SEM, TEM), spectroscopies (Raman, PL, XPS) and diffractometries (XRD, SAED).

- **Chapter 4: Synthesis and characterisation of TMDs**

  The first part of the chapter is focused on the study and methodology for the growth of WS_2 and WSe_2 as trial materials with an already-known synthesis procedure. Afterwards, the research on the CVD production of ZrS_2 is presented and discussed, highlighting the influence of different parameters. A large characterisation analysis of the properties of the obtained ZrS_2 is then provided. As a final step, the attempt of ZrS_xSe_{2-x} alloy synthesis is reported.

- **Appendix**

  Extra results regarding the syntheses and the characterisations are here reported.

During the experimental activity, many characterisation techniques have been carried out to analyse the physical, chemical and morphological properties of the as-synthesised ZrS_2 thin films. Among these techniques, in which I have participated at first hand with other trained group members, we can list TEM, SEM, absorption spectroscopy, XPS and XRD. Personally, I conducted the Raman spectroscopy and photoluminescence measurements.

Chapter 1

2D Materials based on TMDs

1.1 2D Materials

Research on 2D materials started after the ground-breaking experiments on graphene in 2004, by Geim and Novoselov, awarded with the Nobel Prize in Physics in 2010.

The peculiarity of 2D materials lies in the novel properties arising from the shrinking of their dimensions down to the single or few-layered structures. Many 2D materials such as germanene, silicene, black-phosphorous, h-BN and transition metal dichalcogenides (TMDs) have been studied in the last 15 years. Due to the availability of a broad number of combinations, their easy exfoliation capability and their tunable and promising optical and electrical properties, TMDs are among the most studied. This family of materials possesses a band structure variable with the number of layers they are composed of; decreasing the size from bulk to monolayers, the band gap can change form indirect to direct, as it happens in Group VI TMDs [2]. Furthermore, due to the semiconducting character of some of them, TMDs can overcome an intrinsic limitation of graphene, namely the lack of an electronic band gap [3].

In general, 2D materials are appealing for the next generation electronics and optical devices; this is the reason of the intense scientific research that could drive the next generation technology.

1.2 Transition metal dichalcogenides (TMDs): properties

The discovery of transition metal dichalcogenides dates back to 1923, when their structure was first determined by Linus Pauling while studying molybdenite, natural MoS_2. Subsequently, in the '60s there were known more than 60 TMDs, 40 of which had a layered structure.

The future development was due to the discovery of suitable techniques to synthesise them, evolved from the mechanical exfoliation by scotch tape to the more scalable chemical exfoliation, chemical vapour deposition and many others.

Crystal structure

The chemical formula referring to the lattice structure of a generic TMD is MX_2, where M stands for a transition metal belonging to group 4 to 10 of the periodic table, while X refers to a chalcogen, S, Se, or Te (Figure 1.1).

Figure 1.1: Periodic table highlighting the three chalcogens and the transition metals of Group IV and VI (of our interest). Adapted from [2].

Bulk transition metal dichalcogenides are formed by the parallel stacking of monolayers, which are made of three atomic sheets where a transition metal layer is sandwiched between two external layers composed by chalcogen atoms. The in-plane bonds between the transition metals and the chalcogens are strong covalent bonds, however the monolayers are held together by weak physical van der Waals interactions.

These monolayers are stable if isolated and can exist in various polymorphs, whose arrangement is determined by the disposition of the chalcogen layers with respect to the transition metal one. If the six coordinating chalcogen atoms are aligned in the same direction, the coordination of the transition metal will be trigonal prismatic, leading to the 2H phase. If instead, the chalcogen layers point towards opposite directions, the coordination of the transition metal will be octahedral and the phase will be 1T. A rhombohedral structure is also reported as 3R, mainly present in Group V TMDs (and VI), such as Ta and Nb sulphides and selenides. The name of the phases is formed by a number, indicating how many stacking layers build up the unit cell (or how many molecules per unit cell), and a letter, indicating the structure of the crystal lattice (T = trigonal; H = hexagonal; R = rhombohedral). The main crystal structure for Group IV TMDs is thermodynamically stable in the 1T phase, while Group V-VI TMDs are thermodynamically stable in the 2H phase, as reported in Figure 1.2.

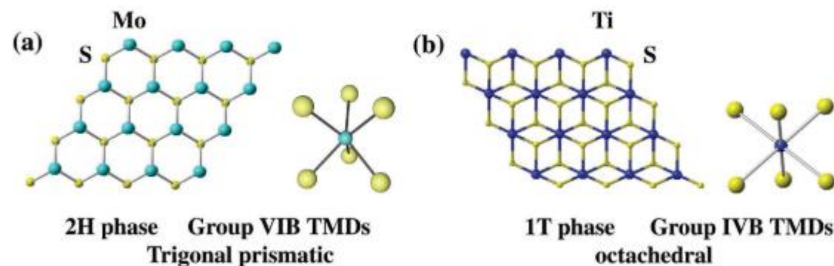

Figure 1.2: Typical 2D crystal structure for TMDs. Left: 2H phase Group VIB TMDs. Right: 1T phase Group VIB TMDs [4].

Electronic properties

Among the broad family of TMDs, the electronic properties span from insulators and semiconductors (MoS_2, WS_2, ReS_2), to semimetals (WTe_2, $NbTe_2$) and metals (NbS_2). We are interested in the study of semiconductors, thus we consider TMDs with a well-defined band gap in their electronic band structure. The electronic band gap is defined as the difference in energy between the conduction band minimum and the valence band maximum. The electronic band structure describes the range of energies an electron can possess and the range of energies which are forbidden to it (band gaps) within a solid. It is a direct consequence of the Bloch theorem and Bloch functions, which describe the eigenfunctions of an electron in a periodic potential, as a crystal lattice. The solutions of the Bloch waves can be characterized by their behaviour in the first Brillouin zone. The latter is a uniquely defined primitive cell representation in the reciprocal lattice, as shown in Figure 1.3 for a hexagonal lattice.

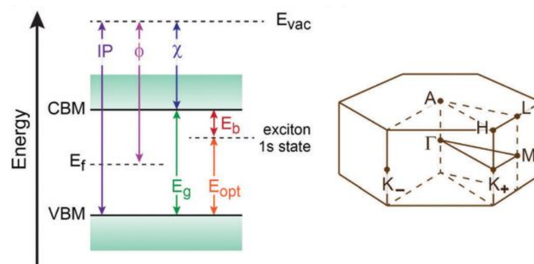

Figure 1.3: Left: Energy diagram of a typical semiconductor. Right: Brillouin zone of hexagonal lattice labelled according to the standard notation [2].

The band gap generally increases going form bulk to monolayers due to the lower number of atoms forming molecular orbitals and involved in the bindings. Furthermore, because of the different coordination of the metal atom in 1T and 2H phases, these two phases will have different electronic band structures due to the filling of the d orbitals of the transition metal [2]. In the case of semiconductors having a hexagonal crystal structure 2H phase (most of Group VI TMDs), they possess an indirect band gap in the bulk form. But for many of them, comprised MoS_2, WS_2 and WSe_2, when they come to the monolayer form

we assist to an abrupt change form an indirect to direct band gap, from bilayer to monolayer. Exemplification of this it is reported for WS_2 and WSe_2 in Figure 1.4.

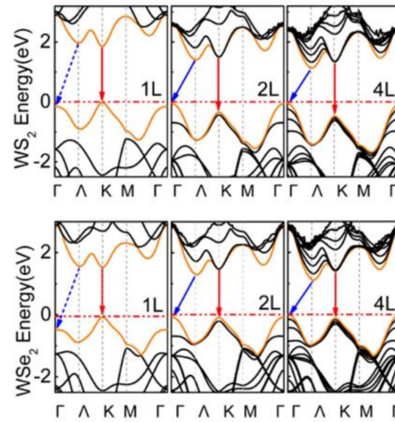

Figure 1.4: DFT calculated band gap structures of 1L, 2L and 4L of WS_2 (top) and WSe_2 (bottom) [5].

For WS_2 and WSe_2 monolayers, both valence-band maximum (VBM) and conduction-band minimum (CBM) are located at the K point in Brillouin zone.

Tungsten disulphide has an optical band gap in the monolayer form of ~ 2 eV, while tungsten diselenide have an optical band gap of ~ 1.65 eV, while for the bulk they are about ~ 0.9 and ~ 1.2 eV, respectively.

Group IV TMDs, differ from Group VI in terms of electronic properties and band structure. They are thermodynamically stable in the 1T phase, but sulphides and selenides are semiconductors, while tellurides and $TiSe_2$ are semimetals. In the case of Zr and Hf sulphides and selenides, they maintain an indirect band gap from the bulk to the monolayer form [4].

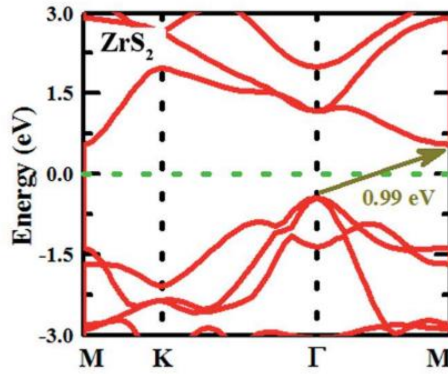

Figure 1.5: Band structure of monolayer ZrS_2 [6].

In literature there are different values associated to the indirect band gap of both ZrS_2 monolayer and bulk, depending on the different calculation methods used. The indirect band gap for the monolayer ranges from 1 eV to 2 eV, while for the bulk from it goes from 0.75 eV to 1.95 eV [4] [6] [7] [8] [9] [10]. A representative band structure for ZrS_2 monolayer is reported in Figure 1.5.

The charge carrier mobilities of semiconductors of Group IV are generally larger than the ones of Group VI, reaching theoretical electron mobilities above 2000 cm^2/Vs at room temperature [11]. In particular, for $HfSe_2$ has been calculated a ultra-high electron mobility of 3579 cm^2/Vs which is an order of magnitude larger than the one of MoS_2 (340 cm^2/Vs) [4].

Moreover, recent studies have proved that Group IV TMDs have promising thermoelectric properties for future device applications [12][13].

All these electronic properties, which can find application in many fields of electronics and optoelectronics (see Chapter 1.5), can be fully exploited only if we can achieve continuous mono- and few-layered TMDs over millimetre-scale, having large crystal sizes and high crystalline quality. As a matter of fact, defects and grain boundaries have a strong negative influence on these properties. Defects in the lattice introduce mid-gap states that acts as scattering or trap centres for non-radiative recombination, thus degrading both the electrical and optical properties.

In the following two chapters we will analyse the state-of-the-art of TMDs fabrication for Group VI and Group IV, focussing on the materials object of this thesis, thus WS_2, WSe_2 and ZrS_2.

1.2.1 Group VI TMDs

Nowadays, the applications in the field of electronics and optoelectronics require high quality crystal films on large-scale, but currently the scientific community is achieving only micron-sized crystals of high purity and the only large-scale films obtained possess low quality due to small crystal sizes [14] [15] [16]. We are referring to lateral sizes of triangular flakes of maximum values of 100-150 µm, which can be obtained in a reproducible manner. In the monolayer form the average step heights of WS_2 and WSe_2 are measured to be ~0.8 and ~0.9, respectively [5].

Tungsten disulphide has been successfully synthesised by many groups using the CVD technique. Tungsten disulphide deposited on gold, at ambient pressure, by *Ren et. al.*, seems to be the best result so far. The triangular monolayer single-crystal domains of WS_2 reach the millimetre-scale [17]. These are the largest domains obtained till now, since usual WS_2 crystal sizes are in the range of 100-150 µm [14] [18] [19]. As we can observe in Figure 1.6, the crystalline flakes deposed on gold are almost three times larger than the corresponding ones grown onto SiO_2/Si.

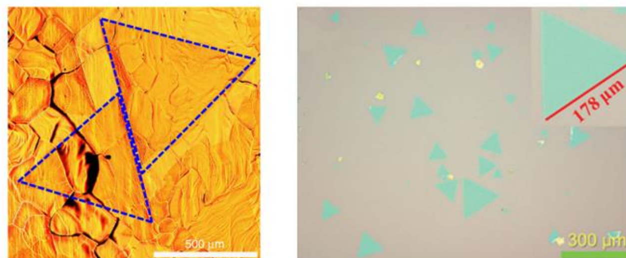

Figure 1.6: Left: WS_2 on Au [17]. *Right: WS_2 on SiO_2/Si* [18]. *Scale bars: 500 µm and 300 µm, respectively.*

Tungsten diselenide has been synthesised with the use of alkali metal halides as growth promoters via the CVD [15]; the hexagonal flakes on SiO_2/Si are visible in Figure 1.7 (right), having a lateral size of 50-100 μm. Field effect transistors constructed with that flakes have electron mobility up to 26 cm^2/Vs.

Ultrafast growth of WSe_2 have been reported by *Gao et. al.* [20] over polycrystalline Au substrates, claiming a growth rate of 26 μm s^{-1}, which is 2-3 orders of magnitude faster than traditional CVD processes on non-metal substrates and having mm-sized single crystals in just 30 seconds. Improving this procedure could lead to reduction of costs for the production and to a quicker industrial application of these materials.

Among the various fabrication techniques, the most promising results have been obtained by the use of MOCVD. Prof. Jiwoong Park and its group were able to synthesise uniform continuous monolayers of MoS_2 and WS_2 over 4-inch SiO_2/Si wafers via MOCVD. However, the grain size is in the range of 1 μm and so the electron mobility at room temperature dramatically decreases to 30 cm^2/Vs, but remaining similar to those of exfoliated samples [21]. These results are obtained after a synthesis of 26 hours due to a very low flow rate of precursors. A similar approach was used by *Robinson et. al.*, realizing thin films of WSe_2, this time on sapphire, by epitaxial growth, with domain sizes from 5 to 8 μm and similar carrier mobilities (29 cm^2/Vs) [16]. They also stressed the importance of a sufficient high temperature of growth to decrease the nucleation density and increase the adatoms mobility. This would favour the atomic diffusion along the domain edges, intuitively helping ripening processes of coalescence into large domains. They obtained a wafer-scale growth after one hour but using H_2 as carrier gas and at a pressure of 500 Torr.

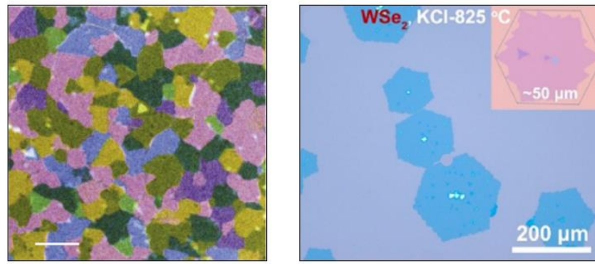

Figure 1.7: Left: False-colour DF-TEM image showing a continuous monolayer MoS_2 film [21]. *Right: Optical images of the WSe_2 monolayers grown with KCl as growth promoter at 825 °C. Inset: high-magnification optical images of polygon-shaped crystals with hexagonal symmetry* [15]. *Scale bars: 1 μm and 200 μm, respectively.*

Growth of WSe_2 monolayers on sapphire was possible also by the use of low-pressure CVD [22]. Physical vapour transport has been demonstrated to produce WSe_2 monolayers with optical quality comparable to the exfoliated samples [23].

1.2.2 Group IV TMDs

The fabrication techniques used for the syntheses of Group VI TMDs are currently widely investigated and many promising results have already been achieved. On the other hand, the investigation on growth techniques reserved to Group IV TMDs, such as ZrX_2 and HfX_2, has been reported only few times. To the best of our knowledge there is only one report on $ZrSe_2$ synthesis.

Regarding ZrS_2, only two communications reported the CVD growth of hexagonal crystals using $ZrCl_4$ as metal precursor and SiO_2/Si, h-BN or Al_2O_3 as substrates [24] [25]. In both cases the flakes do not grow over 10 μm of lateral size, even on an epitaxial substrate and the addition of H_2. Moreover, a spray deposition of ZrS_2 thin films by aqueous solutions containing zirconium-oxy-chloride and thiourea on glass substrate has been reported [26]. The result is a film with average grain size of 18 nm and covered with densely packed nanotubes of ZrS_2 achieved by an economical technique.

Zirconium diselenide synthesis has been reported in the supporting information of [25], where they substituted S powder with Se powder obtaining flakes of comparable size and shape.

Instead, HfS_2 and $HfSe_2$ have been reported a few more times, grown with CVD using chalcogen powders and $HfCl_4$, or exfoliated from CVT fabricated bulk crystals [27] [28] [29] [30] [31]. The resulting flakes possess comparable dimensions with ZrX_2 and hexagonal shape, as shown in Figure 1.8.

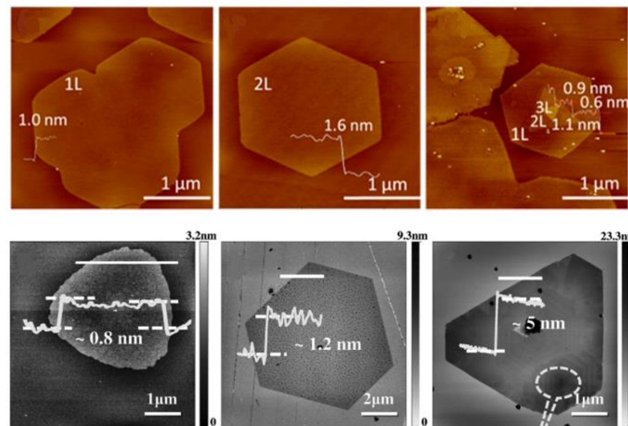

Figure 1.8: AFM of monolayers and few-layers of ZrS_2 (top) [25] *and HfS_2 (bottom)* [27].

Concluding, the fabrication of Group IV and VI TMDs presents gaps to fill and large room for improvement.

1.3 Fabrication techniques for TMDs

As stated above, the fabrication of 2D materials in mono- or few-layers form over large areas is currently a challenge in this field of research. Techniques that are available to synthesise TMDs usually show both advantages and disadvantages with respect to one another, meaning that further developments of the synthesis methods must be achieved in the future in order to promote a rapid development of the research and an effective acceleration from an industrial point of view.

In general, the fabrication of nanomaterials is divided in two different strategies, top-down and bottom-up.

The top-down methods refers to the erosion (reduction in size) of the bulk material until the achievement of the desired thickness and shape. The bottom-up methods instead, refers to all the growth methods which place atoms or molecules one at a time to build the desired nanostructure.

In the following, some examples of these methods are described highlighting the main advantages and drawbacks.

Micromechanical exfoliation using a scotch tape from a bulk source of TMDs is one of the simplest and cheapest methods. This procedure has widely spread the diffusion of these materials in their first period, since it doesn't require any sophisticated equipment. The successively peeling of layers form a bulk crystal, using ordinary adhesive tape, usually leads to about 1 µm layer in thickness or less. The major drawbacks are the non-scalability for large-scale production and the fact that the deposited flakes are usually non-homogeneous in thickness, size, orientation and phase.

Liquid-phase exfoliation is a scalable alternative based on organic solvents which allows to obtain flakes with controllable thicknesses. It consist of three main steps: 1) dispersion of the bulk MX_2 powder in an appropriate solvent; 2) exfoliation of the material into nanosheets with the development of shear stress

by a sonicator or shear mixer; 3) separation of the nanosheets (and size-selection) via centrifugation of the dispersion.

Another top-down fabrication method is the intercalation of guest species (including: simple atomic species, polymers, alkali metals and organometallic species) into the "van der Waals space" among different layers in TMDs. Lithium intercalation is one of the most diffused ones, typically using n-BuLi solution in hexane. After the intercalation of the species, exfoliation of MX_2 nanosheets is usually achieved by water addition. Drawbacks of the intercalation method are the phase transition from the semiconducting (2H) to the metallic (1T) phase that can occur and the limited size and quality of the obtained flakes.

For the direct growth of TMDs, molecular beam epitaxy (MBE) is another widespread technique, which have been used since the '90s. The process takes place in an ultrahigh vacuum chamber (typically 10^{-10} mbar) containing several sources, which form molecular beams of the material to be deposited. The substrate is preheated to favour atoms/molecules diffusion, while the thickness is monitored *in situ* thanks to the electron diffraction. The obtained materials can reach large dimensions but are characterized by many defects and large single crystals are usually not obtainable.

Also spray deposition form an aqueous solution has been used as a deposition technique to create thin films [26]. This technique results commercially scalable, low cost and applicable over large areas. The achievable thickness in this case is higher than the few-layers case and it usually reaches values over 1 μm.

Among all these techniques, chemical vapour deposition (CVD) arises as the best technique to overcome most of the problems above. As a matter of fact, it does not require ultrahigh vacuum to be effective and it is thus cheap and easy to be integrated in industrial processes. Moreover, CVD allows the user to control thickness, size and to grow large-area and high-quality TMD monolayers and few-layers, by controlling growth parameters such as temperature, pressure, precursors quantities, source-substrate distance and deposition time. Precursors

in the powder state and the substrate are inserted in a reaction tube, made of quartz, contained in a furnace which gradually increases in temperature, meanwhile an inert flux flows. When the precursors start to sublimate simultaneously, the reaction takes place in the vapour phase or on the substrate surface, leading to the growth of crystals. During the deposition process, millimetre-sized single-crystalline monolayers can be obtained, as well as uniform wafer-scale polycrystalline films. The misorientation among crystals is the main cause of grain boundaries and, generally, defects, leading to the degradation of the electrical and optical performances of these materials, compared to the theoretical ones. Furthermore, the growth continuity is limited due to the consumption of precursors and the consequent cessation of their supply after a certain time.

To remedy this and the difficulties in terms of thickness-control and uniformity, recently metal-organic chemical vapour deposition (MOCVD) has been used. A better control on the concentration of each reactant can be achieved by regulating their partial pressures, during the growth process. Precursors are supplied in the gas phase. Highly pure carbon-free chalcogen precursors (such as H_2S and H_2Se) are reported to achieve large crystalline domains containing less metal elements impurities coming from the heating of stainless-steel and quartz tubing during the growth process [16]. In this case, the use of H_2 gas is necessary to remove the carbonaceous species generated during the process and avoid their incorporation [21] [32]. Full coverage of the substrate by a polycrystalline layer has been reported with average grain size in the order of 1 to 10 μm.

Wet chemical synthesis is another bottom-up route which involves chemical reaction in the liquid phase at elevated temperatures, to increase the reaction rate. The nucleation and overall growth happens in a liquid medium and a variety of different morphologies can be achieved. Nowadays, the low controllability over the crystalline quality of the flakes makes these techniques disused for the synthesis of TMDs.

1.4 Characterisation techniques for TMDs

The characterisation survey has been addressed to the study of the morphological, compositional and optical properties of these materials.

A simple but fundamental tool as the optical microscope is the first method we use to identify if the material has grown and, if so, to have a first characterisation. With this tool, mono- and few-layers of TMDs can be easily detected if they are larger than 1-2 μm in lateral size and they are placed onto a refractive substrate, typically SiO_2/Si. Nanosheets of TMDs, both in monolayers and few-layers, possess a significant imaginary part of the refractive index along a large portion of the visible spectrum; this makes them attenuate the impinging light. Hence, because they are not reflecting a consistent fraction of visible light, if placed on a high contrast background, this enables their clear detection as darker areas.

In Figure 1.9 on the left we can see the path followed by the light during the measurement, instead, on the right, we see a plot of the optimal SiO_2 thicknesses (maxima at 78 nm and 272 nm) for the best contrast of MoS_2 flakes with the substrate. If a good contrast is achieved, the optical microscope can act as a screening process to identify mono- and few-layered structures. Indeed, the operator can be able to select nanosheets of TMDs which appear to have a lower contrast with respect to the substrate, thus that are thinner than the others. Further measurements using, for example, AFM can then give a precise value of the number of layers.

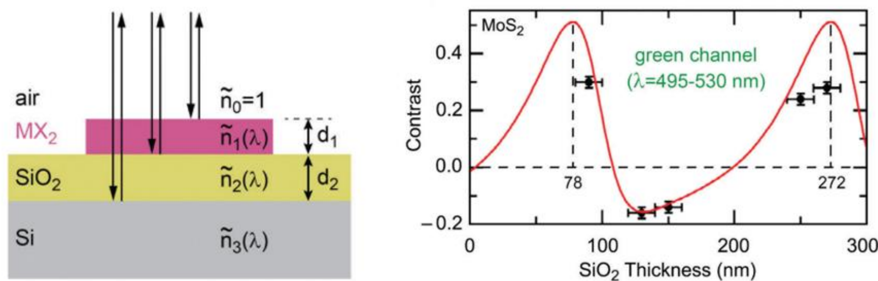

Figure 1.9: Left: Optical reflection and transmission path of a TMD flake upon SiO_2/Si. Right: Contrast of MoS_2 vs. SiO_2/Si substrate [2].

The photoluminescence (PL) analysis is another investigation that can be performed to know at which at which energy (and so wavelength) a particular material emits light. This is possible since Group VI-TMD monolayers are direct band gap semiconductors, therefore they show room temperature luminescence with a peak at their optical band gap, which is the electronic band gap minus the exciton binding energy: $E_{opt} = E_g - E_b$. Since the exciton binding energy is relevant even at room temperature (E_b = ~0.6 eV), a clear distinction between E_g and E_{opt} occurs. Also Group IV TMDs can have a PL, but, if so, it is associated to their indirect band gap. A schematic representation of many 2D monolayer materials, having direct or indirect band gaps, is shown in Figure 1.10.

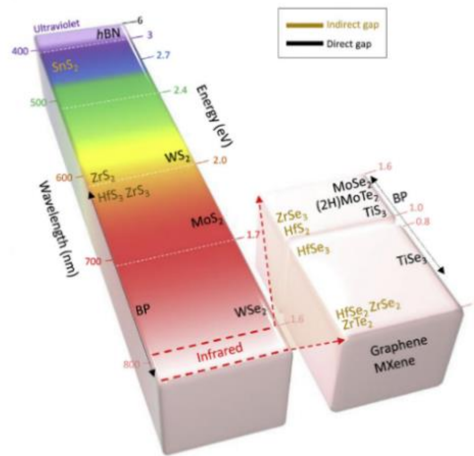

Figure 1.10: Optical band gap of many 2D monolayer materials [33].

Furthermore, the FWHM of the PL peak provides an indication of the purity and the crystal quality of the material. The direct/indirect band gap peak arises from the recombination of the exciton at the band gap edge. However, its position can result to be redshifted due to the contribution of negative trions (one hole bounded to two electrons) which are generated by the excess of electrons in some natively n-doped TMD sulphides and selenides, such as WS_2. Hence, a crystal that is rich in S or Se vacancies will have a larger contribution in the trionic transition, which occurs at lower energies with respect to the band gap and

results in an asymmetric PL peak. Any indirect transition occurs at lower energies and it is characterised by a very low intensity.

A fundamental analysis to assess the material we have grown on the substrate is Raman spectroscopy, which relies on the inelastic scattering of photons (see chapter 3.2 for the functioning). Due to the conservation of energy, the extra energy coming from the incident radiation can be used to trigger vibrations in the lattice. The emergence of specific vibrational modes, associated to each compound, can make us verify the presence of our materials and, as a first analysis, exclude the presence of others.

Depending on the symmetry of the primitive cell we are considering, we can have both IR active or Raman active modes:

- IR modes appear when we have a non-zero variation in the electric dipole moment μ, induced by an externa electric field, associated to the vibration:

  $$\left(\frac{\partial \mu}{\partial Q}\right) \neq 0$$

  Where Q are the internal coordinates of the vibrational problem.
- Raman modes are present only if a vibration alters the polarizability α of the material:

  $$\left(\frac{\partial \alpha}{\partial Q}\right) \neq 0.$$

We have to distinguish between Raman modes associated to the 2H phase and the ones associated to the 1T phase due to the fact that their crystallographic structure is different.

The irreducible representation of optical phonon modes at the zone centre Γ of the hexagonal Brillouin zone for a 2H phase TMD is:

$$\Gamma_{2H,optical} = A_{1g}(R) + A_{2u}(IR) + 2B_{2g}(S) + B_{1u}(S) + E_{1g}(R) + E_{1u}(IR) + 2E_{2g}(R) + E_{2u}(S)$$

where the Raman (R), infrared (IR) and silent (S) optical modes are shown [2].

The Raman active modes for TMDs in the 2H phase (WS_2, WSe_2) are thus [34]:

- The E^2_{2g} mode that is a shear mode corresponding to the vibration of different layers against each other appearing at very low frequencies and visible only in multilayers.
- The E_{1g} instead is an in-plane mode involving only chalcogens.
- E^1_{2g} is an in-plane displacement of all atoms.
- A_{1g} mode is an out-of-plane vibration which concerns only chalcogen atoms.

A schematics of these modes is give in Figure 1.11.

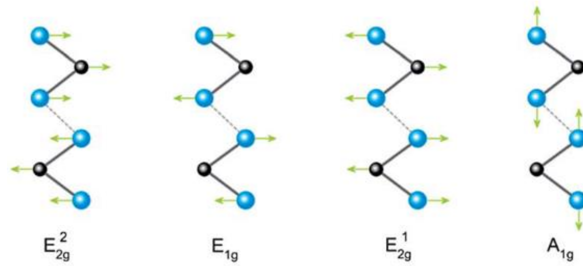

Figure 1.11: Schematics showing atomic displacement of four Raman active modes in WS_2 and WSe_2. The dotted lines are the van der Waals forces [35].

Instead, for a 1T phase TMD, the optical modes predicted at the Γ point, are [36][37]:

$$\Gamma_{1T,optical} = A_{1g}(R) + E_g(R) + 2A_{2u}(IR) + 2E_u(IR)$$

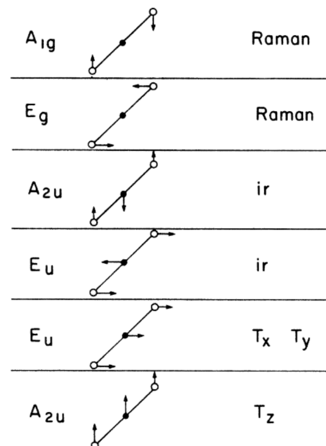

Figure 1.12: Normal optical modes for ZrS_2; empty dots are S atoms, plain dots are Zr atoms [37].

Raman active modes implicate that there is no dipole moment but just a change in the polarizability; this means that in both E_g and A_{1g} modes, the Zr atoms are at rest while the S atoms move in opposite directions. In the case of E_g mode, the S planes slide against each other, while in the A_{1g} mode, the S atoms are stretched in the out-of-plane direction (Figure 1.12). So, we would expect these two main peaks to appear in the Raman spectrum of ZrS_2 (Figure 1.13).

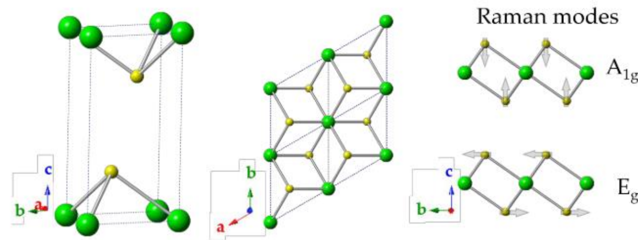

Figure 1.13: Representation of the crystal structure of ZrS_2. Chalcogen atoms are represented in yellow and zirconium atoms in green. Left: Lateral view of a unit cell. Middle: The c-axis view of four unit cells. Right: Extended view of the crystal structure where the layered structure can be appreciated. The out-of-plane Raman mode A_{1g} and the in-plane E_g one are sketched [36].

Furthermore, some TMDs exhibit a shift in the peak positions of the main Raman modes when we increase the number of layers from monolayer (1L) on; this is the case of MoS_2 and WS_2. As reported in the research of *Li et. al.* [5], the red-shifting of the E^1_{2g} mode and the blue shifting of the A_{1g} mode for WS_2, could be observed with increasing layer number from 1L to 5L. Beyond five layers, the peak position doesn't shift any more (Figure 1.14). As a matter of fact, the increment between a 1L and a bulk phase corresponds to just 4 cm^{-1} Raman shift, unfortunately.

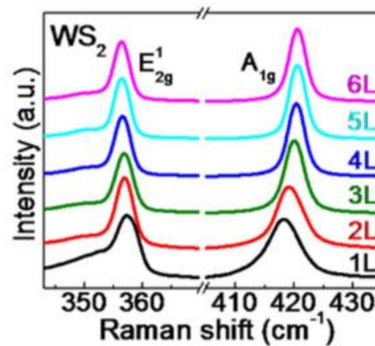

Figure 1.14: Raman spectra of WS_2 from 1L to 6L [5].

On the contrary, for WSe_2 it's very difficult to clearly distinguish the two modes E^1_{2g} and A_{1g}, because they are convoluted together in a single peak at 250 cm^{-1}. Moreover, due to the fact that heavier atoms tend to have weaker thickness-dependence of E and A modes shifting [35], the maximum shift from 1L to 6L is of just 1.3 cm^{-1}. For this case (but also for the previous one) it is possible to use another method to verify the number of layers. Since the band gap structure is very dependent on the number of layers, hence we can use the photoluminescence (PL) to study it. As a matter of fact, since WS_2 and WSe_2, in the monolayer form, are direct band gap semiconductors, only the direct transition (DT) emission can be seen in the PL spectrum. Increasing the number of layers however, indirect transition (IT) emissions show up at higher wavelengths than the direct one (Figure 1.15). The IT emission peak position presents significant layer shift with increasing number of layers, while for the DT peak, positions shifts are much smaller.

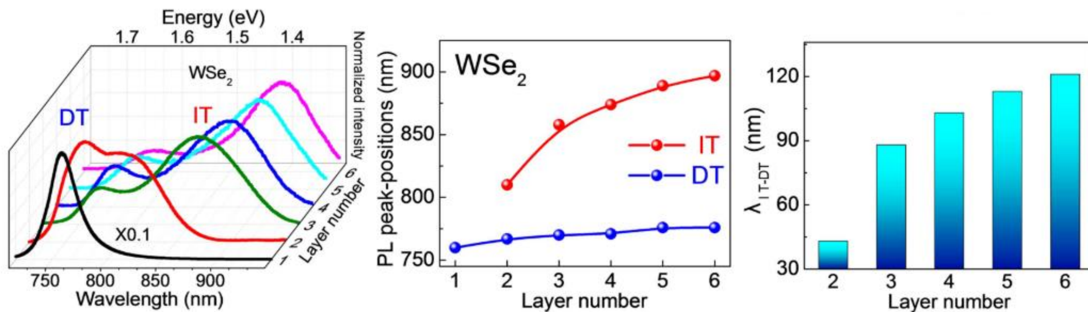

Figure 1.15: From the left: PL spectra of 1L–6L WSe_2 nanoflakes on 300 nm SiO_2/Si substrates; corresponding IT and DT emission peak positions; peak position differences between IT and DT emission of 2L–6L WSe_2 [5].

To obtain a reliable identification thus, it is preferable to calculate the difference in wavelengths between the direct transition and the indirect one (λ_{IT-DT}). This value can be taken as an indicator of the number of layers in our sample because minimizes the external influences, such as the substrate we used.

In the case of ZrS_2, it has been reported that the peak positions form bulk to monolayers don't undergo any shift, instead the peaks strongly decrease in intensity [36].

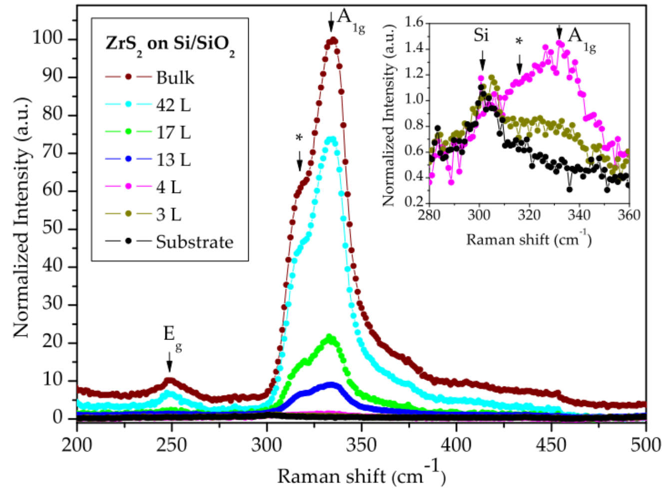

Figure 1.16: Thickness dependence of the Raman spectra for ZrS_2 (λ=532 nm) on a silicon substrate with 285 nm of SiO_2. Inset: Zoom of Raman spectra in the characteristic peak for thin layers. The intensity has been normalized to the height of the silicon phonon peak [36].

Specifically, the Raman spectrum of ZrS_2 bulk consists of an in-plane E_g mode at ~ 250.0 cm^{-1} and an out-of-plane A_{1g} mode at ~ 334.1 cm^{-1} [38], recognized as characteristic peaks. Moreover, the shoulder gathered to the A_{1g} mode appearing at ~ 320 cm^{-1} (labelled with "*" in Figure 1.16) is attributed to non-harmonic effects. In Figure 1.16 we can see how the intensity of the modes decreases with decreasing number of layers; once below 15 L the E_g mode is no longer visible and the same happens to the A_{1g} mode below 3 L. The silicon phonon peak is located at ~ 520 cm^{-1}.

1.5 Applications

Due to their tunable band gap in the VIS-NIR range, high charge carrier mobilities and on/off ratios, as well as their intrinsic layered structures, 2D semiconducting TMDs have been proposed in the last few years as an alternative to the conventional silicon-based technology [39]. Their main attractive applications are shown in Figure 1.17.

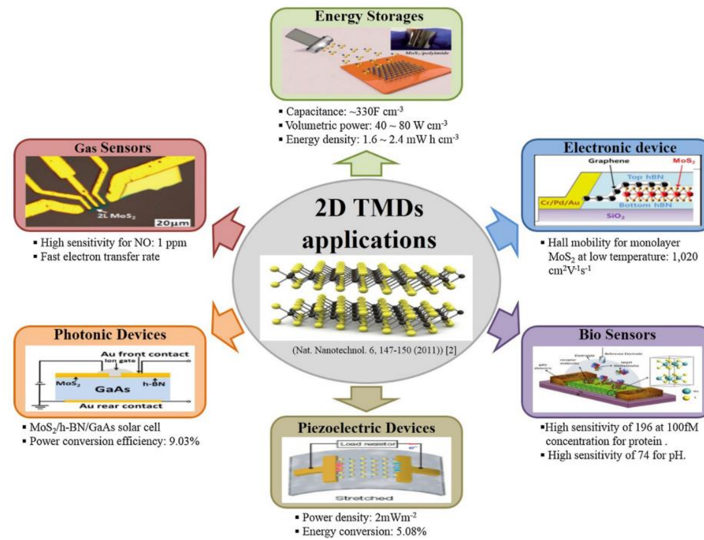

Figure 1.17: Some applications for semiconducting TMDs [33].

Innumerable FETs have been fabricated mainly with MoX_2 and WX_2, demonstrating good performances [2] [40], but also ZrX_2, HfX_2 and alloy-based FETs are being studied [41]. In particular, the ultra-high theoretical mobility values predicted for Zr and Hf selenides (2500 cm^2/Vs and 3500 cm^2/Vs, respectively [4] [11]) appear to be very promising. However, so far, the reported results were disappointing, showing carrier mobilities within 10 cm^2/Vs from exfoliated crystals [28] [42] [43] [44]; these results may be owing to the quality of nanosheets, oxidation, contact resistance and charge trapping.

Furthermore, the large-scale growth on insulating substrates, such as SiO_2, enables the fabrication of high-performance transistors and photodetectors without the need of film transfer [21].

The optoelectronic applications rely on the strong light-matter interactions in these materials. They include light-emitting diodes (LEDs), photovoltaic cells, photodetectors, light emitters/absorbers and photocatalysts, just to name a few. The greatest potential of Group IV TMDs relies in the field of photodetection; devices built with these crystals showed fast phot-response and exceptionally high responsivity [4]. HfS_2-based devices gave photoresponsivity values of 45 mA/W along with a response in the order of tens of miliseconds under 420 laser excitation [28]. A massive response of 3961 A/W with a 800 nm laser and 252 A/W with a 473 nm laser in about 7.3 ms has been reported for a photodetector fabricated using $HfSe_2$ [45].

Another emerging application is in the field of energy storage (e.g. supercapacitors and Li-ion batteries), since 2D TMDs can be used as electrode materials due to their atomically layered structure, high surface area, optimal electrochemical properties and low intercalation barrier for various cations.

Moreover, because of high surface to volume ratio that these 2D TMDs offer, various applications in the field of sensors have already been tested, including gas, chemical and biological sensors. Large amounts of target analysts per unit area can be detected with a rapid response and recovery [33].

Other recently investigated applications include photocatalysis and thermoelectric devices. The latter exploits materials such as WSe_2, which possess the lowest thermal conductivity among dense solids made of layered crystals and for this reason could be used in a thermoelectric device [46].

Furthermore, due to their weakly bonded 2D atomic layers, TMDs can be easily isolated and stacked upon other TMDs to create a wide range of heterostructures [33] with no limitations of lattice matching. Also heterostructures using both TMDs and graphene are reported [17] [40]. In this way, new unique functions and properties can be achieved.

1.6 Aims and objectives

The objective of my thesis was focused on the CVD synthesis of ZrS_2 crystals on large-scale areas, involving carbon-free precursors and excluding the use of H_2, H_2S and H_2Se. To the best of our knowledge, this material has been synthesised only few times by CVD technique on silicon, sapphire and h-BN. The main challenge has been the capability to control different parameters of the CVD process, in order to achieve the best results. By the study of different growth parameters during the whole research period, I addressed to a reproducible synthesis procedure on both SiO_2/Si and gold.

Another aim of the project was to provide an extensive characterisation of this material in order to set a starting point for future developments. In this context, many characterisation techniques have been used, among which some spectroscopies (Raman, photoluminescence and absorption spectroscopies), XPS to show the presence of contaminants or the oxidation of the material, SEM to visualise the morphology of the material, as well as TEM, SAED and EDS for crystallographic and compositional studies.

Finally, I investigated the fabrication of alloys of zirconium, containing both sulphur and selenium, in the form of ZrS_xSe_{2-x}.

Chapter 2

Growth mechanisms in CVD technique

2.1 Principles of nucleation and growth for 2D materials

A deep understanding of material growth mechanism for the preparation of TMDs is fundamental in order to grow 2D materials with controlled quality, structure and properties.

The molecular processes that determine the growth of thin films in its first stages is showed in Figure 2.1. The molecules in the gas phase are transported onto the substrate, where they are absorbed on the surface. At this point they can either be immediately desorbed or diffuse along the surface. During the diffusion of an atom onto the surface, it can happen the nucleation of two or more atoms or there can be the addition of an atom to an already existing island. The nucleation of a crystal happens by a self-assembly organization process. When two or more atoms/molecules aggregate together on the surface of a substrate, they can from a nucleus that will be the starting point for the crystal growth. Once a nucleus is formed and it has overcome a critical size, a drop in free energy associated to the formation of the crystal phase happens and the nucleus can grow to form a crystal. Another phenomenon that can happen during deposition, and that we just mention for completeness, is the intermixing or interdiffusion between substrate and depositing material. The fact that we use SiO_2/Si as a substrate

prevents the interdiffusion mechanism since it is chemically inert. Instead, metal substrates like Cu or Ni can react with the chalcogen precursors of TMDs, forming metallic sulphides and selenides.

The actual happening of these mechanisms depends on many factors, such as the substrate characteristics, its temperature and on the energies of the particles required to activate each process.

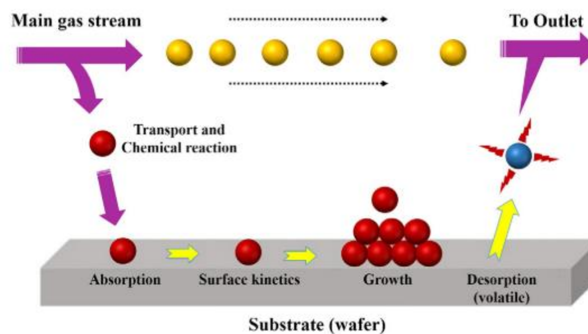

Figure 2.1: Schematic of the processes determining the growth of a film on a solid substrate [33].

Furthermore, the thin film growth is a non-equilibrium kinetic process that can be described by three growth models (Figure 2.2):

1. Layer-by-layer (or Frank-van der Merwe)

   It is the preferred growth mode because of homogeneity and uniformity (theoretically every atom occupies its proper lattice position) but it is not easy to achieve.

   It happens if the interaction between the substrate and the atoms of the film is higher than the interaction among the adatoms in the film. New layers start to grow only when the layer underneath is completed. As a matter of fact, the surface tension of the substrate forces the film to adapt to its surface (higher energy of the substrate).

   A part from the intuitive homoepitaxy growth, examples of 2D heteroepitaxy are reported for metal/metal, metal/semiconductor and semiconductor/semiconductor.

2. 3D islanding (or Volmer-Weber)

   Due to the fact that the interaction between adatoms of the film is higher that the interaction film-substrate, the film grows forming islands (clusters). This is the typical case that occurs for metal films on insulating or contaminated substrates. The layers grow faster in the perpendicular direction than in the parallel plane to the substrate, creating 3D structures. When two islands come in contact there is the formation of grain boundaries and, in turn, they can coalesce to form a continuous film. Higher energy of the film with respect to the substrate favours the formation of small structures with less surface areas rather than combining with the substrate.

3. Layer-by-layer followed by 3D islanding (or Stranski-Krastanov)

   A layer-by-layer film is deposited only till a certain thickness, after which there is a changing in the growth mode becoming 3D islanding. The distortion of the deposited-material lattice to match the mismatch from the substrate lattice generates high internal stresses.

   The transition from 2D to 3D islanding is driven by the elastic strain $E_{elast} \propto \epsilon^2 h$, in the lattice. The $\epsilon = \frac{a_f - a_s}{a_s}$ is the lattice parameter mismatch between the film (a_f) and the substrate (a_s) while the h is the film thickness. Above a certain thickness the internal stresses are so high that there is the switch in the 3D islanding growth mode and the growth is driven by a decrease in the total system energy. If this growth mode happens and we are able to control the thickness of the first layer-by-layer part of the film, we would be able to have just that growth mode in that thickness. In this case we need the surface tension of the substrate to be the highest but with misfit, a difference in the lattice parameter between lattice and film.

Coverage / Mechanism	θ < 1 ML	1 < θ < 2 ML	θ > 2 ML	Examples
3D island growth				Metals on SiO_2
2D layer growth				Cu/Cu, Si/Si, GaAs/GaAs
S-K growth				In/Si, Ge/Si InGaAs/GaAs

Figure 2.2: Schematic of the three growth modes for thin films. Θ is the overlayer coverage in monolayers (ML) [47].

2.2 Physics of CVD

As stated in Chapter 1.3, the vapour deposition methods are the most suitable to obtain wafer-size deposition of high-quality monolayers.

A typical setup consists of a tubular furnace linked to an Ar or N_2 cylinder to one end, while on the other to a vacuum pump that collects the fumes and controls the pressure in the chamber. The substrate and the precursors are loaded in the quartz tube, then the powders are sublimated at high temperature and transported on the substrate by the inert carrier gas. For further details regarding the CVD synthesis, see Chapter 3.1.

The CVD growth process takes place at the substrate surface, at the molecular level. There, the thermodynamics and kinetics of precursors chemistry, as well as the dynamics of mass and heat transport and the physics of crystal growth, play a fundamental role. In Figure 2.3 we can see the representation of the representative system components that control the CVD process [48]. These components influence the quality, crystal size and repeatability of a particular CVD process. Thus, their choice is related to the previous acquired knowledge on that specific system. We can observe that, after the mass flux reaches the substrate, the precursors react in the gas phase or on the substrate. Then, after the

adsorption, the atoms can diffuse on the substrate or they can desorb and be carried away by the gas flow.

The dynamics of this process is governed by the Knudsen number, Kn, which is the ratio between the mean free path in the reactor, λ, and the diameter of the reaction tube, D:

$$Kn = \frac{\lambda}{D}.$$

For instance, the mean free path for air at room temperature and pressure P (Pa) is:

$$\lambda = \frac{6.6 \cdot 10^{-3}}{P}$$

At pressure below 10^{-3} mbar, λ is so large that molecules typically collide only with the walls of the vacuum chamber [48].

There are two different regimes of flow which can be distinguished according to the value of the Knudsen number, Kn:

- Molecular flow, where the mean distance between molecular collisions is large compared to the dimensions of the system (we must have low pressure, low gas density). The gas molecules move randomly and collisions between molecules are rare compared to collisions with the walls.
- Viscous flow, where the mean free path is much smaller than the chamber dimensions (high pressure). This flow can be either laminar or turbulent, depending on the gas velocity.

The flow regimes in different ranges of the Knudsen number are:

- Molecular flow: Kn > 1 – there are no collision from one side to the other of the chamber
- Transition flow: 0.01 < Kn < 1
- Viscous flow: Kn < 0.01 – many collisions

Kn is strictly related to pressures (inversely proportional); high pressures result in viscous flow, while low pressures result in molecular flow. These flow regimes are governed by different laws; the right image of Figure 2.3 is useful to locate the right regime without calculating the Knudsen number. In our case, we used a pressure in the chamber during deposition of ZrS_2 of ~ 1.50 mbar = 150 Pa, while the diameter of the system is 2.8 cm. Thus, our flow regime is identified as viscous regime.

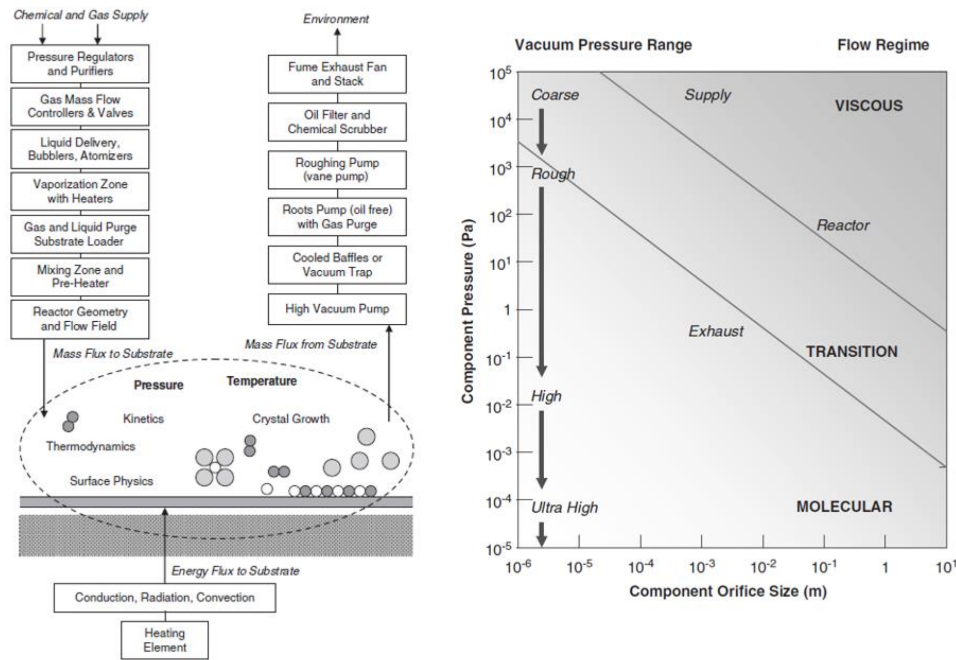

Figure 2.3 Left: Schematic of a CVD process from a nano/micro-scale point of view (dashed oval) and macro-scale equipment required. Right: The three gas flow regimes as a function of the component pressure and dimensions [48].

In the viscous flow regime, the vapours of the precursors are convected through the reactor by other molecules in the carrier gas flow. Then, they diffuse from the bulk gas flow to the substrate surface due to a concentration gradient. This regime is characterized by the presence of a mass transfer boundary layer on the substrate, which is the solid-fluid interaction zone (Figure 2.4). A boundary layer is a thin layer of viscous fluid close to the solid surface of a substrate in contact with a moving vapour flux. Within its thickness δ(x), the flow velocity varies from zero at the substrate (where the flow "sticks" to it because of its viscosity)

up to U_∞ at the boundary, which approximately corresponds to the vapour flux velocity. It is the main cause of non-homogeneous growth across the surface; we observed this phenomenon in almost all our samples, thus it is another proof that our syntheses lay in the viscous regime. In Figure 2.4 are reported all the equations that are valid in this regime and that can be used to identify the best growth parameters. Among them, the Reynolds number (Re) is a dimensionless parameter used to describe the flow characteristics; it is dependent on the bulk velocity of the gas flow, the characteristic length of the reactor (the diameter of the tube) and the kinematic viscosity. In CVD reactors it is always very low and so the flow results to be laminar.

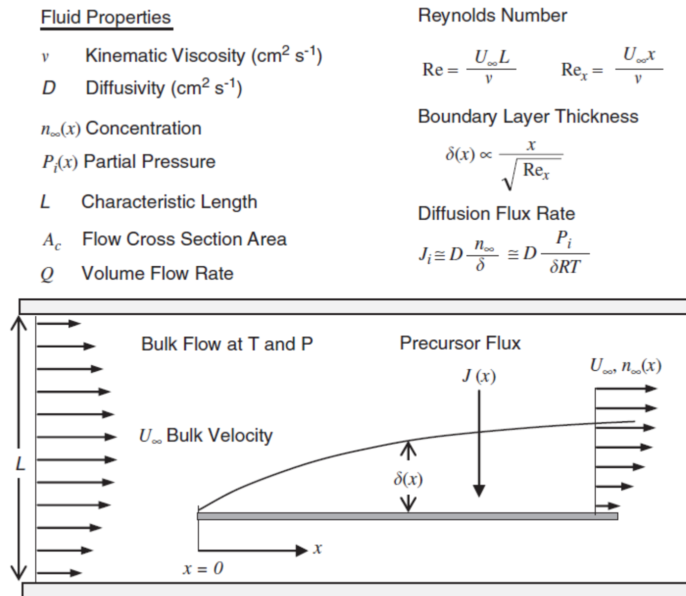

Figure 2.4: Basic flow model for a flat substrate in a horizontal tube reactor in the viscous regime [48].

This model has been expanded by *Strano et. al.* in order to facilitate the calculations of concentration and mass transfer coefficients using engineering correlations [49]. However, as described above, the growth mechanism in the CVD reactor is influenced by many parameters and an their subtle variations can lead to different results, particularly for 2D TMDs growth.

2.3 Mechanism of growth for TMDs

After the sublimation of precursors and their transportation downstream by the carrier gas, they diffuse from the bulk vapour towards the substrate and there they can be absorbed, diffuse along it and react to form product structures. Metal atoms have an higher sticking coefficient with respect to the chalcogen atoms [50] due to their intrinsic heavier nature. Instead, chalcogens atoms are more volatile and tend to easily desorb from the substrate.

A TMD crystal can have both metal terminations, thus formed by one plane of atoms, or chalcogen terminations, made up by two planes of atoms. According to the Wulff construction, the edges that grow slower are the final ones, while the faster ones disappear with time. Therefore, since the Mo-zz and the S-zz faces are the lowest energy faces they grow the slowest and so are the dominant ones during growth (Figure 2.5) [49]. Hence, the crystal shape (equilateral triangular, truncated triangular and hexagonal) depends on whether the rate of growth of one face is higher or lower with respect to the other.

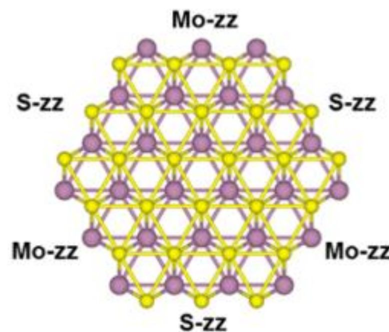

Figure 2.5: Hexagonal MoS_2 crystals alternating Mo-zz and S-zz faces [49].

Thanks to an important experimental study by *Wang et. al.*, it is now possible to correlate the crystal shape (and thus the predominant growth rate) to the stoichiometry of the precursors [51]. In accordance to this, if the supply of precursors is stoichiometric, then the crystal would be hexagonal with three M-edges and three X-edges. On the contrary, the crystal would result triangular

with only one type of edge, when there is excess of one of the precursors as can be seen in Figure 2.6.

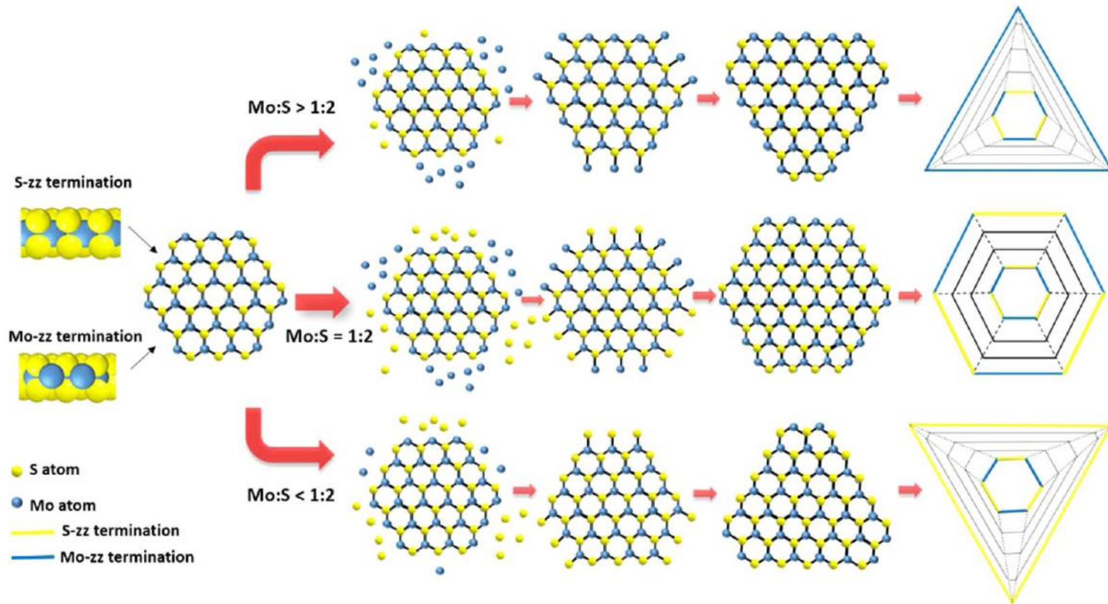

Figure 2.6: Wulff construction and the relationship between Mo:S atom ratio and domain shape [51].

An interesting insight into the growth kinetics of 2D materials, especially if synthesised by CVD, has been reported in a recent study by *Dong et. al.* [52]. They analyse the single crystal growth and assert that it can be classified in:

- Attachment limited growth regime
- Diffusion limited growth regime

The former refers to a regime in which the precursor concentration on the substrate is taken as constant and therefore the growth is ruled by the attachment of the precursors atoms at the growing edges of the material (which have to overcome an attachment barrier).

During this growth it is possible to observe triangular, truncated triangular and hexagonal shapes for TMDs.

Instead the diffusion limited growth regime refers to a fast diffusion of precursors species that attach to the crystal edges. In this regime, there will be a depletion zone around the growing crystal and for this reason the growth will be

limited by the diffusion of further chemical species. The crystals formed will have fractal like shapes (middle panel of Figure 2.7). These shapes have been observed in MoS_2 grown on SiO_2/Si [53].

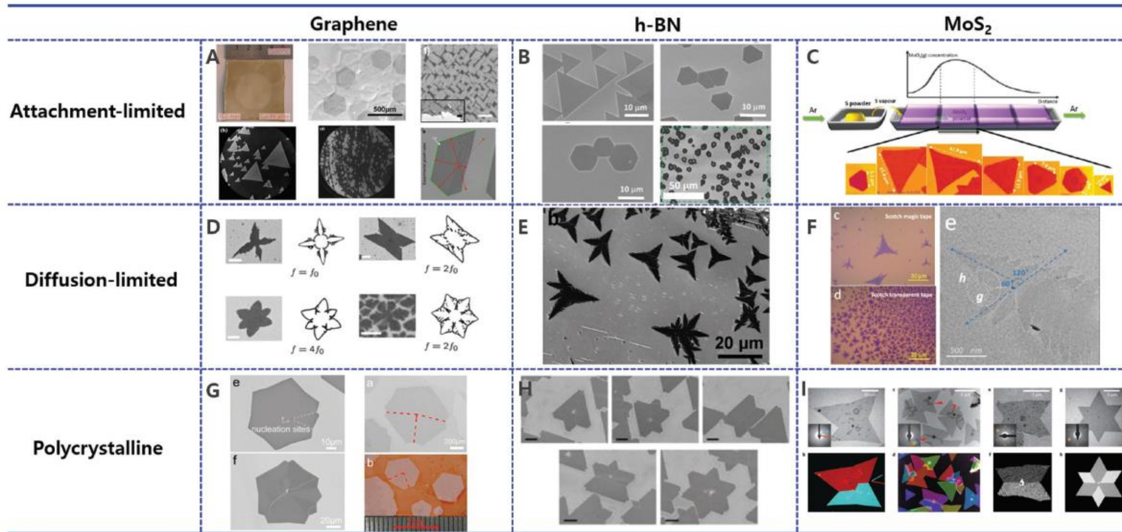

Figure 2.7: The two regimes and the polycrystalline growth analysed for graphene, h-BN and MoS_2, respectively [52].

Another interesting observation regards the polycrystalline growth, which provides different crystals shapes, usually with concave corners at the grain boundaries between single crystalline areas [54]. From the experimental observations of *Guo et. al.* on the coalescence of grain boundaries in graphene (image bottom-left form Figure 2.7), they identified two possible growth paths.

If the nucleation of single crystalline domains occurs at different sites and different time (Figure 2.8 left), the intersection point of grain boundaries will spread in the polycrystalline domain. Instead, if the nucleation occurs simultaneously from the same site (Figure 2.8 right), all the grain boundaries will intersect at the centre of the polycrystalline domain [55].

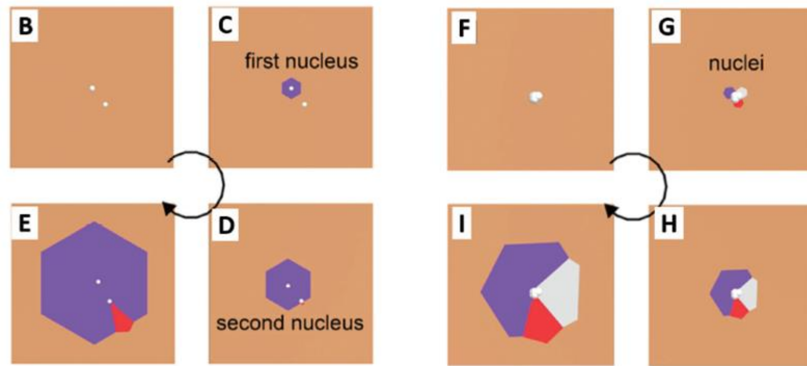

Figure 2.8: Left: Nucleation at different sites and times. Right: Nucleation at the same site and simultaneously [52].

This model is also applicable for other 2D materials other than graphene, such as TMDs [56].

Three potential ways to enlarge the crystal domains and obtain single crystalline 2D materials are suggested [52]:

1. Make only one nucleus develop into the final product on the substrate.
2. Ensure that all the nuclei have the same crystalline orientations in order to avoid the formation of grain boundaries during coalescence (by the choice of a lower symmetry substrate).
3. Post-treatments can turn the polycrystalline film into a single crystal.

Chapter 3

Experimental details

3.1 CVD experimental set-up and procedure

For the synthesis of the materials, a standard laboratory CVD set-up has been installed under a fume hood.

The CVD equipment is composed of a quartz tube with diameter of 3 cm and length of 1 m, which is accommodated inside two distinct furnaces. The main one (F1), which can be manually opened, has a parallelepiped shape, while the smaller one (F2) is closed and has a cylindrical shape (Figure 3.1).

The edges of the reaction tube are connected, one to a rotary vane vacuum pump, which can reach the lower value of 0.220 mbar, while the other to an argon cylinder, which acts as inert gas flux. A valve controls the supply of Ar gas in the tube.

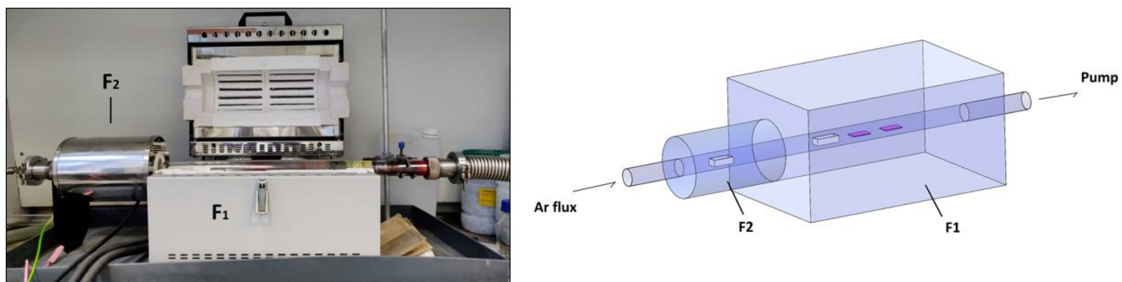

Figure 3.1: Real and schematic of the CVD set-up used.

The furnaces are activated by two different controllers that regulate independently the temperature. Both the controllers are set at the heating rate of 25 °C/minute.

Both the precursors of the transition metal and the chalcogen, as well as the substrate, are accommodated inside the tube of reaction. Two distinct furnaces are used; the position of the precursors varies with their vapour pressure dependence on temperature.

The procedure starts with the tube cleaning, by a long brush using a paper towel and acetone and then water. This would try to prevent contamination or other related issues during the reaction process.

Then, the silicon substrate is prepared. We use a silicon wafer having an external thermally grown 300 nm layer of SiO_2 on Si and a diameter of 10 cm, from which we cut two substrates of length 3-4 cm and width 2.8 cm, in order to accommodate them inside the tube, by the use of a diamond tip pen. Previously the insertion inside the quartz tube in the main furnace, the SiO_2/Si substrates are carefully cleaned by acetone and distilled water and dried by a nitrogen flux in order to avoid any visible glow or contamination trace. Finally, the precursor powders are weighed, placed inside ceramic crucibles and inserted in the tube.

After the equipment has been set, the main furnace closed and the tube properly connected to the pump and the Ar cylinder, the pump is activated and brought to the maximum vacuum value, in the order of 0.220 mbar, and maintained for 30 minutes. This will allow the pump to be stabilized on its lowest value and at the same time to eliminate and desorb some residual organic molecules. After this, we activate the Ar flux (150-200 sccm) and we switch on the main furnace (F1). After a temperature of 200 °C is attained, the very same temperature is maintained for 30 minutes; this "purging step" further avoids the presence of contaminants. At this point, a pressure of ~1.8 mbar is settled in the tube.

The function of the inert gas flux is to transport the sublimated precursors on the substrate, making them able to react there. After this period we decrease the Ar

flux to 100-150 sccm, while the heating of the main furnace keeps increasing constantly till the maximum temperature we have set. During this ramp, we need to activate the secondary furnace at the appropriate time, in order for both the furnaces to reach the maximum temperature simultaneously. This is extremely important due to the fact that, in theory, the sublimation of powders will start at the same time and it will promote the reaction at the right temperature. The latter, namely the time of deposition, will be set in advance and, after it, the main furnace will be quickly opened to stop the deposition reactions by a rapid cooling down.

During the cooling down, this procedure is followed:

- The Ar flux and the pump will keep working till the tube becomes touchable and ready to be handled.
- Both inert flux and pump are shut down.
- The tube is set free from the vacuum; this operation will permit to all the vapours and residues of reacting gases to be oxidized and aspirated from the fume cupboard.
- The crucibles and the substrates are carefully removed from the tube to be catalogued and ready to be characterized.

3.2 Raman spectroscopy and photoluminescence (PL)

Raman spectroscopy is a versatile, non-destructive and high-throughput spectroscopic methodology for characterizing atomically thin materials. This technique relies on the inelastic scattering of incident monochromatic light in the visible, near infrared and near ultraviolet range by the sample, due to interactions between the incident light and lattice vibrations (phonons).

In a typical Raman spectrometer, the sample is irradiated with a laser beam. The electromagnetic radiation interacts with the electrons of the molecules and induces an oscillating electric dipole on them, responsible of the diffusion of the radiation. As a matter of fact the photons of the radiation can be:

- elastically scattered (the majority), so they maintain the same wavelength, of the excitation source but will have different direction. This is called Rayleigh radiation and it is filtered out by using a filter.
- inelastically scattered (only a small fraction), thus the energy of photons is not conserved. This will cause a red or blue shift in the frequency of the photons called Stokes or anti-Stokes, respectively. The energy shift of the scattered photons is expressed in cm^{-1} and it depends on the specimen electronic structure and phonon dispersion.

The energy lost by the incident photons is dispersed as phonons, collective excitations in a periodic arrangement of atoms or molecules in a condensed matter. Therefore, by analysing the photons scattered by the sample, it is possible to acquire information about the vibrational modes in the material.

The same experimental setup can also be used to detect light emitted (photoluminescence) from semiconducting materials excited through a light-source with larger energies than the materials band-gap.

Photoluminescence refers to light emission after the excitation of the material through optical stimulation (absorption of photons). It is a non-destructive

technique, easy to perform and usually available in a laboratory. A schematic of the process is show in Figure 3.2.

An electron absorbs the impinging light at some wavelengths and it is promoted to a higher energy level. In the case of semiconductors, this jump corresponds to the excitation of an electron from the valence band to the conduction band, with the creation of an electron-hole pair. The system then undergoes a non-radiative internal relaxation thanks to which the excited electron moves to a more stable excited level, such as the bottom of the conduction band. At this point the formation of an exciton occurs (bound state between the hole and the electron) and after a certain time, called exciton lifetime, the electron comes back to the ground state and recombines with the hole.

By this last transition, the energy released by the recombination results in radiative emission; the emitted photon has a wavelength larger than the incident one because it has lost energy. At room temperature, the PL emission is broadened usually by ~ 25 meV, but it can be reduced by lowering the temperature for the measurement.

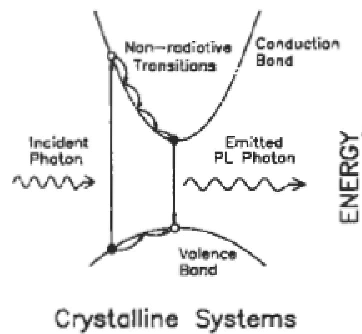

Figure 3.2: Schematic of PL process [57].

All the measurements were carried out at room temperature in atmospheric conditions. Raman and PL spectra were performed by Renishaw inVia Raman Microscope equipped with a 532 nm laser and a Renishaw Raman spectrometer equipped with a 738 nm laser. Specifically, Raman spectra and PL spectra were

collected by a 2400 mm^{-1} grating. The silicon Raman mode at 520 cm^{-1} was used for calibration prior to measurements. Data analysis was done by using Origin and MATLAB software with already provided scripts by group members.

3.3 X-ray photoelectron spectroscopy (XPS)

The X-ray photoelectron spectroscopy is a non-destructive surface sensitive spectroscopic technique that allows the determination of the chemical composition and quantification of materials surfaces. It measures the energy distribution of electrons ejected from a material by means of an X-ray excitation (Figure 3.3). These electrons, coming from core and valence levels of our material, identify the elements present in the sample from their binding energies (BE), characteristic of each material.

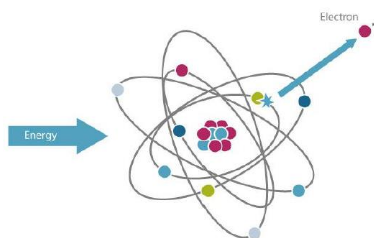

Figure 3.3: Schematic of core electron ejection by means of an x-ray radiation [Notes form a characterisation course].

Due to the fact that atoms in a compound are bound together, it means that the electron binding energy is influenced by the presence of the surrounding atoms. For this reason we have to introduce a work function Φ that is the difference in energy between the Fermi level (the energy of the highest occupied energy level) and the vacuum level (the energy required to the electron to escape its atom and being no more bound to it). Usually the energy given to the system is larger than this value, so the electron ejected will use the extra energy as kinetic energy to move towards the detector. The kinetic energy will be, thus: $K = h\nu - E_b - \Phi$,

where $h\nu$ is the photon energy, while E_b is the binding energy and Φ is the instrument work function, which is known. Thus, it is possible to solve the equation and obtain the E_b for our system.

The final spectrum will be a function of the intensity of the signal (number of electrons detected) versus their binding energy (eV). The significative information is linked to the electrons that, once ejected from their atom, interfere only elastically, so where the kinetic energy is conserved. These electrons come from the superficial atoms and are the ones of interest for the measurement. The mean free inelastic path is an index of the maximum depth from which we can record a significative information and it is in the range of 10 to 50 nm. All the other electrons, which will arrive to the detector with lower kinetic energy, will be recorded too and they will have energies randomly distributed from zero to the energetic maximum, constituting a uniform background at the high binding energies (low kinetic energies).

As each element produces a characteristic set of spectral peaks at characteristic binding energy values, which correspond to the electron configuration of the specific atoms (such as 1s, 2s, 2p, 3s etc.), the elemental composition of the sample surface can be determined. Further, as the number of detected electrons for each spectral peak is directly related to the concentration of the elements within the XPS sampling volume, atomic percentage values can also be calculated.

Core levels in XPS use the nomenclature nl_j, where n is the principal quantum number, l is the angular momentum quantum number and $j = l + s$ (where s is the spin angular momentum, having values ± ½). Therefore, all orbital level except for the s levels (where l = 0) give rise to a doublet with the two possible states having slightly different binding energies. This phenomenon is known as spin-orbit splitting. Moreover, specific area ratios are present between doublets.

Measurements were performed on a Thermo Fisher K-Alpha+ spectrometer equipped with a monochromated micro-focused Al$K\alpha$ x-ray source. The measurements were performed at room temperature using a 20 eV energy pass

with energy step of 0.1 eV. Binding energies were calibrated using a C 1s peak at 284.6 eV. XPS spectra were analysed using the Avantage software package and plotted with Origin. All peak positions were assigned with reference to the NIST X-ray Photoelectron Spectroscopy Database.

3.4 X-Ray diffraction (XRD)

X-ray diffraction (XRD) is another non-destructive technique mainly used to determine the crystalline structure of a material (Figure 3.4). The diffraction of x-rays by a periodic atomic structure of a material allows the study of its crystallinity. This occurs via analysis of the specific directions of the crystal atoms-induced diffraction of an incident x-ray radiation along the lattice planes, on the bases of the Bragg's law, which states that the diffraction angle is related to the distance between the reflecting planes: $2d \cdot sin\theta = n\lambda$.

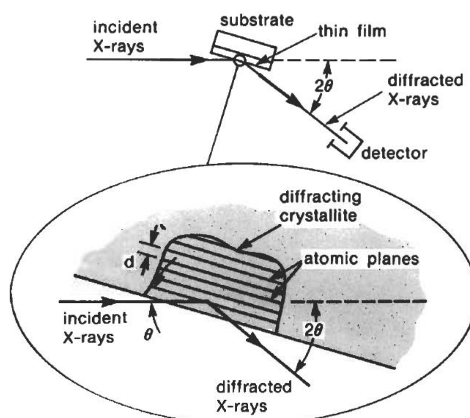

Figure 3.4: Basics of a typical XRD experiment [57].

Due to variations in the lattice parameters for different chemical compounds, the diffraction angle is thus characteristic for a given material. A database of known crystalline structures is necessary to fully understand the diffraction pattern the machine gives us.

The XRD machine used was a PANalytical X'Pert PRO diffractometer using a Cu anode creating a Cu-Kα x-ray radiation (1.5418 Å). X-rays have energy in the order of 18 keV and all the radiation are suppressed using Ni filter. Scans were performed in the 2θ range 10-65° with a typical step size of 0.033°. X'Pert Highscore plus software was used to match the database.

3.5 Scanning electron microscopy (SEM)

SEM imaging is carried out by impinging a high-energy (1-30 keV) focused electron beam under high vacuum (< 10^{-5} mbar) onto a sample and detecting the scattered electrons in the vicinity of the surface. The incident electron beam interacts with the sample generating backscattered electrons, secondary electrons, Auger electrons, characteristic X-rays, fluorescent X-ray and continuum X-ray. We have exploited backscattered electrons and secondary electrons to gain information about the CVD grown ZrS_2 films. Backscattered electrons are a small fraction of the beam electrons which undergo elastic scattering with the atoms of the sample, while secondary electrons are the result of the inelastic scattering between the beam electrons and the sample atoms. In backscattered electron (BSE) imaging mode, a special detector can select predominantly BS electron to form an image of the sample where the spatial resolution is limited to ~ 100 nm. While using a another detector to selectively collect secondary electron (SE), the spatial resolution that can be achieved is ~ 2-10 nm due to the much smaller sampling volume of the secondary electrons as compared to the backscattered electrons. Due to detector proximity to the sample surface and high sensitivity to low-energy secondary electrons (< few tens of eV), SEM allows for high-contrast imaging of atomically thin materials such as graphene and TMDs, in particular at low voltages and small working distances. In our case the voltage was set to be in the range 5-20 kV in order to obtain sharp images due to a poor signal to noise ratio under 5 kV.

SEM measurements were performed with a Zeiss Auriga field emission scanning electron microscope. Images were acquire at 10 kV accelerating voltage. Another SEM, namely JSM-6010LA Analytical Scanning Electron Microscope, was also used at 20 kV to acquire images and elemental mapping of portions of the surface.

3.6 Transition electron microscopy (TEM)

Transmission electron microscopy (TEM) is a microscopy methodology in which a beam of electrons accelerated at voltages in the range of 60-300 kV is transmitted through an ultrathin specimen (less than 100 nm thick) to form an image of the sample at significantly higher lateral resolution than what achievable with light microscopes. The higher resolution is due to the smaller de Broglie wavelength of electrons which acquire significantly higher kinetic energies as compared to in SEM. The electron beam is usually generated by thermionic emission from a tungsten filament or by field electron emission and it is then accelerated under vacuum (~ 10^{-4} Pa) through an electric potential and focused on the sample using electrostatic and electromagnetic lenses. The transmitted electron beam through the sample contains information about the electron density, phase and periodicity of the sample and it is expanded using projector lenses to form a magnified and focused image onto a fluorescent screen (or other imaging devices). In the typical bright-field imaging mode, the contrast formation at lower magnifications is due to the different absorption of electrons by the sample due to composition or thickness variations. The lateral resolutions typically achieved are in the order of nanometres. Whereas at higher magnifications the image contrast intensities are modulated by complex wave interactions, displaying lateral resolution at the atomic level. As the wavelength of high-energy electrons (100-400 keV) is a few thousandths of a nanometre, whereas the spacing between atoms in a solid is about a hundred times larger,

the atoms of the TEM sample act as a diffraction grating for the incident electron beam.

Samples for TEM analysis were prepared on carbon-coated copper grids. Preliminary low-magnification TEM imaging was performed using a JEOL JEM-2100Plus microscope. HR-TEM images were acquired on a JEOL JEM-2100F microscope with a field- emission gun operated at 200 kV accelerating voltage.

3.7 Energy dispersive x-ray spectroscopy (EDS)

Energy dispersive x-ray spectroscopy (EDS) is a complementary characterisation technique which can be carried out within the same experimental setup of the TEM or SEM by using an electron beam. It can excite a core shell electron and eject it; there, it will be created an electron hole which will be filled by a valence band electron. The decay of the latter electron, from the valence band to the core band, may release x-rays which can be collected by a detector and whose energy is uniquely associated with the transition energy of each element.

EDS was employed to investigate the elemental composition of flakes drop-casted onto TEM grids and also to create the elemental mapping of portions of ZrS_2 films using SEM.

3.8 Selected area electron diffraction (SAED)

By adjusting the magnetic lenses of TEM, a diffraction pattern can be obtained. By inserting a selected area aperture (thin strip of metal containing holes with different sizes) into the beam path below the sample holder, the diffraction pattern from the selected area can be obtained in the reciprocal space. The SAED can be used to identify crystal structures and defects within areas significantly

smaller (several hundred nanometres in size) than what achievable through X-ray diffraction (several centimetres in size).

3.9 Absorption spectroscopy

Absorption spectroscopy is a characterisation technique able to measure the absorption of a radiation source after the interaction with the sample. The physical mechanism is based on the fact that the impinging photons have a specific energy. If photon energy matches the energy gap of the molecules present, the photons are absorbed to excite that molecules. Instead, the photons carrying other energies are transmitted and recorded by a detector. The result is an absorption spectrum where we see peaks related to the wavelength of photons absorbed by the material. These frequencies are related to the electronic and molecular structure of the sample, as well as to its crystal structure and the external environment. The interaction between flakes/particles in the dispersion can cause shifts in the absorption peaks. Furthermore, the area underneath the peaks is proportional to the amount of material present in the dispersion.

The machine used was a Cary 5000 UV-Vis-NIR spectrometer with a range of wavelengths from 175 nm to 3300 nm. Before the measurement, a baseline is performed, where just the absorbance of the empty cuvette is recorded. After it, usually the same measurement is done other two times:

- One just with the pure solvent in which our sample is dispersed. We record the 100% transmittance or, in other words, we subtract its absorbance signal from the spectrum, as if it was 100% transmitted.
- The other with a metal sheet to record 0% transmittance and to make sure that the beam is in the right position.

Then, the absorption measurement is carried out on the dispersion containing our material. In our case, the sample was sonicated in the solvent for tens of minutes, to obtain flakes dispersed in it.

Chapter 4

Synthesis and characterisation of TMDs

4.1 Introduction

This chapter will cover the procedures used to synthesise tungsten disulphide, tungsten diselenide, zirconium disulphide and ZrS_xSe_{2-x}, as well as their characterisations.

A general description of the CVD set-up and procedure has been reported in chapter 3.1. The very same set-up will be here proposed again for every material, focusing on the changes in parameters during the process.

The study of tungsten disulphide and tungsten diselenide has been the starting point for the subsequent research on zirconium disulphide, which has never been studied in this group before and, because of its interesting properties, it will be the central part of my work. As very few papers are available on this topic, my research for the synthesis of ZrS_2 has been rooted on already existent knowledge of MoS_2, WS_2 and WSe_2 fabrication in the group. The choice of different synthesis parameters, such as temperature, precursors quantity and growth time, therefore, originates from the syntheses of other TMDs and it has been optimized for the new requirements of ZrS_2. Variations of CVD parameters will be discussed, highlighting advantages or disadvantages of each choice, keeping in mind the limiting factors of our CVD set-up. Afterwards, results and

characterisations are presented and discussed, as well as a short digression on ZrS_xSe_{2-x} alloys.

4.2 Growth of 2D tungsten disulphide WS_2

In order to understand and learn the basic principles of CVD growth of TMDs, I performed some trial syntheses on WS_2 and WSe_2. In the very first experiments, I followed the deposition process conceived by the group itself and reported in a paper [14] for the synthesis of tungsten disulphide. As a matter of fact, this study highlighted how the use of the precursor H_2WO_4 + NaCl was preferable to the use of WO_3 + NaCl or the WO_3 alone, as transition metal source, to obtain WS_2 monolayers, as shown in Figure 4.1.

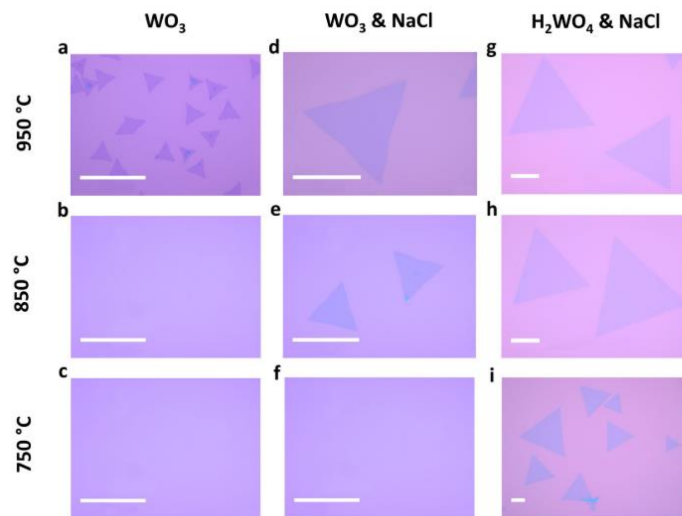

Figure 4.1: Optical micrographs of WS_2 nanocrystals grown at different temperatures and from different precursors [14].

The use of alkali metal halides to favour the synthesis of Group VI TMDs has been demonstrated by many authors [15] [58] [59] [60]; they act as growth promoters reacting with metallic oxides to give volatile oxychlorides. In the case of WS_2 synthesis, the following reaction steps have been identified as likely to occur:

1) $H_2WO_4(s) \rightarrow WO_3(s) + H_2O(l)$
2) $NaCl(s) + H_2O(l) \rightarrow Na^+(aq) + Cl^-(aq) + H_2O(l)$
3) $6Na^+(aq) + 6Cl^-(aq) + 14WO_3(s) \rightarrow Na_2W_4O_{13}(s) + Na_2W_6O_{19}(s) + Na_2W_2O_7(s) + WOCl_4(g) + WO_2Cl_2(g)$
4) $WOCl_4(g) + WO_2Cl_2(g) + S(g) + H_2O(g) \rightarrow WS_2(s) + SO_2(g) + H_2SO_3(g) + HCl(g) + S(g)$

In the third reaction step, where the metal oxide reacts with the salt, there is an increase of the volatility of the metallic species (by the formation of volatile metal-oxyhalide species). This significantly lowers the temperature for the overall reaction with respect to the metallic precursor without the use of alkali metal halides. The presence of intermediated solid compounds such as $Na_XW_YO_Z$ is always found in the crucible after the deposition process, because they possess high evaporation temperatures; their chemical nature was later confirmed by XRD studies [14]. Instead, the formation of oxyhalide species in the vapour phase, such as WO_2Cl_2 and $WOCl_4$, has been reported for the synthesis of WS_2 bulk crystals via chemical vapour transport [61], by reacting halogen molecules, used as transport agents, with tungsten oxides.

The aim of my experiments was to obtain large WS_2 monolayers with good optical quality and limited presence of defects. I used H_2WO_4 and NaCl powders, mixed 1:1 w%, and sulphur powder as precursors.

The procedure has been extensively described in Chapter 3.1; here we report the choice of parameters used during the multiple syntheses with similar positive results:

	Quantity (g)	Temperature (°C)	Furnace	Ar flux (sccm)	t_{dep} (min)	P_{dep} (mbar)
H_2WO_4+NaCl	0.3-0.4	825-850	F1	200→100	15	1.4
S	3	125	F2	//	//	//

Table 1: Precursors and parameters chosen for the synthesis of WS_2 monolayer crystals.

As we can see, the quantity of sulphur is even ten times higher than the metal precursor; this is due to the fact that, among the chalcogens, sulphur, because of its intrinsic low molecular weight of 32.066 g/mol, has a lower sticking coefficient, thus it is easier to be desorbed by the substrate. For this reason, increasing its quantity we try to increase the probability for it to attach to the surface of SiO_2/Si.

Regarding the procedure, due to the fact that a proper thermal insulation is not obtainable, a temperature gradient is present inside each furnace. For this reason, both the crucibles containing the precursors were put in the middle of each furnace (Figure 4.2). Moreover, the metal precursor crucible and the substrate were placed close to each other in the main furnace (F1): the crucible in the middle, the substrate more downstream. This is the optimised position demonstrated by previous studies in the group.

To remark as fundamental, the sulphur powder heating profile has been set to reach the maximum temperature, and so maximum supply, when the W-precursor starts to sublimate. The time of deposition has been reported as optimal for the realization of this TMD [14].

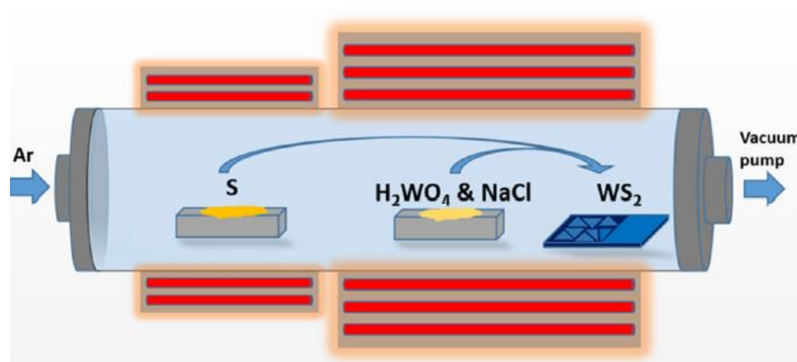

Figure 4.2: CVD set-up for the synthesis of WS_2. On the right the main furnace (F1), on the left the secondary furnace (F2) [14].

4.2.1 Characterisation of WS_2

The first characterisation always performed on the samples after the synthesis is the optical microscopy; thanks to this tool we are able to identify if something has effectively grown on the substrate and, at the same time, we can already spot some mono- or few-layers (Figure 4.3). The features of mono- and few-layers are recognizable by the low contrast with respect to the SiO_2/Si refractive substrate, proving their thinness, whereas darker colours refers to thicker flakes. The defined trigonal geometry confirms the hexagonal symmetry of the crystals.

The results I obtained in terms of crystal size and purity are comparable to the ones in well-known papers [15] [19] [60] .

Figure 4.3: Optical image of WS_2 mono- and few-layers. The monolayers are indicated with white arrows. Scale bar: 50 µm.

We performed Raman spectroscopy to identify the material and count the number of layers. We need to take into consideration the active Raman modes in our material (see Chapter 1.4).

All the spectra, analysed with a 532 nm laser excitation, exhibit the two characteristic peaks located at 351 cm^{-1} and 417 cm^{-1}, which can be attributed to 2LA(M)-E^1_{2g} and A_{1g} vibrational modes of pristine WS_2 monolayer. The longitudinal acoustic (LA) mode, 2LA(M), refers to in-plane collective movements of the atoms in the lattice, periodically compressing and expanding

the lattice [62]. It is a second order Raman mode due to LA phonons at the M point of the Brillouin zone [35] and merges together with the E^1_{2g} mode. In Figure 4.4, we report a typical Raman spectrum for a monolayer triangular crystal of WS_2 with labelled peaks.

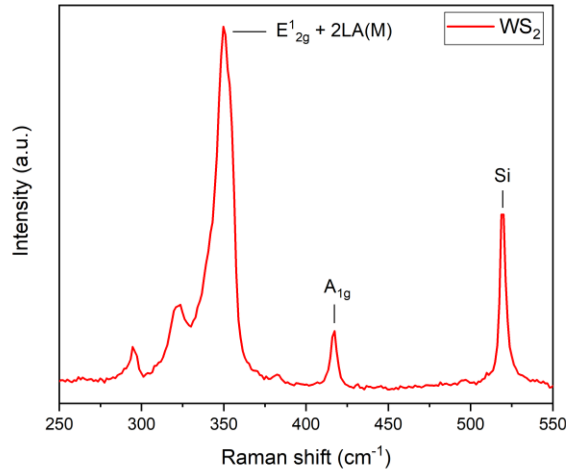

Figure 4.4: Raman spectrum of a WS_2 monolayer crystal labelled with characteristic vibrational modes.

Furthermore, correlating the monolayer spectrum with one of a few-layers, we observed that the relative intensities of 2LA-E^1_{2g} and A_{1g} modes have opposite behaviour with respect to the layer increase, as reported by *Berkdemir et. al.* [62]. The former increases in intensity by decreasing the number of layers, till reaching a maximum for the monolayer, whereas the latter shows an increment of intensity going form monolayer to few-layers.

From Figure 4.5 (left) we can also see the shift of the two characteristic peaks positions increasing the number of layers, as we said in Chapter 1.4. As reported by *Terrones et. al.*, the A_{1g} blueshift, when the number of WS_2 layers increases, can be correlated to the increase of the restoring force caused by van der Waals interactions among layers [62], while the shift of the other peaks is quite subtle (Figure 4.5 right). A Raman shift of 2.59 cm^{-1} was obtained from the experimental graph below, which is higher than the spectral resolution of the instrument (~ 1 cm^{-1}).

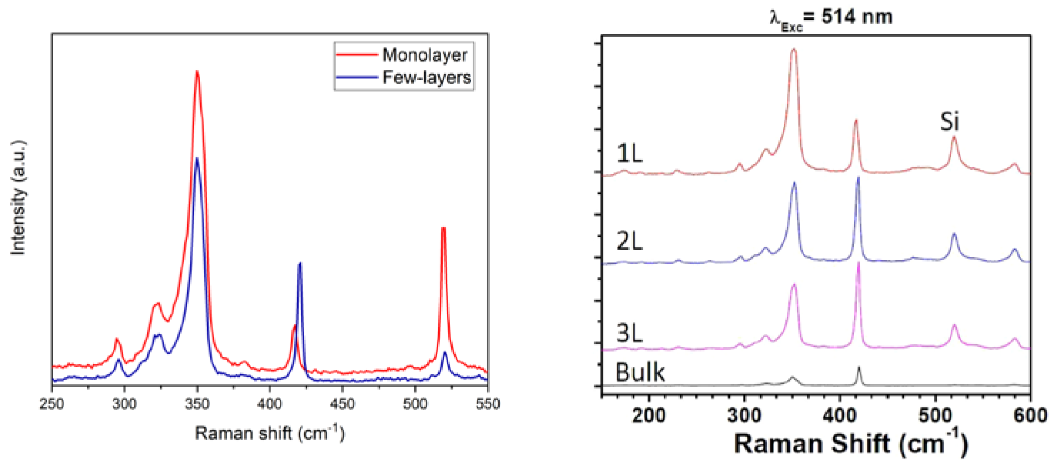

Figure 4.5: Left: Comparison of Raman spectra of a monolayer and a few-layers crystal. Right: Raman spectra of WS_2 for 1L, 2L, 3L and bulk [62].

Photoluminescence analysis was performed on monolayer crystals; the peak position appears at energies in the range of 1.97-2 eV emitting in the red-orange part of the visible spectrum. These values are consistent with the monolayer nature of WS_2, as reported in literature [14]. The value of the FWHM is 36 meV, which corresponds to a lower density of defects in the sample compared to other techniques (Figure 4.6). The peak appears to be asymmetric due to a contribution coming from trionic recombination. A trion is a localized excitation consisting of three charged quasiparticles. This is due to the presence of S vacancies that has been reported to increase the electron density, thus the trions population. Trionic recombination appears as a PL emission at lower energies than the optical band gap with a consequent increase of the FWHM.

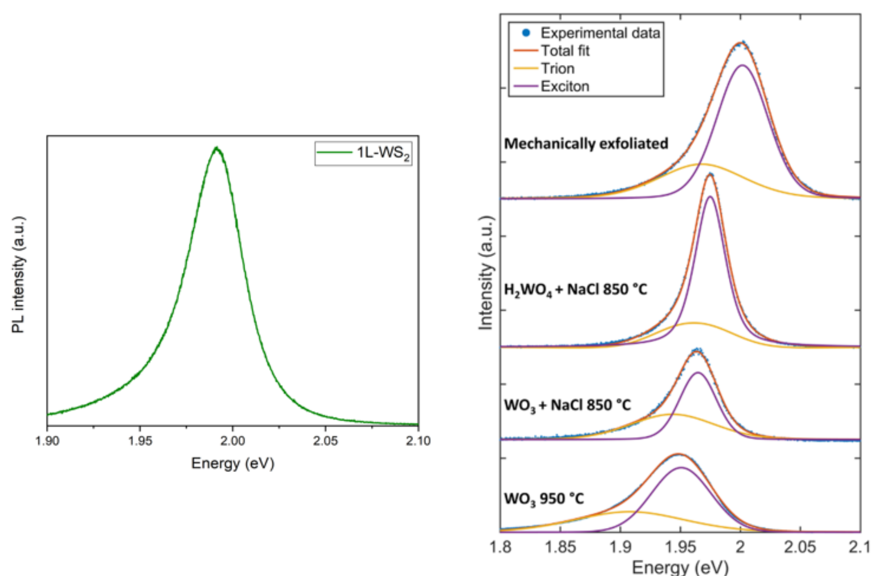

Figure 4.6: Left: PL spectrum for 1L-WS_2, peak position at 1.99 eV. Right: PL spectra characteristics of WS_2 grown using: WO_3 at 950 °C, WO_3 + NaCl at 850 °C and H_2WO_4 + NaCl at 850 °C compared to the PL of a mechanically exfoliated sample. Individual spectra (dotted line) and deconvolution in exciton and trion components are shown [14].

4.3 Growth of 2D tungsten diselenide WSe_2

As part of the same group of TMDs, WSe_2 and WS_2 share many characteristics from the synthesis point of view and final results. The parameters and precursors chosen for tungsten diselenide growth were identified by previous researchers in Mattevi's group [14] [63].

Always following the metal-halide assisted synthesis, already discussed for WS_2, in this case the chalcogen precursor in powder, selenium, results to have low reactivity, making the CVD reaction more problematic. To solve this problem without the use of H_2 as carrier gas, the choice for the Se-precursor was to use ZnSe. This compound contains Se in the same oxidation state as WSe_2 itself, that is Se^{-2}, avoiding in this way the need of a reducing agent as H_2. For the synthesis procedure, I used tungstic acid plus salt and zinc selenide, 0.15 g and 0.30 g respectively. All the other parameters such as time of growth, pressure and Ar

flux are the same used in the synthesis of WS_2 (Table 2). The only difference, a part from the chalcogen precursor, is the use of a single furnace to store both precursors and silicon substrate. This is due to the fact that the sublimation temperature of ZnSe is similar to the one of H_2WO_4 (~ 850 °C at 1.4 mbar); in this way the precursors crucibles are located in the upstream are of the main furnace, while the substrates in the middle of it.

	Quantity (g)	Temperature (°C)	Furnace	Ar flux (sccm)	t_{dep} (min)	P_{dep} (mbar)
H_2WO_4+NaCl	0.15	850	F1	200→100	15	1.4
ZnSe	0.30	//	F1	//	//	//

Table 2: Precursors and parameters chosen for the synthesis of WSe_2 monolayer crystals.

4.3.1 Characterisation of WSe_2

The synthesis process led to a reproducible growth of WSe_2 crystals but in some cases also to the formation of mm^2-sized polycrystalline films starting from the edges of the substrate. Nucleation preferentially initiates at edges and at substrate defects (Figure 4.7: a. ; b.), as reported in literature [64].

In Figure 4.7 a. we observe the massive nucleation at the edge of a silicon substrate, as well as in image b., showing a surface scratch. These sites have higher energy, so atoms would preferentially attach to them in order to decrease the total energy and start the crystal growth. Regarding image c. and d., they represent polycrystalline films of WSe_2. Image c. shows the meeting line between two polycrystalline layers grown with different nucleation densities; the left part shows larger crystals than the right one. Another example of thick polycrystalline layer is shown in image d. of Figure 4.7.

AFM characterisation, performed by other members of the group, gave the proof of monolayer crystals growth, measuring a step edge of 1 nm. This value is slightly larger than the theoretical one (~ 0.7 nm) but this is attributed to the roughness of the amorphous SiO_2, which can increase the effective height of the flake.

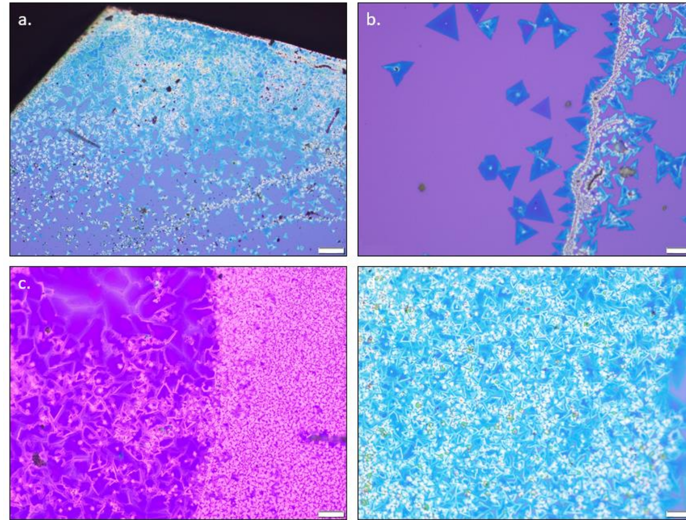

Figure 4.7: Micrographs of WSe_2 crystals and polycrystalline parts. a. Corner of an SiO_2/Si substrate where nucleation density is high; b. Substrate scratch acts as nucleation centre; c. Polycrystalline film with different nucleation density areas; d. Homogeneous polycrystalline film. Scale bars: a. 20 µm, b. 50 µm; c. 50 µm; d. 50 µm.

We have been able to obtain monolayers of WSe_2 having lateral size of 30 µm while thicker ones can reach dimensions of 80 µm (Figure 4.8). Comparing these results with the literature, our monolayer crystals have greater dimensions than the majority of papers [65] [16] [46].

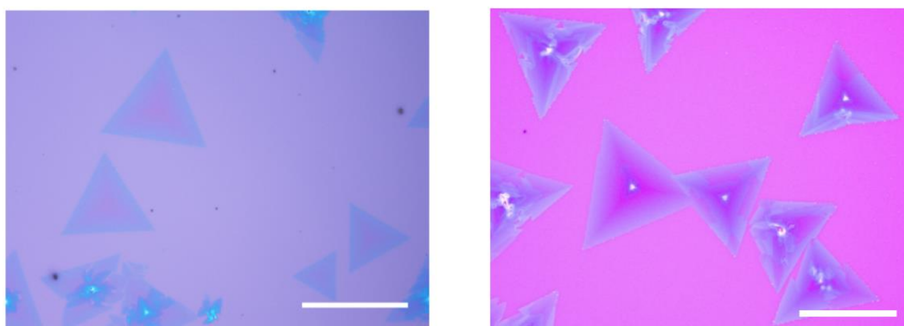

Figure 4.8: Optical microscopy of WSe_2 monolayers (left) and thicker layers (right). Scale bars: 50 µm.

Spectroscopic studies on the vibrational modes using a λ=532 nm laser demonstrated the characteristic features of our material. The Raman spectrum fingerprints of WSe_2 comprise the already mentioned 2LA(M) mode at 259 cm^{-1} and the A_{1g} and E^1_{2g} modes; these last two are degenerate in the monolayer and generally merge together in few-layers at 250 cm^{-1}. Furthermore, a peak at ~ 304-310 cm^{-1} is absent in the 1L form but appears from the 2L on; we refer to it as a "breathing mode" (B^1_{2g}) because of its probable relation with the vibrations among multiple WSe_2 layers [65] [46]. Comparing the two Raman spectra of Figure 4.9, we can state that the left one is a WSe_2 monolayer crystal, while the right one is a few-layers WSe_2 crystal because of the appearance of the B^1_{2g} mode.

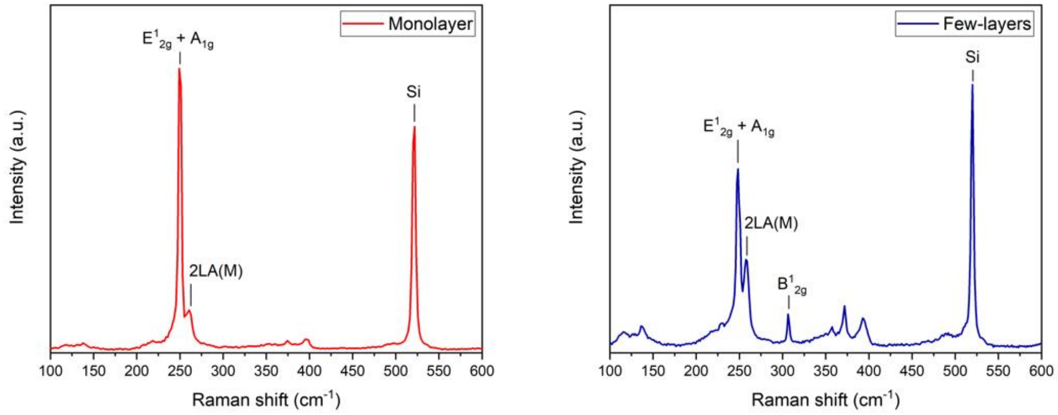

Figure 4.9: Raman spectrum of WSe_2 monolayer (left) and few-layers (right), labelled with characteristic vibrational modes. The 520 cm^{-1} peak refers to the silicon substrate.

The photoluminescence peak appears at 1.65 eV for the monolayer, ~ 751 nm in the visible range close to the NIR [5] [16] [66], as shown in Figure 4.10. The calculated FWHM is in the range of 50 meV, which is very close to the widening usually attributed to thermal contributions due to the laser excitation; this result makes our flakes among the best CVD grown flakes, in terms of defects, strain, doping and other factors contributing to the peak shift.

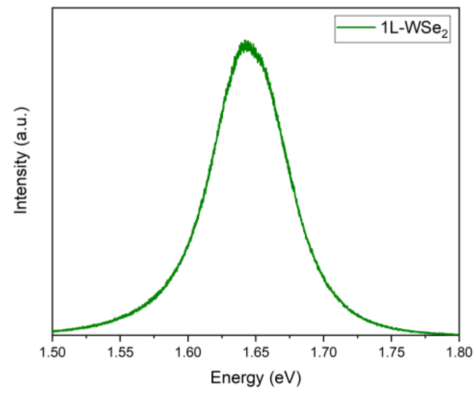

Figure 4.10: PL spectrum for 1L-WSe_2. The maximum of the peak is positioned at 1.65 eV.

4.4 Zirconium disulphide

The main aim of the project was the synthesis of ZrS_2 monolayer crystals of large areas. I refer to Chapter 1.2.2 for the state-of-the-art of the fabrication.

For this reason, the calculation of precursor vapour pressure should be indicative as well as a uniform theoretical flux of Ar in the tube.

Trying to deal with all the parameters described in a previous chapter, in the following section I will describe the process to optimize the growth, following all the variations performed and their relative results. Then, I will analyse the growth on substrates, such as SiO_2/Si, gold and sapphire as well as an alternative precursor for the synthesis. In the end, the characterisations of the most successful samples is described and commented.

4.4.1 Experimental trials for the sublimation of $ZrCl_4$

To date, the literature available for the CVD synthesis of ZrS_2 mono- and few-layers counts two principal references [24][25]; these researchers carried out the CVD synthesis process using $ZrCl_4$, preferentially chosen because of its higher volatility with respect to the oxide-precursor, ZrO_2. The other precursor is always sulphur powder and both are placed in the reaction furnaces. The Zr-precursor was weighted inside a glovebox, as it may react with the air moisture releasing HCl and degrading the precursor itself, placed into vials and then cautiously transferred under the fume hood and into the crucible. The controlled atmosphere of the glovebox allowed the preservation of the precursor.

To carry out the synthesis, the first issue to be solved it was assessing the volatility of $ZrCl_4$ powders. Referring to the literature [24][25], the authors of the two papers chose two different temperatures for the sublimation of $ZrCl_4$. As a matter of fact, they based their studies on two different vapour pressures for

$ZrCl_4$; the *Wang et. al.* referred to an empirical study [67], while *Zhang et. al.* to the Clausius-Clapeyron equation:

$$\ln\left(\frac{p_2}{p_1}\right) = \frac{\Delta_{sub}H_m}{R}\left(\frac{1}{T_1} - \frac{1}{T_2}\right)$$

where $\Delta_{sub}H_m$ is the molar enthalpy of sublimation (110.5 kJ/mol); R is the perfect gas constant (8.314 J/mol · K); T_1 is the sublimation temperature (604.15 K): T_2 is $ZrCl_4$ heating temperature; $p_1$is the atmosphere pressure (101325 Pa); p_2 is $ZrCl_4$ vapour pressure at T_2.

I based my initial experiments on the analysis of these two vapour pressure behaviours for $ZrCl_4$, as an indication of the material to go from a condensed phase to a gaseous one, namely sublimation. In Figure 4.11, I reported the curves for both behaviours: we can see that the empirical curve shows that a minimum temperature higher than 400 °C is needed to make the material sublimate. Instead, according to the Clausius-Clapeyron equation, $ZrCl_4$ sublimates at ~ 150 °C.

The vapour pressure of our $ZrCl_4$ must be considered only as an indication of its volatility and its value depends on surface area, intermolecular forces and temperature.

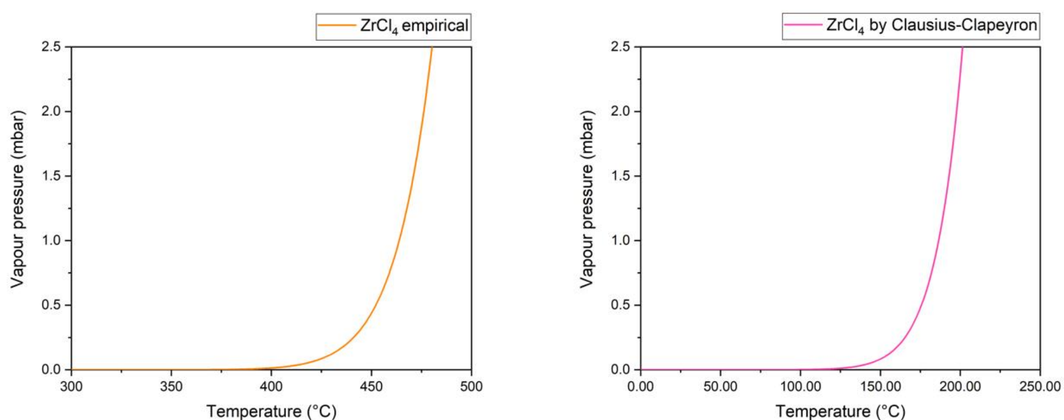

Figure 4.11: Vapour pressure of $ZrCl_4$ empirically calculated (left) and from Clausius-Clapeyron equation (right).

Depending on the two estimated behaviours for $ZrCl_4$ vapour pressure, the decision to make was whether to put $ZrCl_4$ powder in the main furnace (so at high temperatures needed for the substrate diffusion) or in the same furnace as sulphur (in the range of 100-150 °C, where it sublimates). To start, I decided to follow the empirical model, thus to insert the Zr-precursor in the main furnace.

The parameters I used for the first syntheses are summarized in the following table:

	Quantity (g)	Temperature (°C)	Furnace	Ar flux (sccm)	t_{dep} (min)	P_{dep} (mbar)
$ZrCl_4$	0.3	825-875	F1 edge	150→115	15	1.5
S	2	150	F2	//	//	//

Table 3: Precursors and parameters chosen to synthesise ZrS_2, as a first trial.

In order for $ZrCl_4$ not to sublimate too early with respect to S, it was placed at the edge of the main furnace, exploiting the temperature gradient, as shown in Figure 4.12.

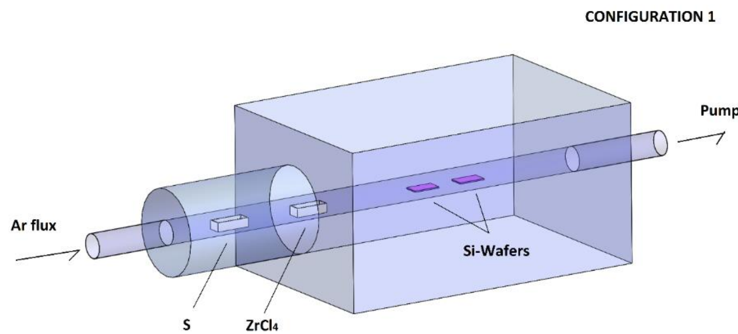

Figure 4.12: 1st CVD configuration.

Multiple experiments changing the temperature of the substrate from 825 to 875 were preformed leading to no suitable deposition of mono- or few-layered crystals.

After that, we tried to focus the experiments on the Clausius-Clapeyron theory, thus placing the Zr-precursor in the secondary furnace with sulphur, always at 150 °C. However, the quantity of zirconium tetrachloride appeared completely unchanged. An explanation could be a too low vapour pressure of $ZrCl_4$ at that temperature. At this point, in order to find the suitable deposition temperature at which both the precursors have the same vapour pressure (meaning the possibility for the two materials to have the same moles in the vapour phase) we performed the calculation of the vapour pressure of both $ZrCl_4$ and of S, with respect to the temperature. The resulting of the vapour pressure for sulphur [30] plotted together with the vapour pressure of $ZrCl_4$ in the Clausius-Clapeyron form, made possible to find an intersection point between them (Figure 4.13). Zirconium tetrachloride and sulphur sublimate with the same value of vapour pressure at the temperature of **213 °C**, hence I decided to use the same value during the experiments. Figure 4.14 shows both S and $ZrCl_4$-containing crucibles in the same furnace (F2).

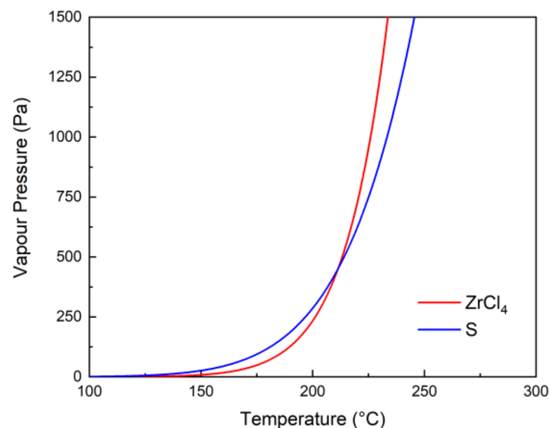

Figure 4.13: Comparison between the S and $ZrCl_4$ curves of vapour pressure vs. temperature. The interception is an indication of the best choice for deposition.

Actually, the secondary furnace (F2) was set at 220 °C, a value slightly higher than the one of the interception of the curves. This was done because of

fluctuations in temperature during periods in which temperature needed to be held constant, particularly during the growth time.

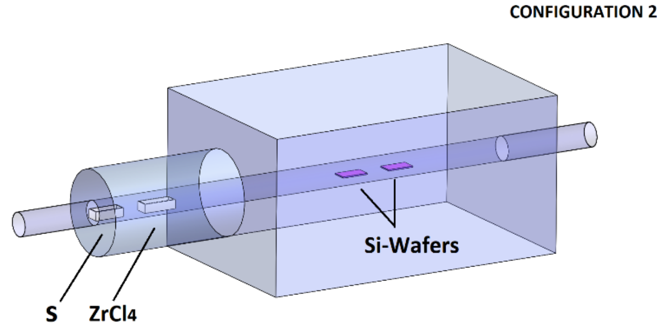

Figure 4.14: 2nd CVD configuration.

The parameters used are the same of the previous experiment, a part form the main furnace temperature which was set at 850 °C (Table 4).

	Quantity (g)	Temperature (°C)	Furnace	Ar flux (sccm)	t_{dep} (min)	P_{dep} (mbar)
$ZrCl_4$	0.3	220	F2	150→115	15	1.5
S	2	220	F2 edge	//	//	//
Wafer	X	850	F1	//	//	//

Table 4: Parameters chosen for the optimized synthesis of ZrS_2.

The ideal temperature of 220 °C worked in depositing our material. The sulphur crucible was found completely empty, while the other one seems to be still filled of $ZrCl_4$, probably because it takes time to sublimate it completely. Anyway, as vapour pressure graph pre-announced, a certain quantity of zirconium tetrachloride was sublimated. The results from this deposition were very positive: even if no single crystal was found on the surface, a complete coverage of the wafer pieces by a polycrystalline film was observed at the optical microscope (Figure 4.15). The film was characterised by Raman spectroscopy, which showed that the material was ZrS_2.

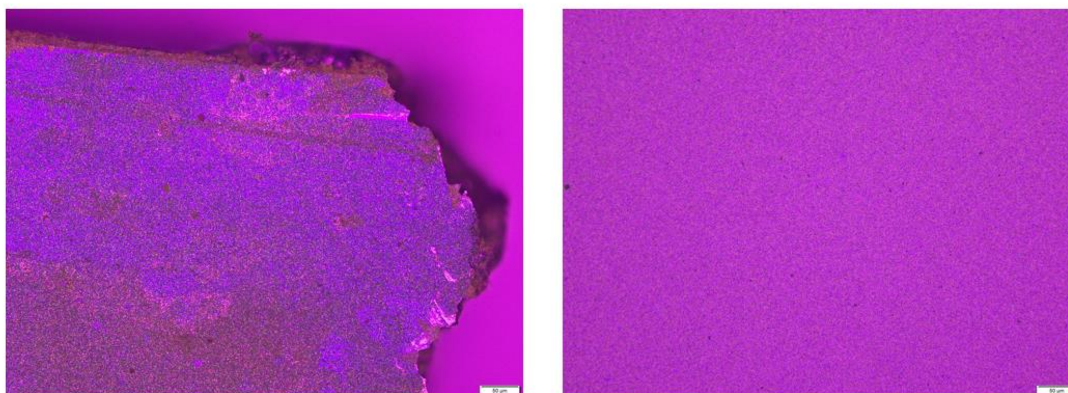

Figure 4.15: Optical micrographs showing the complete coverage by ZrS_2 both on the edges (left) and on the central part (right) of the silicon wafer. Inhomogeneities are visible. Scale bars: 50 µm.

After many syntheses, I found out that the reproducibility of the results was dependent on the periodical substitution of the reaction tube; after 5-6 processes the results were no more obtainable with the same parameters, possibly due to high contamination present in the tube that appear to be visible mainly in the downstream part of it. This observation was reported also in literature [68].

4.4.2 Effects of specific parameters

After the repetition of the above deposition process to assure the reproducibility of the result, many other experiments were performed aiming to an optimization and a better control on some growth parameters, such as thickness of the film and crystal size. The effort to obtain single crystalline structure was not achievable using this type of CVD set-up, but an analysis of the main parameter changes and their results proved the choice of the best variables for the growth of ZrS_2.

Temperature of the substrate

First of all, to allow a better diffusion of surface atoms and molecules, the temperature of the SiO_2/Si substrate was brought to 950 °C [32].

In this case, the sample appeared to be almost completely empty, having just some traces of contaminations and thick crystalline structures as the one reported in Figure 4.16. These clusters were made of ZrS_2, but just a few of them were present in the whole sample surface. The hypothesis for the worse result with respect to the previous ones could be pointed at the too high temperature of the substrate, which may have desorbed most of the particles impinging onto it.

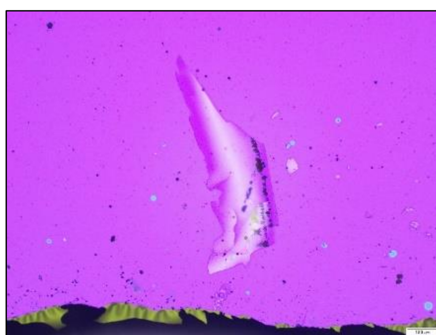

Figure 4.16: Cluster of ZrS_2.

Inert gas flux and substrate distance

In other experiments, we took down the inert flux, after the purging step, to values in the range of 50 sccm.

The distance between the substrate and the crucibles is another important parameter in this process. It has been demonstrated that shorter substrate-precursors distance favours large-size domains of few-layers with rough edges [69]. The use of 50 sccm of Ar flux was probably too low to effectively transport the precursors species, or their products of reaction, towards the substrate. Probably, the main difficulty have been the transport of Zr-compounds because $ZrCl_4$ was placed in the secondary furnace, thus it has to travel longer distances with respect to the W-precursor in the tungsten disulphide/diselenide syntheses.

Here, the distance between $ZrCl_4$ crucible and the silicon substrate was in the range of 25 cm. Accordingly, both the phenomena of low flux, together with a longer distance to travel, could have led to a limited presence of zirconium on the substrate and the consequent impossibility of growth of our material.

To assert the veracity of this statement, I carried out a synthesis placing a wafer substrate at the extreme downstream edge of the main furnace (half out of it): the result was a silicon wafer completely covered by different structures of sulphur, proved by the Raman spectroscopy (Figure 4.17). They formed due to the large change in temperature between the furnace and the room temperature which have led to the frosting of S vapours.

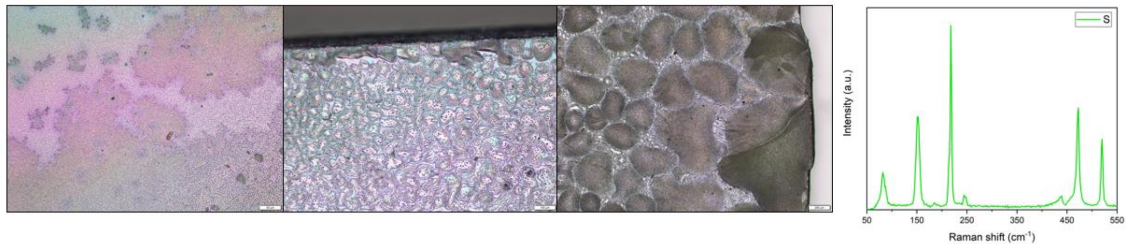

Figure 4.17: Optical images of S at different scale bars and relative Raman spectrum (confirmed by RRUFF database).

I did not perform any other changes on the inert gas flux because in general it is considered as a poorly influent parameter for the CVD deposition.

Precursors quantity

The quantity of precursors has been tuned accordingly to TMDs growths reported in the literature and performed in our laboratory. The precursors conversion efficiency and consumption is an important factor to estimate the cost factor of a production. For this reason I tried to find out which was the minimum quantity of $ZrCl_4$ required for the deposition of ZrS_2 film. An excess of sulphur chalcogen assured the presence of enough chalcogen during the process, while the metal precursor was traditionally used around values of tenths of a gram.

Reproducing the best synthesis at 220 °C, it resulted to be successful even using a value of 0.1 g instead of 0.3 g, leading to the deposition of the usual ZrS_2 thin films. Instead, decreasing further the precursor amount to half this value, 0.05 g, did not lead to any growth. Just sporadic sulphur structures, such as spherical crystallites, were present probably due to a scarce presence of Zr during the deposition process. The reaction is also very sensitive to small changes in precursors quantities in terms of spatial aggregation; if the $ZrCl_4$ powder is not completely spread over the crucible but it has some accumulations, in that zones a lower portion of powder is exposed to external environment, introducing limitations in the sublimation.

Growth time

After having achieved the most optimized synthesis methodology to produce ZrS_2 nanosheets, several variations in the time of deposition were performed. This experiments were executed in order to find the minimum time for the actual deposition of ZrS_2 and at the same time reveal variations in the thickness and morphologies of our film. The different times proposed were: 8, 10, 12, 15, 20 and 25 minutes; before 8 minutes no growth of our material was observed. Since the reproducibility in CVD is limited, more experiments should be made in order to confirm this statement. The use of the scanning electron microscope (SEM) allowed us to furtherly study the surface morphology of the film.

For information on the influence of the chamber pressure variations, I refer you to the Appendix (A1).

4.4.3 Different substrate orientations

The change in substrate orientation with respect to the flow of precursors has been mentioned in literature. To the best of our knowledge, one of these papers

was reported by *Wang et. al.*, who synthesised MoS_2 via CVD placing the substrate face down on the MoO_3-containing crucible. They discovered that, depending on the Mo:S ratio, different shapes of crystals appear.

I followed the same configuration for ZrS_2, placing a SiO_2/Si and a sapphire substrate upon two 0.01 g $ZrCl_4$-containing crucibles each (Figure 4.18).

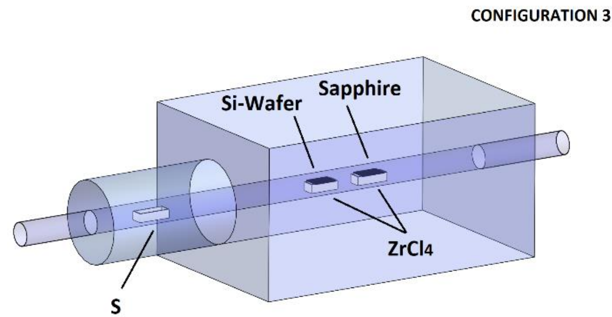

Figure 4.18: Upside-down configuration. The silicon and sapphire wafers are placed face-down upon two $ZrCl_4$-containg crucibles.

The substrates were both placed in the middle of the main furnace at a temperature of 350-400 °C, in order to promote the precursor sublimation and at the same time having decent diffusivity on the substrate.

The sulphur source was placed in the secondary furnace at 150 °C. After a growth time of 15 minutes, the main furnace was brought at a 700 °C, trying to favour rearrangement of grown structures.

The result was not successful probably due to the fact that during deposition the substrate was not warm enough to promote the adhesion and diffusion of the chemical species. Moreover, S atoms may have not been able to reach in sufficient quantity the facing-down substrate since the distance substrate-edge of crucible was less than 1 cm.

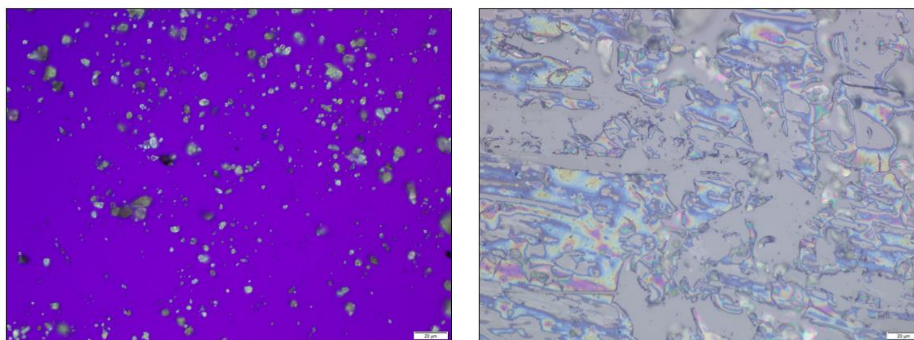

Figure 4.19: Micrographs of SiO_2/Si (left) and Al_2O_3 (right) substrates in the upside-down configuration are shown. Scale bars: 20 µm.

Optical micrographs of the process show that something has been deposited also on sapphire, but Raman spectroscopy gave no vibrational mode peaks, indicating absence of ZrS_2 (Figure 4.19).

As a matter of fact, also vertically positioned silicon substrates with respect to the gas flow were placed in the reaction tube in other experiments. The results were the same reported in Figure 4.19 on the left. Probably, changing the optimized parameters for the synthesis could have led to a slower evaporation rate of Zr-precursor leaving the majority of it unreacted.

4.4.4 Deposition on Au foil

The deposition on gold substrates was performed to see if growth of ZrS_2 may be possible. Furthermore, Au is a reusable substrate which can be applied for photocatalysis and photodetectors.

Gold foils of 25 µm of thickness were chosen as substrates for the growth of ZrS_2 crystals. A piece of 0.8 x 2.5 cm size was accommodated over a silicon substrate and fixed to it by folding a small edge around it in order to keep it stable when the inert flux and pump are activated (Figure 4.20).

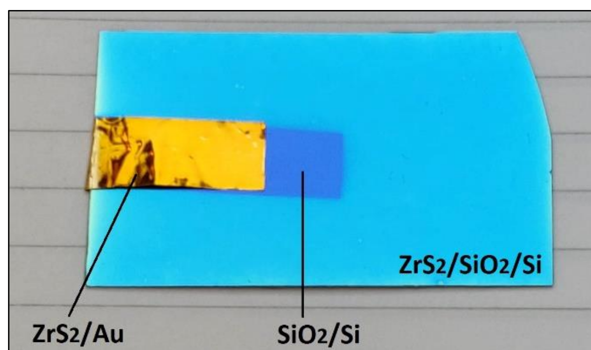

Figure 4.20: Photograph showing the Au foil over the SiO_2/Si sample. A piece of gold has been cut to show the deposition of ZrS_2 also on the silicon substrate.

Following the deposition process reported in Table 4, form the optical microscope appeared zones of partial deposition on gold which have been associate to ZrS_2 by the Raman spectroscopy.

Further studies by SEM revealed the presence of inhomogeneous growth of ZrS_2 having different thicknesses (Figure 4.21) and appearing as shades on the gold substrate.

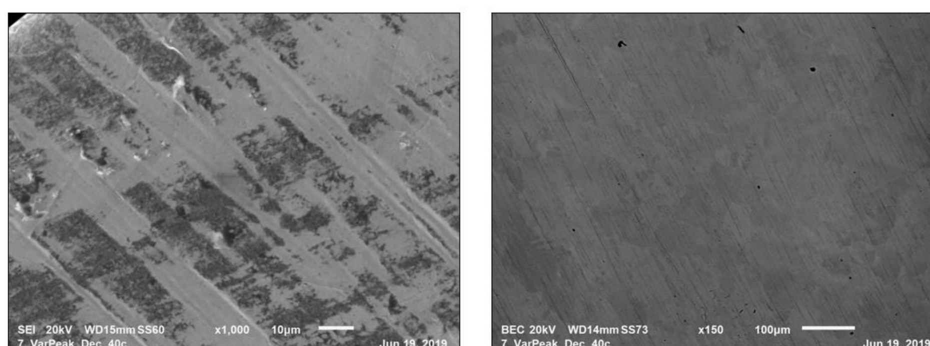

Figure 4.21: SEM images of ZrS_2 deposited on gold foils. Scale bars: 10 µm and 100 µm, respectively.

Finally, x-ray photoelectron spectroscopy analysis was used to study the superficial composition (~ 10 nm) of the samples. The results are shown in Figure 4.22. The peaks related to the Zr 3d orbital were associated to both ZrS_2 and ZrO_2. Furthermore, their relative intensities proved a strong oxidation of the surface in few days from the synthesis. A single state was associated to gold, while for O 1s we found contaminations probably by adsorbed molecules form the atmosphere. It wasn't possible to associate the sulphur 2p doublets with specific compounds,

but an hypothesis is that the doublet at higher energies comes from a compound-containing sulphate ion, while the other probably to hydroxide species of sulphur.

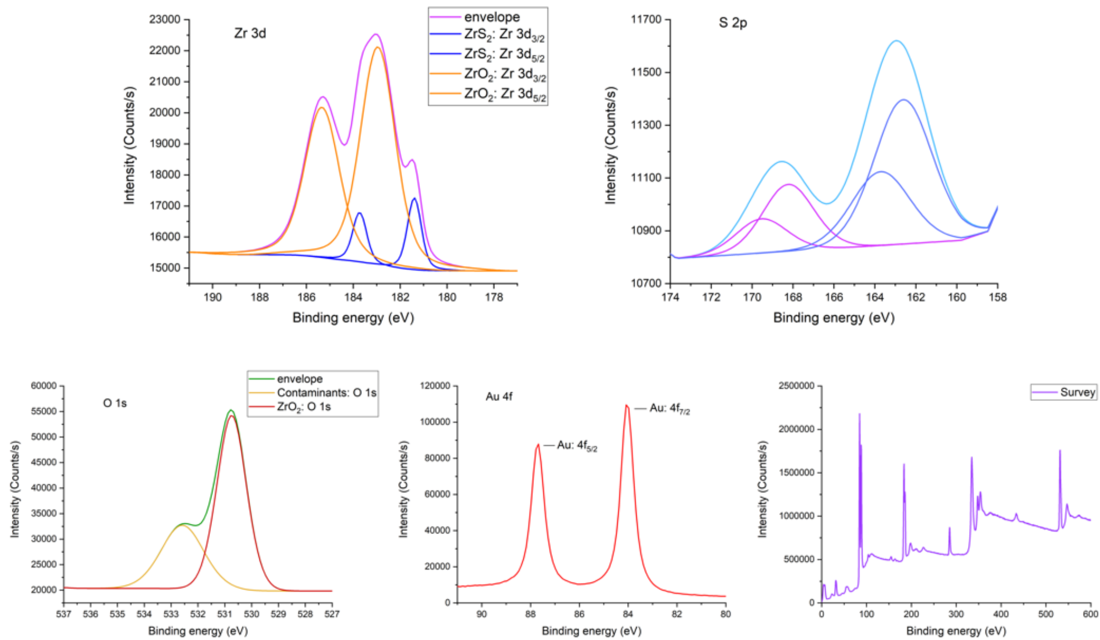

Figure 4.22: XPS spectra of ZrS_2 on gold.

4.4.5 Deposition on sapphire

Further the upside-down deposition reported in Chapter 4.4.3., following the same paramenters and CVD configuration in Table 4, Al_2O_3 was again used as the substrate. The fact that the sapphire wafer is a single crystal having (0001) planes orinetation and similar lattice paramenters of ZrS_2, could have led to a preferential epitaxyal growth of ZrS_2 crystals.

The results included only strucures having asymmethrycal and flower-like morphologies (Figure 4.23). The Raman spectroscopy labelled them as sulphur structures, while non ZrS_2 was found. Only few samples were synthesised, so

additional experiments and deepening should be carried out on sapphire substrates.

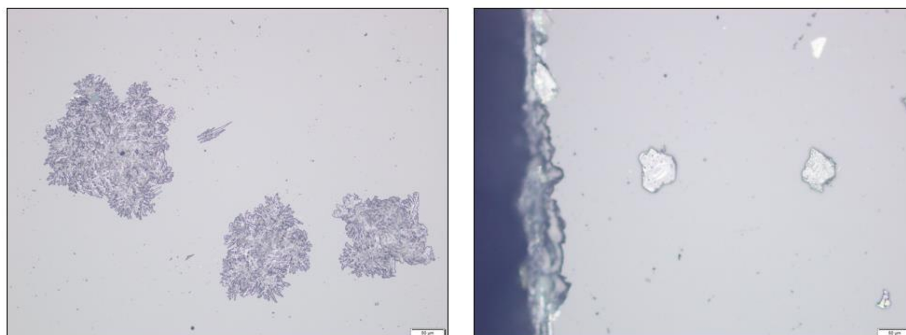

Figure 4.23: Sulphur structures on sapphire.

4.4.6 Choice of different precursors

Another common synthesis approach is the sulphurisation of metallic oxides (WO_3, MoO_3, etc.). As an alternative reaction pathway we used ZrO_2 mixed with NaCl to grow ZrS_2. Zirconium dioxide has a really low volatility but, as already mentioned, the addition of alkali metal halides should be able to create volatile metal-oxyhalide compounds which can reduce the overall reaction temperature. Following *Zhou et. al.*, which reported to have obtained ZrS_2 from a powder mixture with ratio of 3:1 between ZrO_2 and NaCl respectively [60], I performed a similar procedure with the only difference being the use of Ar flux and not Ar/H_2. A 0.3 g mixture was introduced into the main furnace at a T = 800, 820 and 850 °C in three different experiments, always with 2 g of sulphur powder in the other furnace at T = 130 °C. The results are shown in Figure 4.24; something was deposited, but the material wasn't ZrS_2. Some of the Raman spectra led to sulphur structures again.

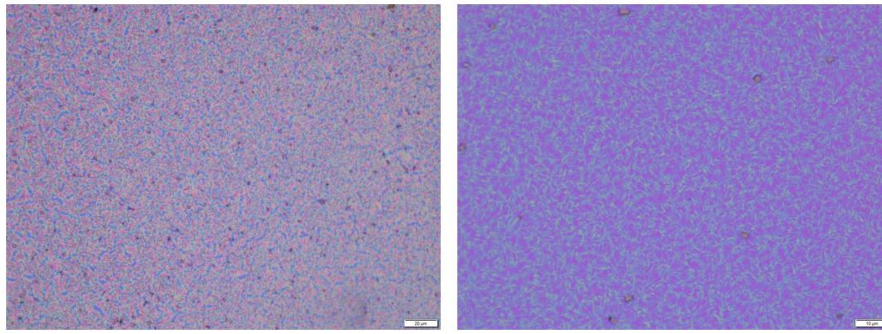

Figure 4.24: Structures from the deposition of ZrO_2 + NaCl and S as precursors. Scale bars: 20 and 10 µm, respectively.

Hence, the literature results were not reproducible by our CVD set-up.

4.4.7 Physical and morphological characterisation of ZrS_2 on SiO_2/Si

We analysed the completely covered substrates with the aim to achieve as many information as possible about compositional, crystalline, morphological and optical characteristics and properties. Personally, I performed the Raman measurements and the photoluminescence ones. In this chapter I will analyse the results obtained for ZrS_2 on SiO_2/Si substrates, focusing on the specific properties we would like to investigate.

To explore the materials obtained from the syntheses, as a first discriminating technique, I performed Raman spectroscopy.

In doing so, particular attention must be paid to the laser power and exposure time used, since too high values could lead to the destruction of a thin flake and thus, to the degradation of our thin film. For this reason, I usually carried out the measurements using form 0.1% to 1% of the laser beam power, which was of 50 mW, hence a power from 50 to 500 µW/µm^2 was used. The accumulations were usually from 1 to 10 in order to have a better signal to noise ratio, while the exposure time was usually a few seconds. The Raman spectra obtained for each

polycrystalline sample are representative of ZrS_2 material and find support in literature; in Figure 4.25 a comparison between an extended experimental spectrum and another one from literature shows the same features all over the spectral range.

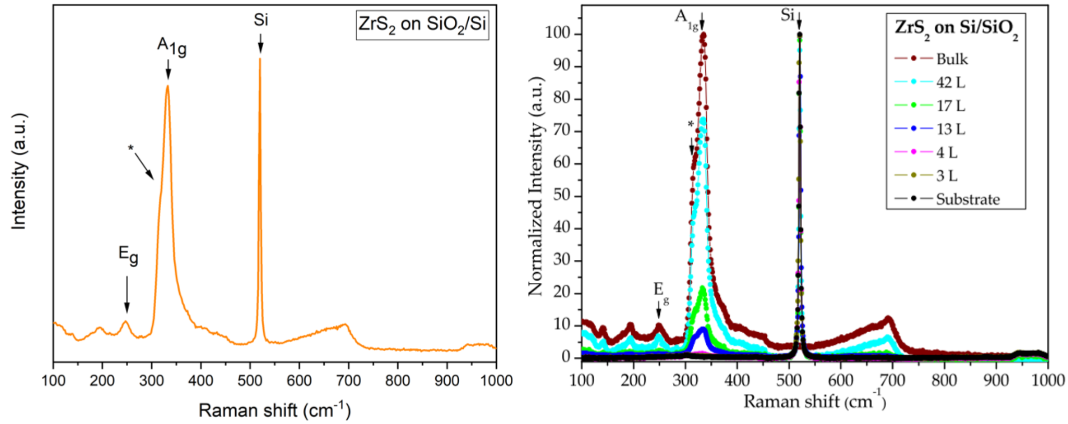

Figure 4.25: Left: Experimental spectrum of ZrS_2 thin film grown by CVD. Right: Raman spectra for different number of layers obtained by mechanical exfoliation [36].

The silicon peak appears at 520 cm^{-1}, while the two characteristic Raman peaks are at 250 cm^{-1} (E_g) and at 334 cm^{-1} (A_{1g}). Regarding the "*" broadening of peak A_{1g}, the reason can be attributed to anharmonicity [36].

A fitting of the characteristic A_{1g} peak and its shoulder (denoted as "X") is shown in Figure 4.26; from the experimental Raman data (dotted line) it has been possible to deconvolute the peak into two curves, one related to the A_{1g} peak, the other associated to the "*" broadening caused by anharmonic effects.

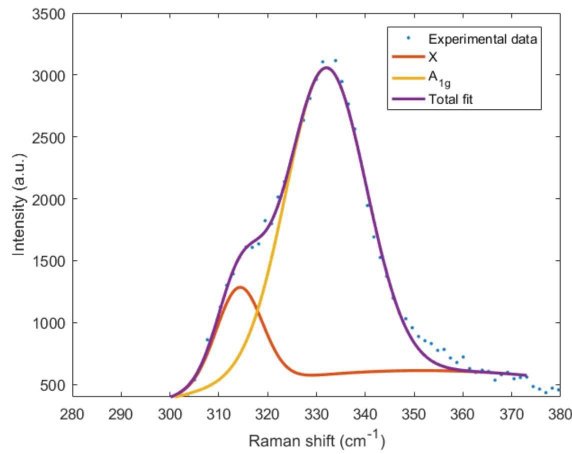

Figure 4.26: Deconvolution and fitting of the experimental main peak for ZrS_2 (blue dotted line). The yellow curve refers to the A_{1g} peak, the red curve to the "" broadening of A_{1g}, while the violet curve resembles the total fitting.*

Inhomogeneity in the polycrystalline samples are well visible in Figure 4.27 (left), reporting an optical micrograph where we can see at least three areas of different thickness going from the external edge to few hundreds of μm inward. Three circle of different colours have been drawn on the picture which are related to the three different Raman spectra on the right; going from the edge to the inner part the thickness decreases till a point (blue one) where it stabilizes and remains constant through all the rest of the substrate.

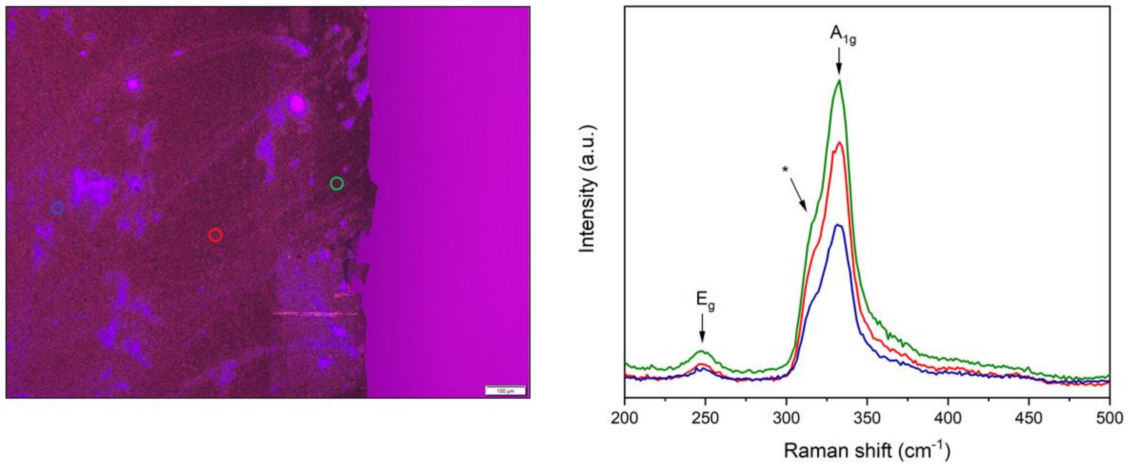

Figure 4.27: Left: Optical micrograph of a ZrS_2 sample grown for 25 min. Scale bar: 100 μm. Right: Raman spectra of the three circled points in the left image.

Furthermore, to qualitatively visualize the difference in thickness and crystalline quality present in our samples, several Raman maps and their related histograms have been designed, referring to the A_{1g} peak. This has been possible only by deconvoluting the previously shown peak in Figure 4.26. Thanks to this, the analysis of the Raman maps of both the intensity and the width are referred to the A_{1g} peak only. We chose A_{1g} peak because it was the most intense in the Raman spectrum and, as we have mentioned, it remains visible till very few number of layers.

The Raman maps have been performed with the same machine used for the collection of the Raman spectra. A Raman map consist in the subsequent measurement of Raman spectra related to adjacent points in a selected area. It is possible to choose a "step" between the acquisition of two Raman spectra, usually lower than 1 µm. A sliding sample-holder made possible the recording of each Raman spectrum. In the end, we obtain information about the position, the intensity and the width of every peak in the spectrum.

The intensity maps colour-bar has a value between zero (dark blue) to the maximum value (light yellow) found in the sample. This is well visible in Figure 4.28, where an intensity map was taken in an area between the bare silicon substrate and the polycrystalline ZrS_2. In this area, ZrS_2 is not present homogeneously, giving raise to regions where it's present and others where it's not. From the magnification of the blue squared area, we can see that ZrS_2 firstly grows in the islands form and later it converges to create a film.

As a matter of fact, the change in colour is referring to a different thickness of our sample, higher when it tends to yellow.

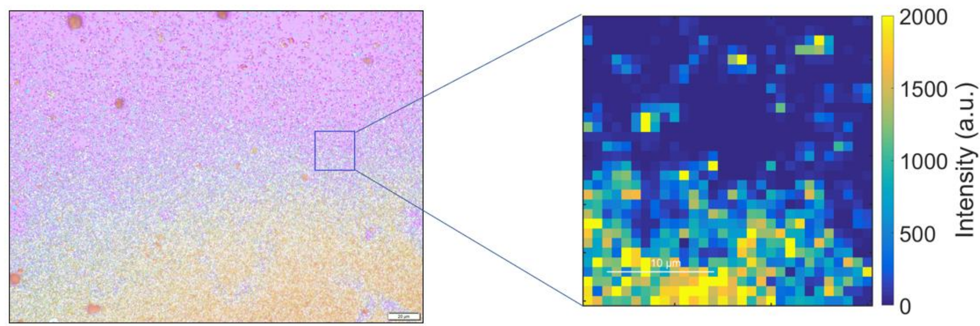

Figure 4.28: Raman map of the intensity of the A_{1g} peak (on the right) referring to the blue squared area from the optical micrograph on the left.

Moreover, we report the A_{1g} peak intensity variation of an area of ~225 µm² of complete covering of the substrate, measured on a sample grown for 15 minutes. Consecutive Raman spectra were taken with a step of 0.3 µm from one to the other with and exposition time of 1 s per measurement. Taking into account Figure 4.29, we can see that the intensity map appears quite homogeneous except for some very intense randomly positioned peaks. Anyway, the vast majority of the peak intensities remains below half the value of these maximum peaks, as we can see form the probability histogram (Figure 4.29 right).

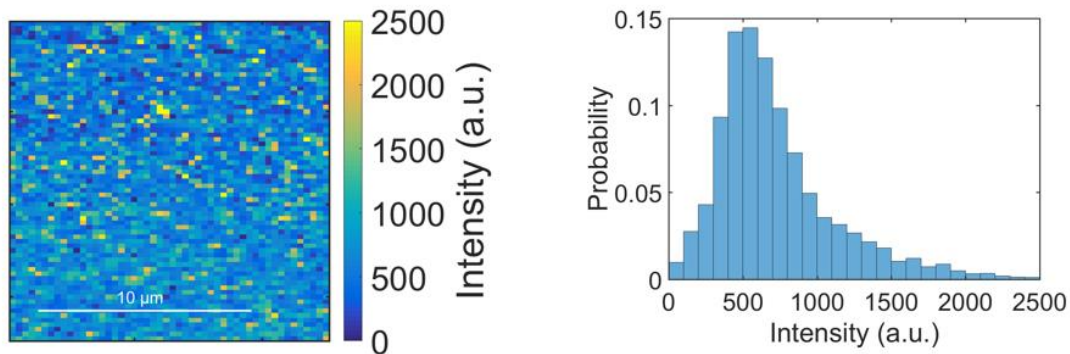

Figure 4.29: Raman map and related histogram of the intensity of A_{1g} peak.

Instead, focusing on the FWHM of the A_{1g} peak, we observed a curve in the narrow range between 16 and 18 cm^{-1} (Figure 4.30 right).

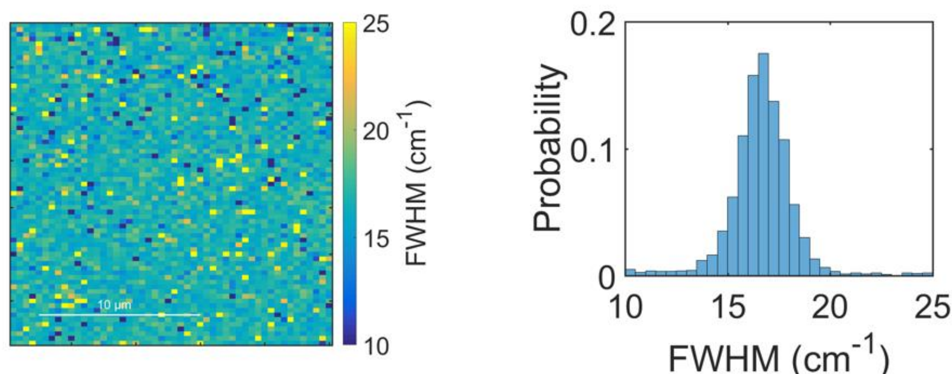

Figure 4.30: Raman map and histogram referring to the FWHM of the A_{1g} peak of a sample grown for 15 minutes. The histogram has been normalized to 1.

This narrow distribution of FWHM is an indication of the homogeneity of our sample.

A further investigation, focusing on the atomic composition and chemical state of our samples, was x-ray photoelectron spectroscopy (Figure 4.31).

From the survey we observe the presence of Si 2p at ~ 100 eV and Si 2s at ~ 150 eV; this made us assign the O 1s peaks for SiO_2 and ZrO_2 located at 532.2 eV and 530.4 eV, respectively. Considering sulphur, no database was found regarding S 2p of ZrS_2. But checking other spectral lines of sulphur in the same range of binding energies, they all correspond to transition metal-sulphides; thus we can infer that our 161.7 eV and 160.6 eV peaks correspond to S $2p_{1/2}$ and S $2p_{3/2}$ of ZrS_2, respectively. Due to the fact that our sample has been exposed to air, in the XPS spectrum we find the presence of ZrO_2. This indicates that ZrS_2 is subjected to surface oxidation during aging.

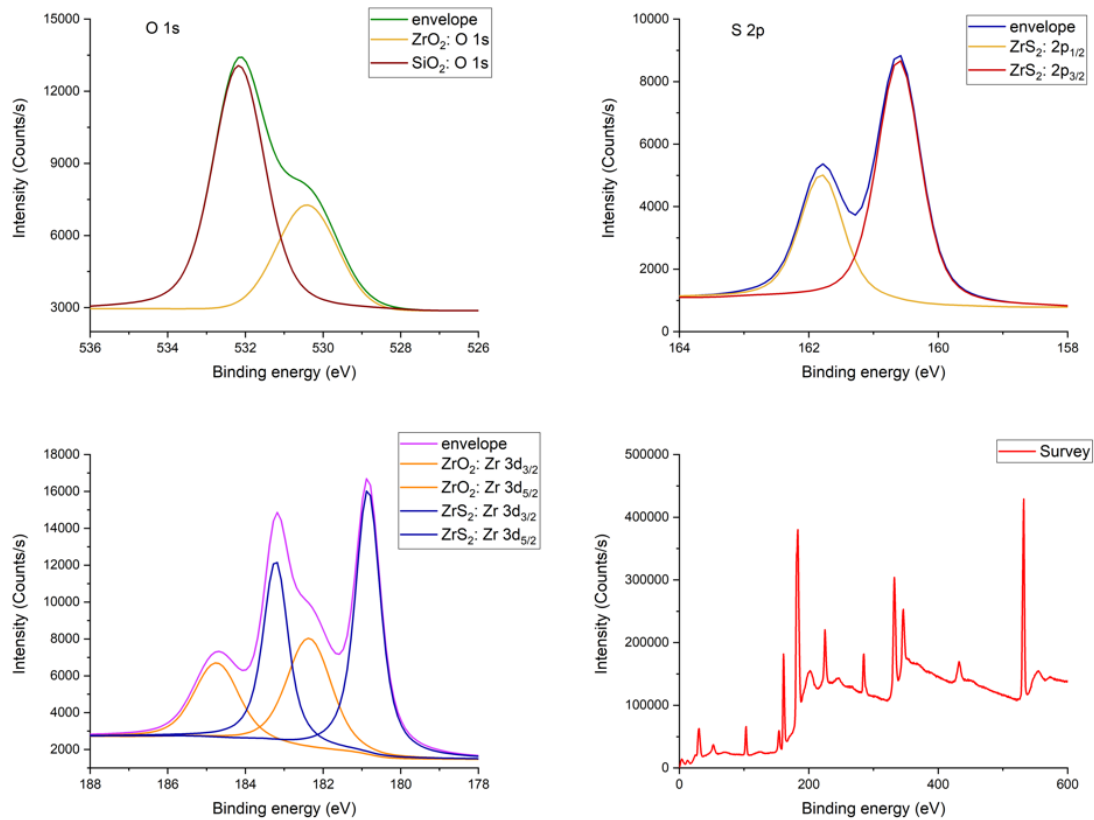

Figure 4.31: XPS spectra of polycrystalline ZrS_2 sample grown for 12 minutes.

As we can see from the Zr spectrum above, the difference in energy between Zr-oxide and ZrS_2 is very small. The Zr $3d_{3/2}$ and Zr $3d_{5/2}$ peaks for ZrO_2 are positioned at 184.8 eV and 182.4 eV respectively, while for ZrS_2, Zr $3d_{3/2}$ peak is at 183.2 eV and Zr $3d_{5/2}$ peak is at 180.9 eV. The peaks relative to the oxides of an element or compound are at slightly higher binding energies with respect to the pure material, for electronegativity reasons. In our case, this happens because the oxygen is more electronegative than sulphur and we know, as a rule of thumb, that the binding energy increases proportionally to the electronegativity of the elements bonded to the metal. The intensity of the non-oxidized peaks is higher than the oxidized ones, and this is a clear indication of the majority of ZrS_2 unoxidized.

Thanks to the use of the TEM, it was possible to perform an elemental analysis of small areas of the exfoliated flakes by the energy-dispersive x-ray spectroscopy.

It provided a spectrum of the x-ray energies corresponding to the characteristic difference in energy between the two shells (involved in the excitation), thus univocally leading to the atomic structure of a specific emitting element.

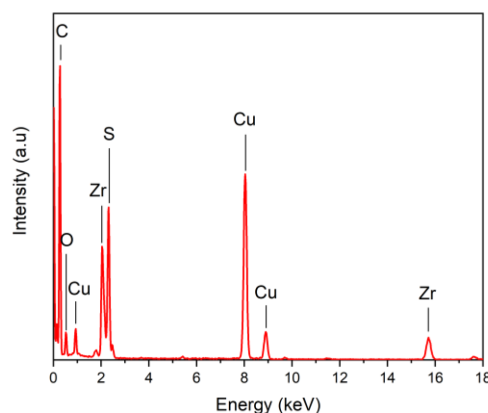

Figure 4.32: EDS spectrum of an exfoliated flake of ZrS_2.

Figure 4.32 summarises the main elements present in ZrS_2 flakes: we can state that no extra-elements contamination has been revealed by this measurement, a part from a small quantity of oxygen, probably coming from a natural surface oxidation through time. The presence of copper has to be assigned to the carbon coated copper grids used to carry out the measurement, while carbon is also a common contaminant coming from the environment. Furthermore, the stoichiometric ratio of the analysed flakes appears to be near the 2:1 (S:Zr) with a slight excess of Zr atoms, in the ratio from 1.60 to 1.70 at. %.

The main purpose of x-ray diffraction data analysis is to assess the crystalline nature and to provide specific crystalline orientation for our material, ZrS_2. Furthermore, it can help giving a comprehensive overview with respect to the data acquired with other investigations and can contribute to an overall model for the deposited sample. Crystalline planes, which undergo x-ray diffraction for specific values of the incident radiation angle, create sharp peaks in the spectrum. XRD analysis starts from considering all the elements present in the sample and linking them to specific compound and compounds-phases, which can be find in

the database, to interpret the peaks we got from the XRD spectrum. The characteristic peaks, which are found in the database, are based on powder diffraction data referring to crystal powders randomly orientated. This means that, from the reference data found in the database for our material, only the position of the planes must be taken into account, not their absolute intensities.

From the graph obtained (Figure 4.33), we can see the presence of a very intense peak at $2\theta \cong 15.3°$ and then other small peaks at higher angles, equal to $2\theta \cong 30.7°, 33.0°, 46.8°, 61.8°, 63.9°$. A blank sample of silicon substrate showed that the peaks at $2\theta = 33.0°$ and $61.8°$ are relative to the substrate.

Instead, the other four peaks are related to our sample and specifically refers to:

- $2\theta = 15.3° \rightarrow (001)\ plane$
- $2\theta = 30.7° \rightarrow (002)\ plane$
- $2\theta = 46.8° \rightarrow (003)\ plane$
- $2\theta = 63.9° \rightarrow (004)\ plane$

This is a very interesting result from the point of view of the growth; these families of Miller indexes refer to planes that are parallel to the surface of the substrate in a perfectly aligned manner. This means that the crystallites composing our material are position all with the same orientation and always parallel to the substrate.

From this result, we can now infer an islands growth mode which then leads to their merging and consequent formation of the polycrystalline film structure of ZrS_2, as already thought from the Raman maps.

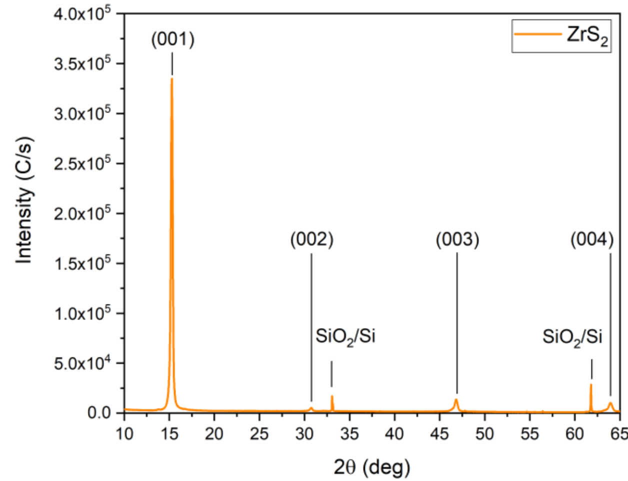

Figure 4.33: XRD spectrum of a polycrystalline ZrS_2 thin film.

Another technique, used to study the atomic structure of our ZrS_2 samples, was the high-resolution transmission electron microscopy. In this work, HR-TEM has been used to visualize the crystal structure of CVD-grown ZrS_2 films and to determine the lattice parameters. We were able to observe the atoms one by one and spot their relative positions and arrangement. In order to prepare the sample for the analysis, I performed an exfolaition process of the polycrystalline layers. After placing a small sample of 1 x 1 cm^2 in a vial, containing an appropriate amount of ethanol, I let it in a ultrasonication water bath for 15 minutes. The result was a suspension of flakes, which we can detect by a change in colour and refractive index of light from the previous transparent ethanol. The suspended traces of ZrS_2 detatched from the silicon substrate are with high probablilty flakes coming from the surface.

Once ZrS_2 particles are well dispersed in ethanol, few droplets of the solution are drop casted onto a TEM grid, used to observe a clear image in its holes where electons can pass through. After waiting few minutes for the evaporation of ethanol, the sample was ready to be investigated.

From the collected images, we observed several flakes of different shapes and dimensions: a perfect triangular flake, probably a monolayer of ZrS_2, a few-

layered flake and a thicker one are reported in Figure 4.34. The latter seems to be made of vertical flakes still attached to the layered ZrS_2 underneath, a futher proof that we have a ZrS_2 film over silicon.

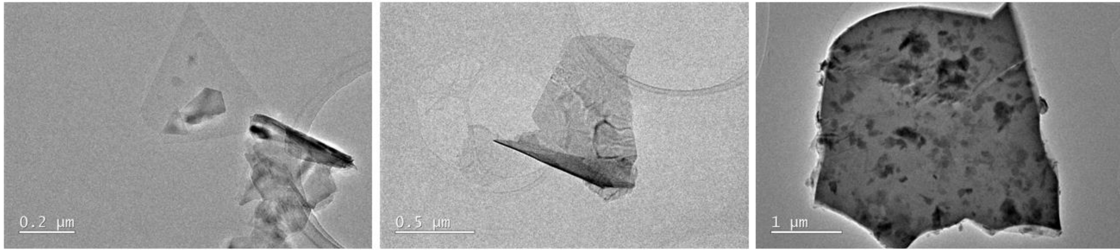

Figure 4.34: TEM images of different flakes taken at different magnitudes. Left: Perfect triangular flake; scale bar 0.2 µm. Middle: Few-layered flake; scale bar 0.5 µm. Right: Thick sample; scale bar 1 µm.

Going to higher magnituedes inside these flakes, it was possible to spot the atomic structure (Figure 4.35). The flakes are composed of crystalline and amorphous domains, the latter being mainly on at the edges. In the crystalline parts we can see a prefect atomic array of atoms resembling an hexagonal lattice. No point defects or voids are observed over large areas.

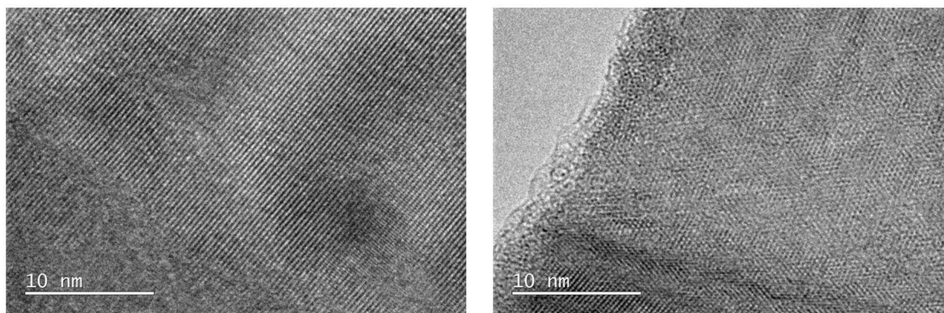

Figure 4.35: HR-TEM images of the flakes. Crystalline and amorphous domains are visible. Scale bar: 10 nm.

This can be better visualised by the selected area electron diffraction technique, which can be performed by the same TEM machine. From an SAED measurement done on the previously mentioned triangular flake (top part), we obtained the diffraction pattern in the reciprocal space (Figure 4.36). It resembles the hexagonal pattern of the crystal lattice in the reciprocal space, highlighting high crystallinity.

Furthermore, singles spots appear only when the beam is diffracted by a single crystal. The points of an hexagon refer to a family of planes; these have all the same interplanar distances but different orientations. The vector going from the centre of the SAED to a bright spot is thus perpendicular to that family of planes. Hence, each normal vector is proportional, in modulus, to the reciprocal of an interplanar distance in the real lattice. Thus, measuring the distance in the diffraction pattern, we can calculate the distance between the corresponding planes in the direct space. This is possible through a software in the machine, which calculates the reciprocal of the value obtained and multiplies it for a constant related to the machine itself.

The measured interplanar distances are: 3.13 Å for the (100) planes and 1.82 Å for the (110) planes. These values are very close to bulk ones: 3.16 Å and 1.83 Å respectively (form ICDD Database).

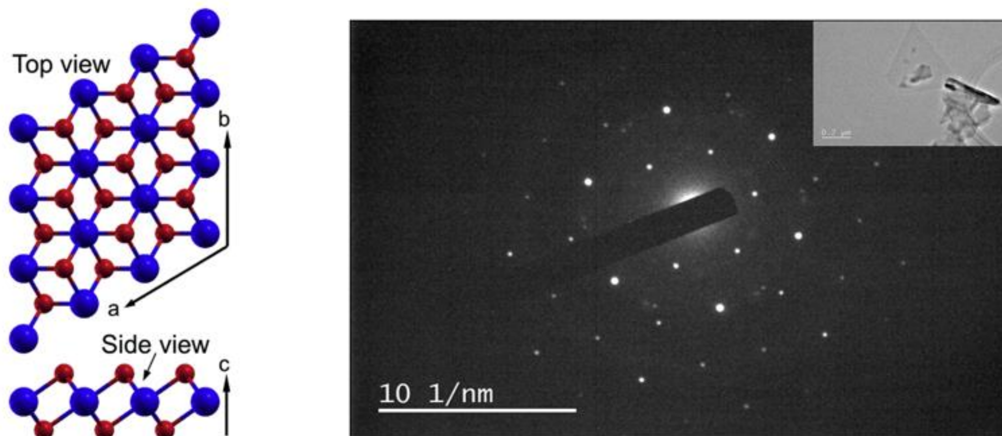

Figure 4.36: Left: Top and side views of monolayer ZrS_2 showing the hexagonal lattice; a, b and c axes are defined [70]. *Right: SAED image of the triangular flake in the inset. A perfect hexagonal lattice is visible.*

<u>Field emission scanning electron microscopy</u> has been employed to probe the morphology of the ZrS_2 films. Thus, lateral size, distribution and density of ZrS_2 vertical flakes have been characterized. Figure 4.37 shows a sample holder carrying eight different ZrS_2 samples both on silicon and gold.

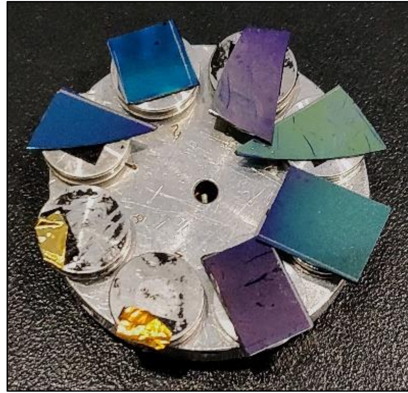

Figure 4.37: SEM samples-holder carrying ZrS_2 on both SiO_2/Si and gold substrates.

The surface of the sample appears to be covered by vertical flakes of ZrS_2. We can say that at the bottom of these flakes there is ZrS_2 grown layer-by-layer, as prooved by Raman spectroscopy and XRD measurement.

As reported in other papers [31], the size of these vertical flakes is related to the time of growth given to the sample. To the best of our knowledge, we report for the first time the synthesis of vertical flakes of ZrS_2 on silicon and gold substrates. As we can see from the SEM images in Figure 4.38, we repoted images taken at the same magnitude for samples grown at t=10 min, t=15 min and t=25 min, respectively.

The size of the flakes is visibly increasing by increasing the growth time, doubling from 10 to 25 minutes. Using ImageJ software, we have estimated the maximum lateral sizes of the flakes visible form the SEM images and the results were:

- t = 10 minutes: ~ 400-550 nm
- t = 15 minutes: ~ 600-850 nm
- t = 25 minutes: ~ 1.3-1.5 µm

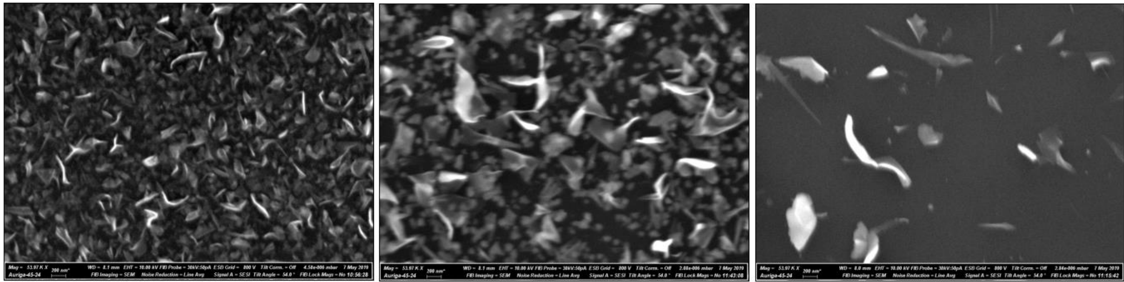

Figure 4.38: SEM images of ZrS_2 samples grown on SiO_2/Si at different times: 10, 15 and 25 minutes. Scale bars: 300 nm; magnitude 53.97 k.

Furthermore, looking at lower magnitudes the overall samples' surfaces, we have noticed that increasing the time of growth also increases the nucleation density while after a certain threshold, of ~ 15-20 minutes, the density decreases and we see bigger flakes (Figure 4.39). The first fact is in accordance with the theory of growth, which links the nucleation rate to the growth time. The second comment can be associate to a probable Ostwald-Ripening effect, which takes place through a coalescence process of flakes, leading to their enlargement and subsequent reduction of nucleation density. However, it has been observed for just few samples and in some cases even after the 20 minutes threshold, the nucleation density doesn't decrease. Ulterior investigations should be made to verify the veracity of this behaviour.

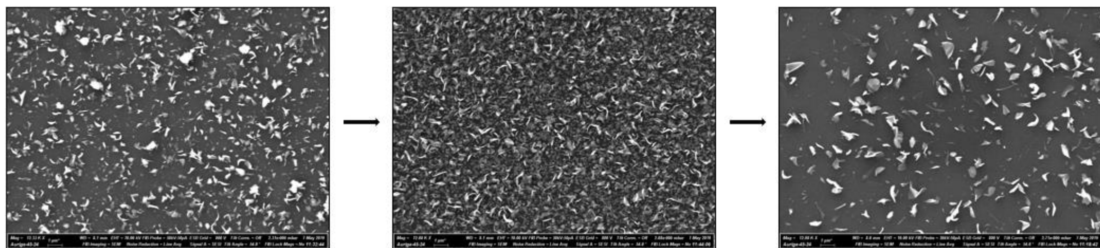

Figure 4.39: SEM images of ZrS_2 samples grown for 12, 15 and 25 minutes. Scale bars: 1 µm; magnitude 12 k.

A picture of the sample taken from a different perspective gave us the possibility to access, qualitatively, the thicknesses of the vertical flakes and the layered part (Figure 4.40). Because the scale bar is 300 nm, the silicon and silicon oxide parts

are well distinguishable. Above the SiO_2, we detect a layer certainly < 150 nm in thickness, followed by the inhomogeneous height of the vertical flakes. From the image, we can spot a flake (top left) of almost 1 μm.

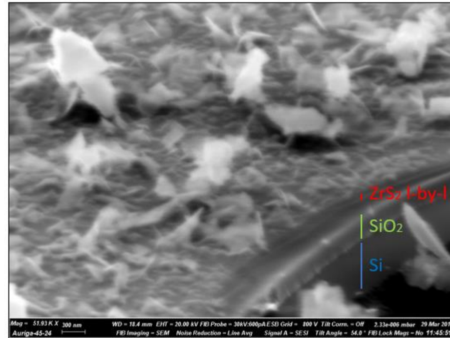

Figure 4.40: SEM image from a non-perpendicular direction. Scale bar: 300 nm; magnitude 53.97 k.

Other measurements by cross-sectional SEM were performed in order to quantify the height of the vertical flakes. The tallest one spotted is visible in the left image of Figure 4.41; it rises till a height of almost 10 μm. From all the other pictures, the average height seems to be in the range from 3 to 4 μm.

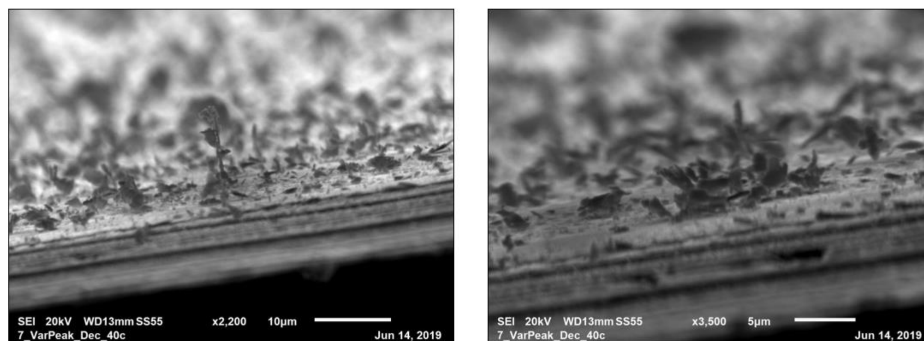

Figure 4.41: Cross-sectional SEM images portraying vertical flakes. Scale bars: 10 μm and 5 μm, respectively.

Moreover, a part from vertical flakes, sporadic different features were present on the surface and they are reported in Figure 4.42. Clusters of ZrS_2 covering the surface and having a layered structure could possibly be formed in the vapour phase and then condensed onto the surface, but another hypothesis is that they might be a remembrance of the bottom layered structure. Besides, preferentially

in long time growths, agglomerates of flakes were found in the bally form, reaching dimensions of more than 3 µm.

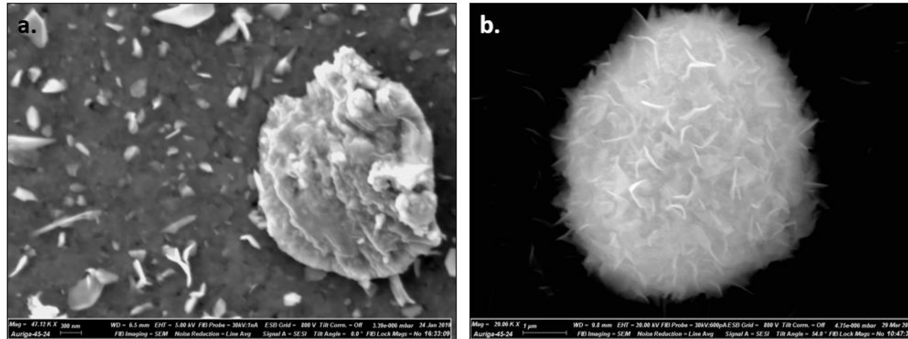

Figure 4.42: a. SEM image of a ZrS_2 cluster with terraced structure; b. ZrS_2 flakes ball with high contrast. Scale bars: 300 nm and 1 µm, respectively.

To assess the actual presence of both zirconium and sulphur in the whole sample surface, in order to surely associate the vertical flakes with ZrS_2, an EDS mapping has been performed on a small area. Signals of zirconium, sulphur, silicon and oxygen are visible all over the selected area in a homogeneous way (Figure 4.43). Just on the middle left we see a higher presence of S and Zr, probably due to a denser cluster or aggregate.

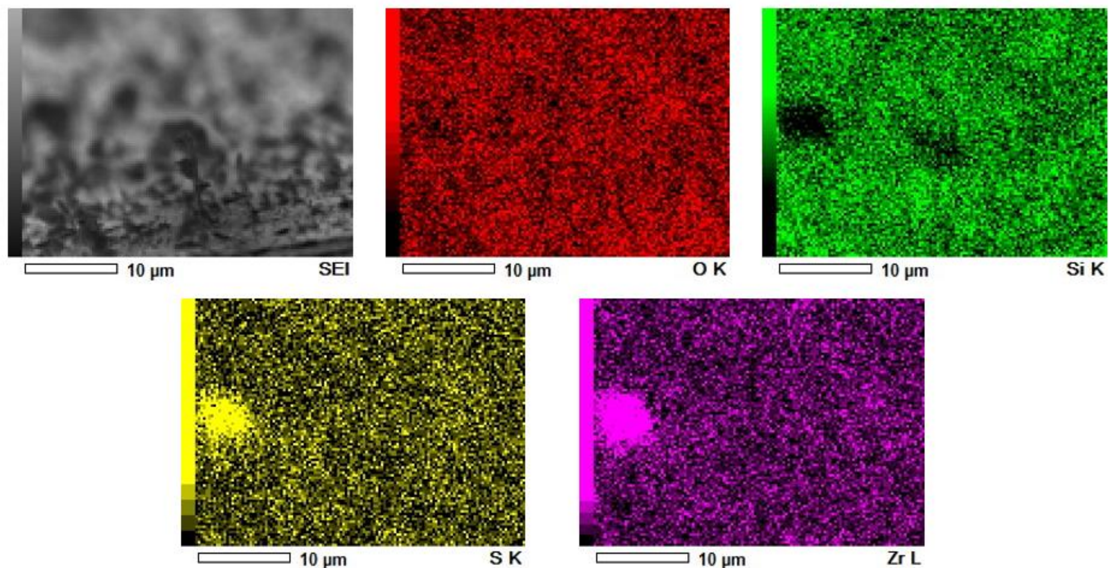

Figure 4.43: Top left: Area selected for the EDS map. Maps of oxygen, silicon, sulphur and zirconium are shown.

Furthermore, a variation in the colour of the covered silicon substrates indicates a different quantity of material on them (Figure 4.44).

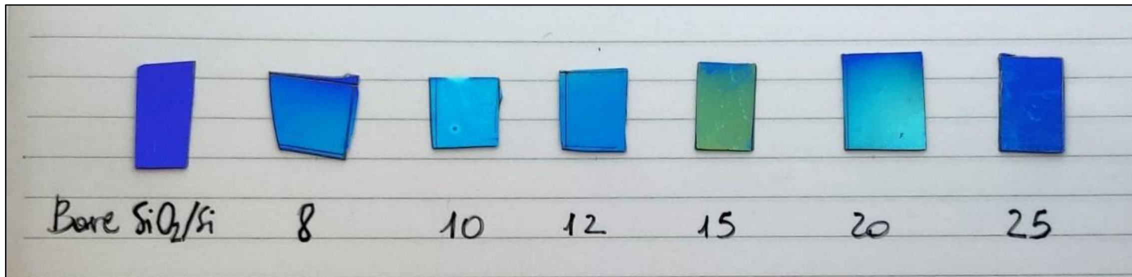

Figure 4.44: Photograph of ZrS_2 samples grown with increasing growth time as indicated in the picture (in minutes). Bare silicon substrate is reported at the extreme left.

To study the intrinsic optical properties of this innovative TMD, both photoluminescence and absorption spectroscopy have been carried out.

Photoluminescence analysis is carried out with the Raman spectroscopy equipment. In this configuration, photoluminescence is excited with a monochromatic source (532 nm) to measure the intensity of the PL emission over a range of wavelengths; in our case it goes form 1.2 eV to 1.6 eV.

The band gap related to ZrS_2 is indirect both in 3D and 2D form; in the monolayer form the optical gap has a value comprised between 1.14 and 1.7 [71]. Here we report a photoluminescence peak at **1.38 eV**, consistent with the nature of ZrS_2 reported in the literature ([36] [24] [72]), from a thick sample of ZrS_2. It refers to the bulk indirect band gap and it is completely separated from the silicon emission peak at 1.23 eV. This emission lies in the NIR region (898.43 nm).

In Figure 4.45 we can see the experimental data (dotted green line) which have been fitted with a gaussian curve (orange line). The FWHM calculated form the fitting is 140 meV.

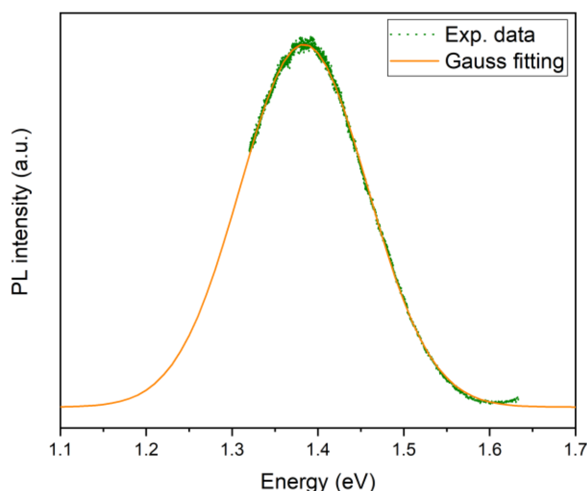

Figure 4.45: PL emission spectrum of ZrS_2 thick layer. The experimental data (dotted line) have been fitted with a gaussian curve (line).

Absorption spectroscopy was performed on a solution of ZrS_2 flakes dispersed in ethanol after sonication of a small sample.

The experimental absorption spectrum (Figure 4.46) provides the first evidence of strong excitonic effects in this material, thus prooving its semiconducting character. Here, I reported the absorbance spectrum going from 250 nm to 950 nm because at shorter wavelenghts the cuvette was absorbing, while after ~ 950 nm ethanol starts to absorb in the IR and so the measurment is no longer relevant.

From Figure 4.46 we can see two merging peaks with maximum values at 421 nm (2.94 eV) and 479 nm (2.58 eV). After the 479 nm peak, the absorbance of the film decrases gradually with increase in wavelength. The peak at higher wavelenghts can be associated with a probable transition at the band gap related to our material. The other peak can be associated to a transition of higher order.

Since the dispersion we made is probably polydisperse, thus the size and thickness of our flakes can vary in it (as we can see from the TEM images), the absorption spectrum we have is the result of that particular band structure

emerging from that dispersione of flakes. It is thus correlated to an intermedied situation between a monolayer and a bulk ZrS_2.

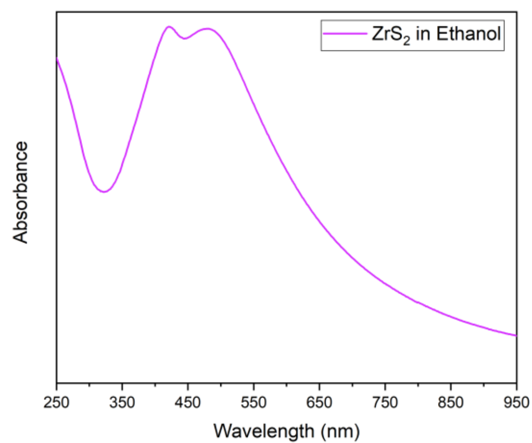

Figure 4.46: Absorption spectrum of ZrS_2 flakes in ethanol.

4.5 ZrS_xSe_{1-x} alloys

4.5.1 Synthesis and characterisation

At the end, after the successful synthesis of ZrS_2 films on SiO_2/Si substrates, the idea was to try an annealing process on the polycrystalline ZrS_2 samples with the addition of Se powder in order to form a ZrS_xSe_{2-x} alloy.

Just few syntheses were carried out with the following methodology: 0.3 grams of Se powder were placed in the secondary furnace at 340 °C, while the already synthesised ZrS_2 sample was placed in the main furnace and heated to a temperature of 700 and 720 °C. The time of deposition was fixed at 13-15 minutes.

After this process, Raman spectroscopy was performed on the final samples and the result shows different peaks from the ones of ZrS_2 spectra, indicating that something must have deposited on it (Figure 4.47).

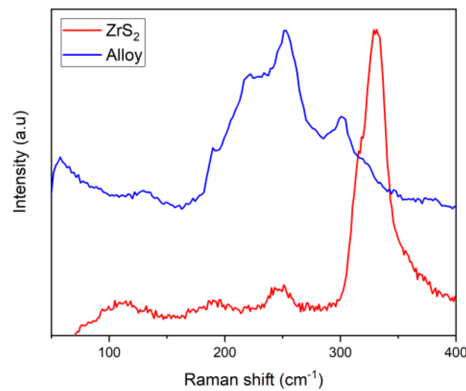

Figure 4.47: Comparison between Raman features of ZrS_2 (red) and ZrS_xSe_{2-x} (blue).

This was further checked thanks to XPS measurements (Figure 4.48), which revealed the presence of Se, S and Zr on the surface. The usual O 1s peaks for SiO_2 and ZrO_2 are located at 532.2 eV and 530.4 eV, respectively. In this sample, Zr 3d orbitals reveal the presence of ZrO_2 alone, not ZrS_2, probably because of heavy oxidation on the surface even before the alloying process. Electrons of

selenium 3d are coming from three different compounds, which, also in this case, was impossible to identify with precision. The doublet at higher binding energies can be associated to some selenium oxides while the other two doublets probably to some Se-containing hydroxides compounds.

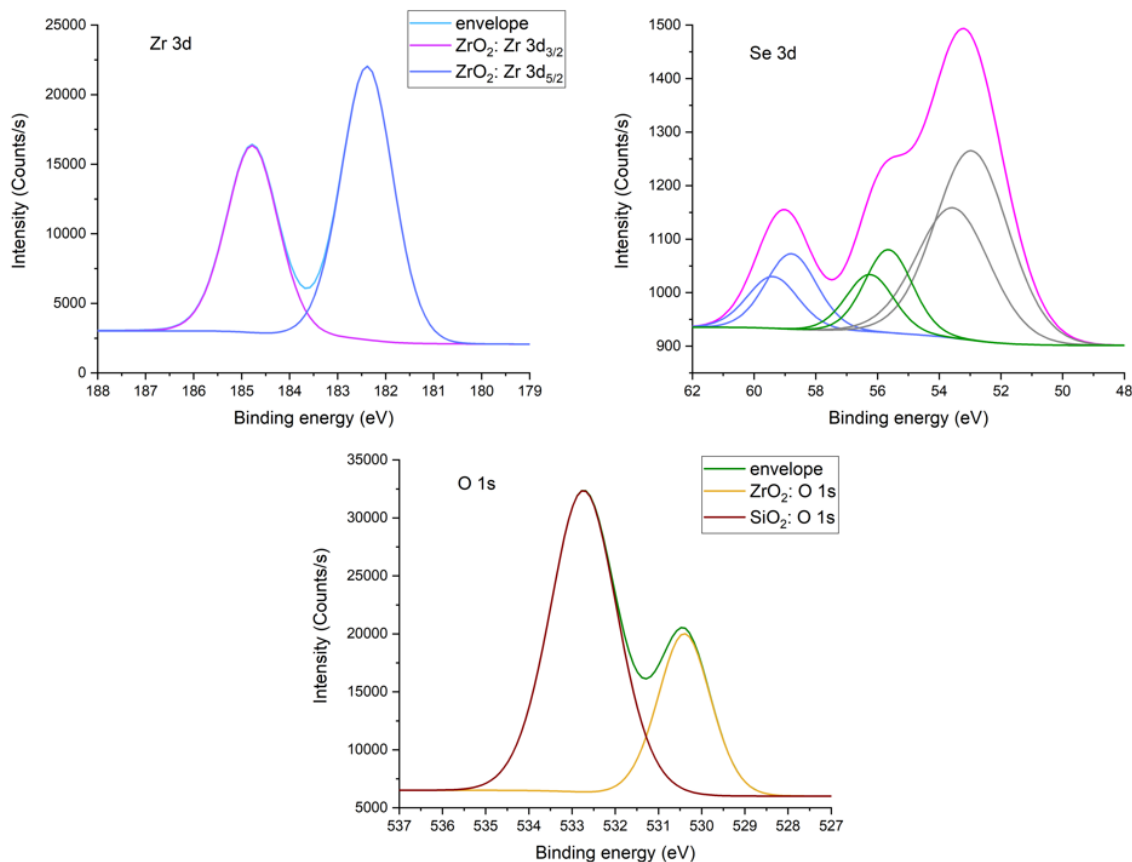

Figure 4.48: XPS spectra for ZrS_xSe_{2-x} alloy.

Furthermore, XRD measurements have been performed, obtaining some diffraction planes, but no database data were found in order to compare the results.

4.6 Final remarks

The syntheses performed on W-based TMDs have been useful to assess the CVD functioning and to approach to this family of materials for the first time. From the positive results obtained, the study on the optimised synthesis parameters for the growth of ZrS_2, which were not yet known, started. Remarkably, the research effort has led to the successful synthesis of ZrS_2 thin films, on mm^2, both on gold and silicon wafers, through the CVD approach described in Chapter 4.4.1. Furthermore, the synthesis appears to be reproducible even at different growth times.

The investigation on the morphology of these films has led to the discover of vertically oriented flakes grown on a layer-by-layer structure of the same material, as proved by XRD measurements. The overall samples appear to have high crystalline purity with no obvious contamination by any other element, a part from Zr, S and O. Therefore, the present synthesis strategy can be employed to achieve high quality atomically thin ZrS_2 films, through a strict control of CVD parameters, which can be employed as a starting point for the promising application of their semiconducting and optical properties.

Conclusions and perspectives

The aim of this research project was the synthesis of ZrS_2 monolayer crystals of large areas. We have been able to demonstrate a novel CVD synthesis procedure to achieve high quality ZrS_2 thin films over cm^2 areas.

This work discloses new possibilities on the synthesis of ZrS_2 and reveals how the CVD parameters can be exploited to obtain high quality materials via a reproducible, cost effective and industrially scalable synthesis method.

Furthermore, to the best of our knowledge, this is the first time ZrS_2 has been reported to grow with vertically oriented flakes on a layer-by-layer substrate of the same material on both gold and silicon wafers. The flakes dimensions can be tuned according to the growth time following a low-vacuum synthesis using a simple laboratory equipment. The dimension of flakes has been studied by SEM and cross-sectional SEM leading to dimensions in the range of half to few micrometres. Other characteriations, such as TEM and SAED, proved the crystalline quality and the hexagonal lattice of the as-synthesised ZrS_2 films. Furthermore, the semiconducting nature of our material has been verified by the absorption spectroscopy while its optical qualities has been assessed with a PL peak at its optical band gap.

We also synthesised ZrS_xSe_{2-x} alloys by an annealing process of a pre-synthesised ZrS_2 substrate, confirming the deposition of selenium after the procedure. The properties are yet to be fully characterized but its synthesis has been proved.

This work gives the basis for future possibilities of improvement of the synthesis methodology, aiming to a further control on the thickness and on the deposition

over large areas for future applications. The large-scale growth of ZrS_2 directly onto insulating substrates (such as SiO_2/Si) and flexible platforms (such as Au) would also enable the batch fabrication of electronic and optoelectronic devices on flexible substrates on a technologically relevant scale without the need of film transfer.

The future research effort will be directed to the build-up of an MOCVD set up, which can furtherly add controllability on the precursors deposition quantity and thus, it can lead to better achievable results.

Since an atomic force microscope (AFM) measurements couldn't be conducted on a completely covered substrate because of the high degree of roughness, a cross-sectional SEM could be performed to quantify the vertical flakes height. Furthermore, a deeper access to the characterisation of the surface of the thin films would be possible by the use of a profilometer. The topography of the as-synthesised ZrS_2 thin films would be visible and accessible to measurements and we could assign a value of thickness to our thin films and correlate them with the number of layers present by dividing it by the *c* parameter of the unit cell.

The last missing step of the project is the fabrication of devices from the material in order to test its performances and compare it with the state-of-the-art.

Appendix

A.1. Pressure variation during deposition

During the study of the experimental parameters influencing the crystal growth of ZrS_2, I did not mentioned the pressure variation. Indeed, I tried to vary the pressure inside the chamber, mainly to diminish the mean free path of each atom and compound in the vapour phase in order to increase the residence time onto the substrate and favour the adhesion. But the problem was the manual control of the pumping system, which was very difficult to stabilize on a precise value during the deposition time. I once tried to increase the pressure to values double the ones of the regular depositions (3-4 mbar) but on the substrate were grown only crystallites and ribbons lately labelled as sulphur structures, as we can see in Figure A.1.

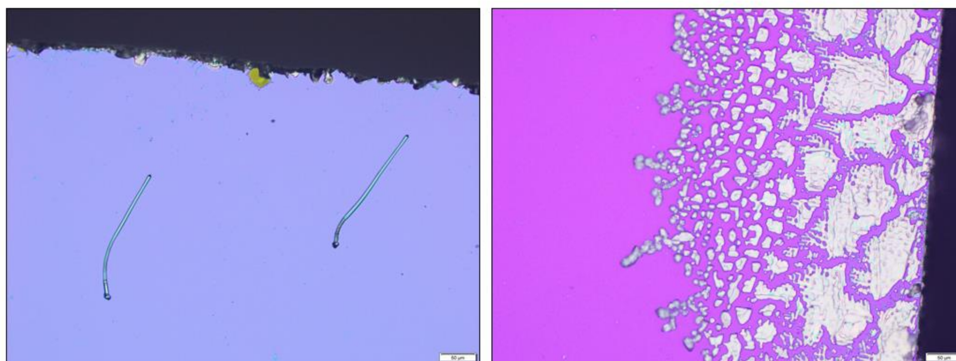

Figure A.1: Sulphur structures, crystallites and ribbons.

A.2. SAED of other ZrS_2 crystals

During the SAED measurements, also other diffraction patterns appeared from the analysis of other exfoliated flakes. An example is shown in Figure A.2, where we show the SAED measurement referred to the flake on the left. The diffraction pattern resulted to be hexagonal also in this case, but the diffraction spots appeared doubled. This result may be due to the fact that, in the selected area analysed, two single crystalline domains overlapped and they were rotated around their *c* axis with respect one another.

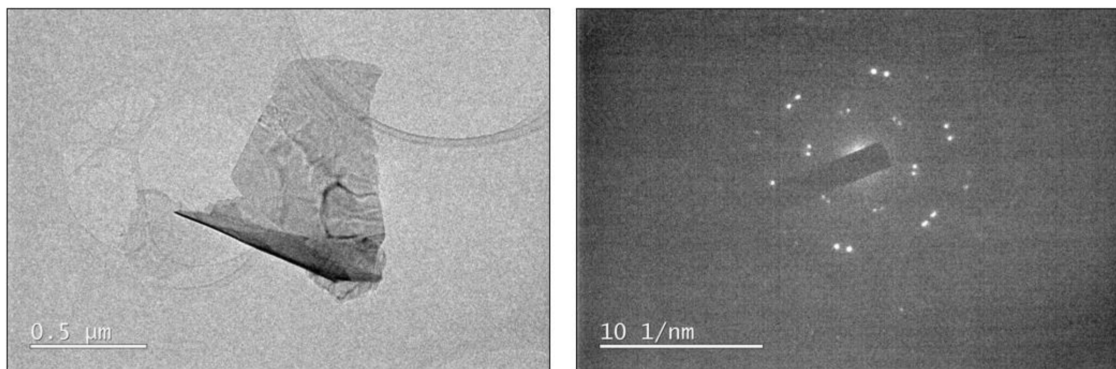

Figure A.2: Left: Exfoliated ZrS_2 flake on TEM grid. Right: Resultant SAED pattern.

References

[1] K. F. Mak, C. Lee, J. Hone, J. Shan, and T. F. Heinz, "Atomically Thin MoS 2 : A New Direct-Gap Semiconductor," *Phys. Rev. Lett.*, vol. 136805, no. September, pp. 2–5, 2010.

[2] M. Samadi, N. Sarikhani, M. Zirak, H. Zhang, H. L. Zhang, and A. Z. Moshfegh, "Group 6 transition metal dichalcogenide nanomaterials: Synthesis, applications and future perspectives," *Nanoscale Horizons*, vol. 3, no. 2, pp. 90–204, 2018.

[3] S. Manzeli, D. Ovchinnikov, D. Pasquier, O. V. Yazyev, and A. Kis, "2D transition metal dichalcogenides," *Nat. Rev. Mater.*, vol. 2, no. 8, p. 17033, Jun. 2017.

[4] C. Yan *et al.*, "2D Group IVB Transition Metal Dichalcogenides," *Adv. Funct. Mater.*, vol. 28, no. 39, pp. 1–18, 2018.

[5] Y. Li *et al.*, "Accurate identification of layer number for few-layer WS_2 and WSe_2 via spectroscopic study," *Nanotechnology*, vol. 29, no. 12, p. 124001, Mar. 2018.

[6] J. Shang, S. Zhang, X. Cheng, Z. Wei, and J. Li, "Electric field induced electronic properties modification of ZrS2/HfS2van der Waals heterostructure," *RSC Adv.*, vol. 7, no. 24, pp. 14625–14630, 2017.

[7] Q. Zhao, Y. Guo, K. Si, Z. Ren, J. Bai, and X. Xu, "Elastic, electronic, and dielectric properties of bulk and monolayer ZrS 2 , ZrSe 2 , HfS 2 , HfSe 2 from van der Waals density-functional theory."

[8] T. V. Vu *et al.*, “Electronic properties and optical behaviors of bulk and monolayer ZrS2: A theoretical investigation,” *Superlattices Microstruct.*, vol. 125, pp. 205–213, Jan. 2019.

[9] Y. Li, J. Kang, and J. Li, “Indirect-to-direct band gap transition of the ZrS2 monolayer by strain: first-principles calculations,” *RSC Adv.*, vol. 4, no. 15, p. 7396, Jan. 2014.

[10] Y. Si *et al.*, “Dramatically Enhanced Visible Light Response of Monolayer ZrS2 via Non-covalent Modification by Double-Ring Tubular B20 Cluster,” *Nanoscale Res. Lett.*, vol. 11, no. 1, p. 495, Dec. 2016.

[11] W. Zhang, Z. Huang, W. Zhang, and Y. Li, “Two-dimensional semiconductors with possible high room temperature mobility,” *Nano Res.*, vol. 7, no. 12, pp. 1731–1737, Dec. 2014.

[12] G. Ding, G. Y. Gao, Z. Huang, W. Zhang, and K. Yao, “Thermoelectric properties of monolayer *M* Se $_2$ (M = Zr, Hf): low lattice thermal conductivity and a promising figure of merit,” *Nanotechnology*, vol. 27, no. 37, p. 375703, Sep. 2016.

[13] F. Khan *et al.*, “Theoretical investigation of electronic structure and thermoelectric properties of MX2 (M=Zr, Hf; X=S, Se) van der Waals heterostructures,” *J. Phys. Chem. Solids*, 2019.

[14] F. Reale *et al.*, “High-Mobility and High-Optical Quality Atomically Thin WS2,” *Sci. Rep.*, vol. 7, no. 1, pp. 1–10, 2017.

[15] S. Li *et al.*, “Halide-assisted atmospheric pressure growth of large WSe2 and WS2 monolayer crystals,” *Appl. Mater. Today*, vol. 1, no. 1, pp. 60–66, Nov. 2015.

[16] Y.-C. Lin *et al.*, “Realizing Large-Scale, Electronic-Grade Two-Dimensional Semiconductors,” *ACS Nano*, vol. 12, no. 2, pp. 965–975, Feb. 2018.

[17] Y. Gao *et al.*, “Large-area synthesis of high-quality and uniform monolayer

WS2 on reusable Au foils," *Nat. Commun.*, vol. 6, no. 1, p. 8569, Dec. 2015.

[18] C. Cong *et al.*, "Synthesis and Optical Properties of Large-Area Single-Crystalline 2D Semiconductor WS $_2$ Monolayer from Chemical Vapor Deposition," *Adv. Opt. Mater.*, vol. 2, no. 2, pp. 131–136, Feb. 2014.

[19] Y. Zhang *et al.*, "Controlled growth of high-quality monolayer WS2 layers on sapphire and imaging its grain boundary," *ACS Nano*, vol. 7, no. 10, pp. 8963–8971, 2013.

[20] Y. Gao *et al.*, "Ultrafast Growth of High-Quality Monolayer WSe $_2$ on Au," *Adv. Mater.*, vol. 29, no. 29, p. 1700990, Aug. 2017.

[21] K. Kang *et al.*, "High-mobility three-atom-thick semiconducting films with wafer-scale homogeneity," *Nature*, vol. 520, no. 7549, pp. 656–660, Apr. 2015.

[22] J. K. Huang *et al.*, "Large-area synthesis of highly crystalline WSe2 monolayers and device applications," *ACS Nano*, vol. 8, no. 1, pp. 923–930, 2014.

[23] G. Clark *et al.*, "Vapor-transport growth of high optical quality WSe $_2$ monolayers," *APL Mater.*, vol. 2, no. 10, p. 101101, Oct. 2014.

[24] X. Wang, L. Huang, X.-W. Jiang, Y. Li, Z. Wei, and J. Li, "Large scale ZrS $_2$ atomically thin layers," *J. Mater. Chem. C*, vol. 4, no. 15, pp. 3143–3148, Apr. 2016.

[25] M. Zhang *et al.*, "Controlled Synthesis of ZrS $_2$ Monolayer and Few Layers on Hexagonal Boron Nitride," *J. Am. Chem. Soc.*, vol. 137, no. 22, pp. 7051–7054, Jun. 2015.

[26] R. Thiyagarajan, M. Mahaboob Beevi, and M. Anusuya, "Nano structural characteristics of Zirconium Sulphide thin films," *Journal of American Science*, 2009.

[27] C. Yan *et al.*, "Space-Confined Chemical Vapor Deposition Synthesis of

Ultrathin HfS_2 Flakes for Optoelectronic Application," *Adv. Funct. Mater.*, vol. 27, no. 39, p. 1702918, Oct. 2017.

[28] L. Fu *et al.*, "Van der Waals Epitaxial Growth of Atomic Layered HfS_2 Crystals for Ultrasensitive Near-Infrared Phototransistors," *Adv. Mater.*, vol. 29, no. 32, p. 1700439, Aug. 2017.

[29] M. J. Mleczko *et al.*, "$HfSe_2$ and $ZrSe_2$: Two-dimensional semiconductors with native high-κ oxides," *Sci. Adv.*, vol. 3, no. 8, p. e1700481, Aug. 2017.

[30] B. Zheng *et al.*, "CVD growth of large-area and high-quality HfS2 nanoforest on diverse substrates," *Appl. Surf. Sci.*, vol. 435, pp. 563–567, Mar. 2018.

[31] B. Zheng *et al.*, "Vertically oriented few-layered HfS_2 nanosheets: growth mechanism and optical properties," *2D Mater.*, vol. 3, no. 3, p. 035024, Sep. 2016.

[32] S. M. Eichfeld *et al.*, "Highly Scalable, Atomically Thin WSe_2 Grown *via* Metal–Organic Chemical Vapor Deposition," *ACS Nano*, vol. 9, no. 2, pp. 2080–2087, Feb. 2015.

[33] W. Choi, N. Choudhary, G. H. Han, J. Park, D. Akinwande, and Y. H. Lee, "Recent development of two-dimensional transition metal dichalcogenides and their applications," *Mater. Today*, vol. 20, no. 3, pp. 116–130, Apr. 2017.

[34] G. Lucovsky, R. M. White, J. A. Benda, and J. F. Revelli, "Infrared-reflectance spectra of layered group-IV and group-VI transition-metal dichalcogenides," *Phys. Rev. B*, vol. 7, no. 8, pp. 3859–3870, 1973.

[35] W. Zhao *et al.*, "Lattice dynamics in mono- and few-layer sheets of WS2 and WSe2," *Nanoscale*, vol. 5, no. 20, p. 9677, Sep. 2013.

[36] S. Mañas-Valero *et al.*, "Raman Spectra of ZrS2 and ZrSe2 from Bulk to Atomically Thin Layers," *Appl. Sci.*, vol. 6, no. 9, p. 264, Sep. 2016.

[37] L. Roubi and C. Carlone, "Resonance Raman spectrum of HfS2 and ZrS2,"

Phys. Rev. B, vol. 37, no. 12, pp. 6808–6812, 1988.

[38] P. C. Klipstein, C. M. Pereira, and R. H. Friend, "Transport and Raman studies of the group IV layered compounds and their lithium intercalates: LixTiS2, LixTiSe2, LixZrS2, LixZrSe2, LixHfS2and LixHfSe2," *Philos. Mag. B Phys. Condens. Matter; Stat. Mech. Electron. Opt. Magn. Prop.*, vol. 56, no. 5, pp. 531–559, 1987.

[39] N. Briggs *et al.*, "A roadmap for electronic grade 2D materials," *2D Mater.*, vol. 6, no. 2, p. 022001, 2019.

[40] Z. Cai, B. Liu, X. Zou, and H. M. Cheng, "Chemical Vapor Deposition Growth and Applications of Two-Dimensional Materials and Their Heterostructures," *Chem. Rev.*, vol. 118, no. 13, pp. 6091–6133, 2018.

[41] L. M. Xie, "Two-dimensional transition metal dichalcogenide alloys: preparation, characterization and applications," *Nanoscale*, vol. 7, no. 44, pp. 18392–18401, Nov. 2015.

[42] Y. Zhu, X. Wang, M. Zhang, C. Cai, and L. Xie, "Thickness and temperature dependent electrical properties of ZrS2 thin films directly grown on hexagonal boron nitride," *Nano Res.*, vol. 9, no. 10, pp. 2931–2937, Oct. 2016.

[43] T. Kanazawa *et al.*, "Few-layer HfS2 transistors," *Sci. Rep.*, vol. 6, no. 1, p. 22277, Apr. 2016.

[44] M. Kang *et al.*, "Electrical characterization of multilayer $HfSe_2$ field-effect transistors on SiO_2 substrate," *Appl. Phys. Lett.*, vol. 106, no. 14, p. 143108, Apr. 2015.

[45] L. Yin *et al.*, "Ultrafast and ultrasensitive phototransistors based on few-layered $HfSe_2$," *Appl. Phys. Lett.*, vol. 109, no. 21, p. 213105, Nov. 2016.

[46] B. Liu, M. Fathi, L. Chen, A. Abbas, Y. Ma, and C. Zhou, "Chemical Vapor Deposition Growth of Monolayer WSe_2 with Tunable Device Characteristics and Growth Mechanism Study," *ACS Nano*, vol. 9, no. 6, pp.

6119–6127, Jun. 2015.

[47] J. E. Greene, "Thin Film Nucleation, Growth, and Microstructural Evolution: An Atomic Scale View,", *William Andrew Applied Science Publishers*, *Handb. Depos. Technol. Film. Coatings*, pp. 554–620, Jan. 2010.

[48] A. C. Jones and M. L. Hitchman, *Chemical Vapour Deposition: Precursors, Processes and Applications*. *RSC Publishing*, 2009.

[49] A. Govind Rajan, J. H. Warner, D. Blankschtein, and M. S. Strano, "Generalized Mechanistic Model for the Chemical Vapor Deposition of 2D Transition Metal Dichalcogenide Monolayers," *ACS Nano*, vol. 10, no. 4, pp. 4330–4344, 2016.

[50] R. Yue *et al.*, "Nucleation and growth of WSe_2: enabling large grain transition metal dichalcogenides," *2D Mater.*, vol. 4, no. 4, p. 045019, Sep. 2017.

[51] S. Wang *et al.*, "Shape Evolution of Monolayer MoS_2 Crystals Grown by Chemical Vapor Deposition," *Chem. Mater.*, vol. 26, no. 22, pp. 6371–6379, Nov. 2014.

[52] J. Dong, L. Zhang, and F. Ding, "Kinetics of Graphene and 2D Materials Growth," *2D Materials*, vol. 1801583, pp. 1–29, 2019.

[53] D. Dumcenco *et al.*, "Large-Area Epitaxial Monolayer MoS_2," *ACS Nano*, vol. 9, no. 4, pp. 4611–4620, Apr. 2015.

[54] A. M. van der Zande *et al.*, "Grains and grain boundaries in highly crystalline monolayer molybdenum disulphide," *Nat. Mater.*, vol. 12, no. 6, pp. 554–561, Jun. 2013.

[55] W. Guo *et al.*, "Governing Rule for Dynamic Formation of Grain Boundaries in Grown Graphene," *ACS Nano*, vol. 9, no. 6, pp. 5792–5798, Jun. 2015.

[56] J. Cheng *et al.*, "Kinetic Nature of Grain Boundary Formation in As-Grown

MoS $_2$ Monolayers," *Adv. Mater.*, vol. 27, no. 27, pp. 4069–4074, Jul. 2015.

[57] C.R. Brundle, C. A. Evans Jr., W. Shaun, "Enciclopedia of Materials characterization," *Manning Publications Co.*, pp. 282–299, 1992.

[58] H. Kim, D. Ovchinnikov, D. Deiana, D. Unuchek, and A. Kis, "Suppressing nucleation in metal-organic chemical vapor deposition of MoS2 monolayers by alkali metal halides," *Nano Lett.*, vol. 17, no. 8, pp. 5056–5063, 2017.

[59] H. Kim *et al.*, "Role of alkali metal promoter in enhancing lateral growth of monolayer transition metal dichalcogenides," *Nanotechnology*, vol. 28, no. 36, p. 36LT01, Sep. 2017.

[60] J. Zhou *et al.*, "A library of atomically thin metal chalcogenides," *Nature*, vol. 556, no. 7701, pp. 355–359, Apr. 2018.

[61] M. Lenz and R. Gruehn, "Developments in measuring and calculating chemical vapor transport phenomena demonstrated on Cr, Mo, W, and their compounds," *Chem. Rev.*, vol. 97, no. 8, pp. 2967–2994, 1997.

[62] A. Berkdemir *et al.*, "Identification of individual and few layers of WS2 using Raman Spectroscopy," *Sci. Rep.*, vol. 3, no. 1, p. 1755, Dec. 2013.

[63] F. Reale, K. Sharda, and C. Mattevi, "From bulk crystals to atomically thin layers of group VI-transition metal dichalcogenides vapour phase synthesis," *Appl. Mater. Today*, vol. 3, pp. 11–22, Jun. 2016.

[64] S. Najmaei *et al.*, "Vapour phase growth and grain boundary structure of molybdenum disulphide atomic layers," *Nat. Mater.*, vol. 12, no. 8, pp. 754–759, Aug. 2013.

[65] X. Zhang *et al.*, "Diffusion-Controlled Epitaxy of Large Area Coalesced WSe2Monolayers on Sapphire," *Nano Lett.*, vol. 18, no. 2, pp. 1049–1056, 2018.

[66] S. Lippert *et al.*, "Influence of the Substrate Material on the Optical

Properties of Tungsten Diselenide Monolayers," *2D Materials*, Sep. 2016.

[67] A. A. Palko, A. D. Ryon, and D. W. Kuhn, "The vapor pressures of zirconium tetrachloride and hafnium tetrachloride," *J. Phys. Chem.*, vol. 62, no. 3, pp. 319–322, 1958.

[68] Q. Zhang *et al.*, "Reliable Synthesis of Large-Area Monolayer WS_2 Single Crystals, Films, and Heterostructures with Extraordinary Photoluminescence Induced by Water Intercalation," *Adv. Opt. Mater.*, vol. 6, no. 12, p. 1701347, Jun. 2018.

[69] Q. Ji, Y. Zhang, Y. Zhang, and Z. Liu, "Chemical vapour deposition of group-VIB metal dichalcogenide monolayers: engineered substrates from amorphous to single crystalline," *Chem. Soc. Rev.*, vol. 44, no. 9, pp. 2587–2602, Apr. 2015.

[70] S. Li, C. Wang, and H. Qiu, "Single- and few-layer ZrS2 as efficient photocatalysts for hydrogen production under visible light," *Int. J. Hydrogen Energy*, vol. 40, no. 45, pp. 15503–15509, Dec. 2015.

[71] H. Isomäki and J. von Boehm, "Bonding and Band Structure of ZrS_2 and $ZrSe_2$," *Phys. Scr.*, vol. 24, no. 2, pp. 465–467, Aug. 1981.

[72] L. Li *et al.*, "Electrical Transport and High-Performance Photoconductivity in Individual ZrS2 Nanobelts," *Adv. Mater.*, vol. 22, no. 37, pp. 4151–4156, Aug. 2010.